university of groningen

FORMING WORLDS

Modelling the Interior Structure of Rocky Exoplanets with Zalmoxis*

Bachelor's Project Thesis

Flavia Cristiana Pascal, s5351685, f.pascal@student.rug.nl
Supervisors: Dr. Tim Lichtenberg
Second examiner: Dr. Quentin Changeat

July 12, 2025

ABSTRACT

Context. Understanding exoplanet interiors is crucial for constraining their composition, thermal evolution, and habitability. Realistic simulations require self-consistent modeling of interior and atmosphere across diverse masses and compositions.
Aims. This thesis focuses on three main goals: (1) to develop and extend Zalmoxis, an open-source, pip-installable Python package for modeling the interiors of terrestrial-like exoplanets such as super-Earths and sub-Neptunes; (2) to integrate the extended Zalmoxis into the coupled atmosphere-interior framework PROTEUS, enabling self-consistent simulations of rocky planet evolution; and (3) to couple Zalmoxis with the mantle evolution module Aragog within PROTEUS to simulate the thermochemical evolution of fully molten rocky exoplanets.
Methods. Zalmoxis solves a system of coupled ordinary differential equations governing hydrostatic equilibrium, mass conservation, and gravity to compute the radial profiles of mass, density, pressure, and gravity from the core to the surface, for input masses up to 50 $M_\oplus$ and specified core mass fraction(s). It incorporates numerical equations of state from Seager et al. [2007] to model two differentiated planet types: (1) super-Earths with an Fe core and $MgSiO_3$ mantle, and (2) water-rich planets with an additional water ice layer. Zalmoxis is validated using `pytest` against mass-radius relations from Zeng et al. [2019] and internal structure profiles from Seager et al. [2007]. It achieves full model convergence in ∼5 seconds for a 1 $M_\oplus$ planet, enabling quick parameter space exploration.
Results. Following integration with PROTEUS, the Zalmoxis-Aragog pipeline is used to simulate the evolution of fully molten rocky exoplanets across the 1 to 7 $M_\oplus$ range. The results reveal a preliminary mass dependence in crystallization timescales. As planetary mass increases, volatile outgassing efficiency decreases, leading to lower surface pressures and reduced H_2O release. H_2O becomes the dominant volatile for 1 and 2 $M_\oplus$ planets upon their complete solidification. However, the current version of Aragog fails to robustly capture the expected bottom-up crystallization behavior in planets more massive than 2 $M_\oplus$, likely due to limitations in the extrapolation of high-pressure melting curves.
Conclusions. This work extends interior-atmosphere coupling modeling in rocky exoplanets by integrating Zalmoxis into PROTEUS. The pipeline now enables physically consistent thermochemical and volatile evolution simulations over a broader mass range. Preliminary findings show that increasing mass influences mantle crystallization and volatile outgassing, affecting surface pressure and atmospheric composition. Further improvements in Aragog's melting curves coverage and energy transport modeling are needed to better capture solidification at higher masses.

1 INTRODUCTION

1.1 The Diversity of Exoplanets

The discovery of thousands of exoplanets over the past few decades has revealed a striking diversity in planetary properties, far beyond what is represented within our own Solar System. Figure 1.1 illustrates this variety: exoplanets span a wide range of sizes and masses, clustering into distinct groups based on their likely compositions. This diversity raises one of the fundamental questions in planetary science: what are the internal compositions of these worlds? Alongside its illustrative value, the mass-radius diagram highlights a key challenge: inferring planetary composition from limited observables. Ongoing research effort is

Named after the deity of the Getae and Dacians, ancient peoples from the lower Danube region (present-day Romania and Bulgaria). Derived from the Thracian word "zamol", meaning "earth".

focusing on developing more refined mass-radius relationships to better distinguish between rocky, icy, and gaseous planets, and to keep up with the rapid expansion of the exoplanet catalog. While only three idealized composition curves (for H_2O, $MgSiO_3$, and Fe) are shown in Figure 1.1 for illustrative purposes, they exemplify the broader effort to characterize internal structures based on indirect observations.

1.2 Inferring interiors from limited observables

A planet's bulk composition refers to the overall elemental and mineral makeup of the entire planet, averaged over all internal layers. It includes the relative abundances of major rock-forming elements (e.g., Fe, Mg, Si, O) and volatiles (e.g., H, He, H_2O), which are shaped by formation environment and accretion history. In exoplanet modeling, bulk composition is a key input or inference from observables such as mass and radius, since it governs the density structure and influences whether a planet is rocky, icy, or gas-rich (Lichtenberg and Miguel [2025]).

Among all known planets, Earth remains unique as one of the few worlds whose internal structures have been directly measured through seismic and geophysical observations, alongside Mars, recently probed by the InSight mission (Le Maistre et al. [2023]). However, beyond the Solar System, such direct measurements are impossible with the current technology. Instead, understanding exoplanet interiors relies primarily on indirect observations (Dressing et al. [2015], Dorn et al. [2015], Dorn et al. [2018], Madhusudhan et al. [2020], Bloot et al. [2023]) and theoretical models grounded in Earth and Solar System analogs (Valencia et al. [2006, 2007], Fortney et al. [2007], Seager et al. [2007], Léger et al. [2004], Sotin et al. [2007], Grasset et al. [2009], Rogers and Seager [2010], Wagner et al. [2012], Swift et al. [2011], Gong and Zhou [2012], Madhusudhan et al. [2012], Tackley et al. [2013], Zeng et al. [2016], Boujibar et al. [2020], Noack and Lasbleis [2020], Unterborn and Panero [2019], Lin et al. [2024], Sahu et al. [2025]). The standard modeling approach assumes that exoplanets are spherically symmetric and in hydrostatic equilibrium, allowing the interior structure to be determined by solving coupled differential equations describing how mass, pressure, and density vary with radius, typically the equations of hydrostatic equilibrium, mass conservation, and an appropriate equation of state (EOS) (Duffy et al. [2015]).

Direct observational constraints on exoplanet interiors are virtually absent, with existing knowledge largely based on indirect inferences from bulk properties such as mass and radius. As the number of discovered exoplanets continues to grow, presenting a wide diversity in masses, radii, and compositions, these indirect methods and models represent essential tools to interpret and understand the rich variety of planetary interiors beyond the Solar System. In this context, the term planetary interior broadly refers to all layers of a planet that are not predominantly gaseous. This includes rocky mantles and metallic cores typical of terrestrial planets, as well as volatile-rich interiors of planets that may contain exotic phases such as high-pressure ices (Lichtenberg and Miguel [2025]).

1.3 Diversity of rocky exoplanets

Exoplanets are commonly classified based on their position in the mass-radius-density parameter space. Planets with radii up to roughly 2 $R_\oplus$ and masses up to about 10 $M_\oplus$ are often categorized as either super-Earths or sub-Neptunes. Sub-Neptunes tend to exhibit lower densities, consistent with substantial gaseous envelopes and Neptune-like compositions, whereas super-Earths display higher densities indicative of predominantly rocky interiors (Lichtenberg and Miguel [2025]).

However, as Duffy et al. [2015] emphasize, there are no direct analogs to super-Earths in the Solar System. The limited observational data suggest that super-Earths span a broad spectrum of internal structures and surface conditions, ranging from iron-rich super-Mercuries and molten lava planets to water planets enveloped by thick, steamy atmospheres, and even carbon-dominated planets. It remains an open question what fraction of these planets are scaled-up versions of terrestrial planets, scaled-down ice giants such as Neptune, or intermediate cases blending features of both classes (Duffy et al. [2015]).

1.4 Core-mantle differentiation and core mass fractions

Within the Solar System, planets exhibit a common internal stratification due to chemical differentiation during and after planetary accretion, where denser materials such as iron segregate to form cores, overlain by silicate mantles and crusts composed of progressively less dense materials (Seager et al. [2007], Lichtenberg and Miguel [2025]). This general principle is extended to exoplanet modeling, which typically assumes similar differentiation for rocky worlds. In such models, the iron alloy in the core is generally assumed to be liquid, akin to Earth's outer core, which dominates over the smaller solid inner core. The inner core likely forms through gradual solidification of the liquid outer core, and in more massive planets, the greater internal heat content makes a fully or predominantly liquid core even more probable (Zeng et al. [2016]).

Core mass fraction (CMF), the proportion of a planet's mass residing in the core, is a key pa-

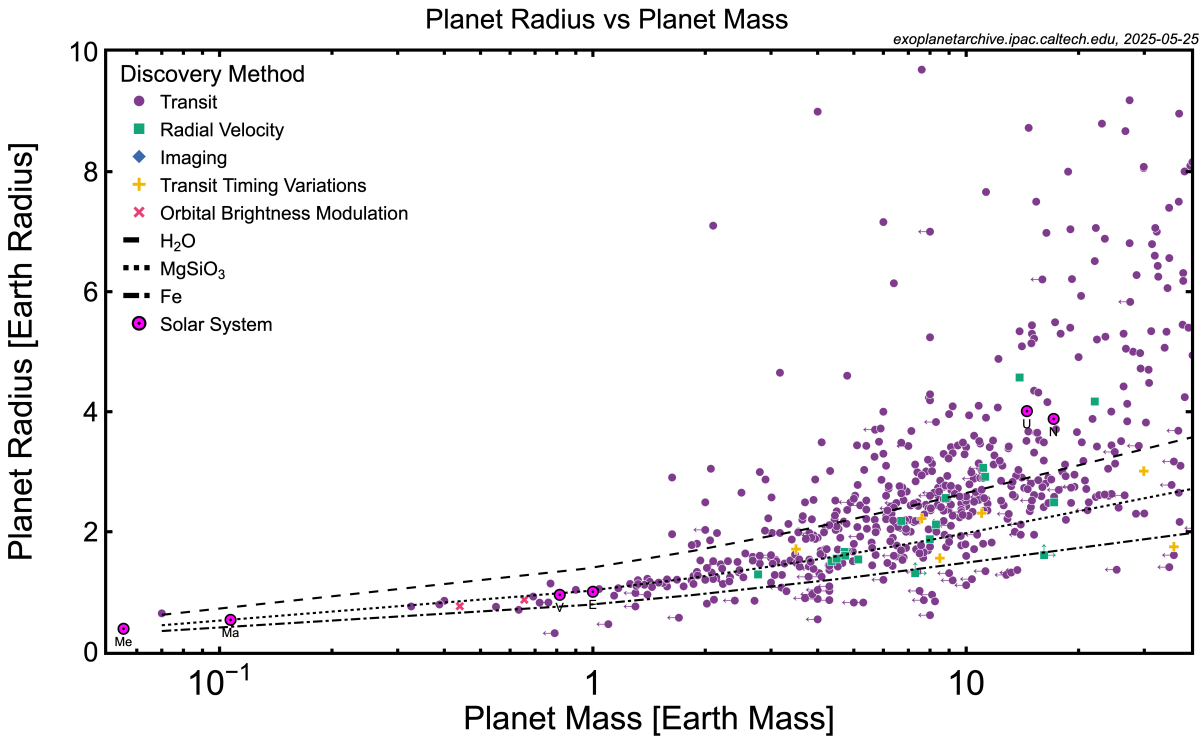

Figure 1.1: Radius vs. mass plot for confirmed exoplanets, using default parameter values from the Planetary Systems interactive table of the NASA Exoplanet Archive [2025]. Planets are grouped by discovery method. The plot is zoomed in to show planet masses between 0.05 and 40 $M_\oplus$ (logarithmic scale) and radii between 0 and 10 $R_\oplus$. For context, density curves corresponding to pure H_2O, $MgSiO_3$, and Fe compositions are overlaid. Solar System planets are included for comparison.

rameter in interior modeling. Typical core mass fractions in rocky planets provide a key constraint on internal structure models. For Earth, the core constitutes roughly $32 - 33\%$ of the planet's total mass (McDonough [2003]), with similar values estimated for Venus and Mars (Mocquet et al. [2011], Aitta [2012]), although with some variation reflecting planetary formation conditions and composition (Boujibar et al. [2020]). Mercury's unusually high CMF ($\sim 68\%$) indicates significant mantle stripping or differentiation processes (Helffrich et al. [2019]). Super-Earth exoplanets may exhibit a range of CMFs, from Earth-like values to significantly higher or lower fractions, depending on their formation history, bulk composition, and subsequent evolutionary processes (Unterborn and Panero [2019]). The core mass fraction in rocky planets is influenced not only by the total iron content but also by the processes that determine how iron is distributed between the core and mantle during differentiation. However, interior mass-radius relationships are relatively insensitive to variations in iron partitioning between core and mantle (Elkins-Tanton and Seager [2008], Fortney et al. [2009], Duffy et al. [2015]).

1.5 Extreme conditions in super-Earth interiors

For planets in the super-Earth and Earth-sized range, internal pressures and temperatures can reach extremes far beyond terrestrial conditions, with pressures reaching several TPa and temperatures potentially exceeding 10000 K (Wagner et al. [2012], Boujibar et al. [2020]). Such conditions give rise to mineral phases and physical properties not found naturally on Earth, though they can be investigated using synthetic materials in high-pressure laboratory experiments (Lichtenberg and Miguel [2025]). In particular, $MgSiO_3$ (abundant in Earth's mantle) occurs in both perovskite and postperovskite forms, with the postperovskite phase likely determining the geophysical behavior of rocky super-Earth interiors (Wagner et al. [2012], Tackley et al. [2013], Boujibar et al. [2020], Lichtenberg and Miguel [2025]). To illustrate the diversity of mineralogical phases that arise under super-Earth interior conditions, Figure 1.2 presents a schematic summary of experimentally predicted geochemical compositions across a range of elementally distinct exoplanet interiors.

1.6 Water-rich exoplanets

Beyond purely rocky planets, a significant subset of exoplanets, often referred to as "water worlds"

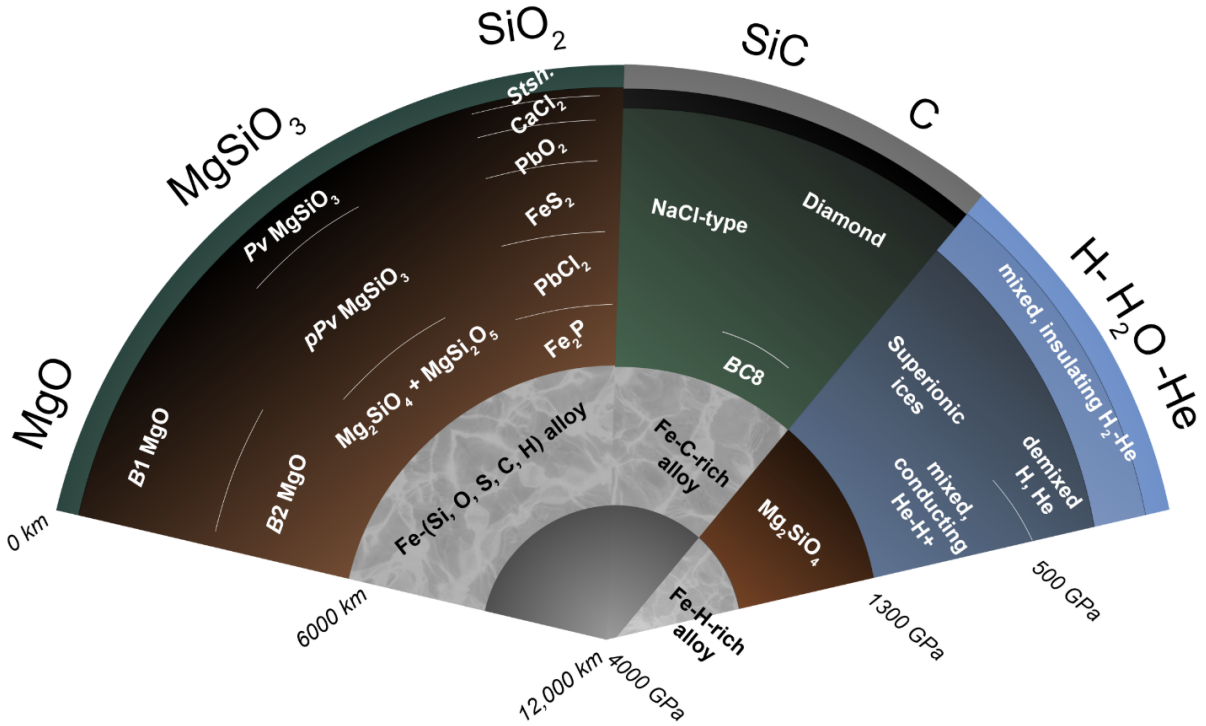

Figure 1.2: Geochemical predictions for temperate super-Earth exoplanets informed by laboratory experiments under different compositional regimes. Adapted from Lichtenberg and Miguel [2025], extending prior work by Duffy et al. [2015], with a schematic by Claire Zurkowski.

or "ocean planets", may contain layers of water or water ice atop their rocky interiors, potentially extending thousands of kilometers in depth (Léger et al. [2004], Sotin et al. [2007], Noack et al. [2016]). These planets are generally smaller and cooler than the Solar System's ice giants, with outer layers that may allow for the stable presence of water ice. In contrast, Uranus and Neptune, while also volatile-rich, have internal pressures and temperatures far too high for water ice to be stable. Their interiors likely consist of exotic high-pressure phases or supercritical water, with water ice making up more than 70% of their mass under the assumption of a differentiated layered structure. Even in smaller water worlds, interior conditions can be extreme, with pressures exceeding 500 GPa on their Earth-sized iron-silicate cores and central states reaching up to 2400 GPa and 6500 K in 10 $M_\oplus$ planets (Duffy et al. [2015], Lin et al. [2024]).

1.7 Equations of state in planetary interior models

A planet's internal structure depends on how its materials respond to extreme pressures and temperatures as governed by an equation of state (EOS). Defined as a thermodynamic relation that connects pressure, density, and temperature of a given material, the EOS thus represents a crucial component for accurately modeling planetary interiors in relation to observable parameters such as mass and radius. However, no single EOS formulation can capture the full range of physical conditions encountered across all planetary types and layers. Instead, different EOSs are required depending on the dominant materials (e.g., iron, silicates, water in various phases, hydrogen-helium) and pressure-temperature regimes, ranging from solid rocky mantles to volatile-rich envelopes and degenerate cores. The choice of EOS must therefore be tailored to the specific context and composition of the planet under study (Duffy et al. [2015]).

1.7.1 Theoretical and practical EOS formulations

To derive EOS data for planetary materials, both experimental and theoretical approaches are employed to investigate material behavior under extreme pressures and temperatures. Among the theoretical methods, quantum mechanical simulations such as density functional theory (DFT) are often used to derive thermodynamic properties by modeling fundamental electron-nucleus interactions. The calculations are typically simplified using approximations like the Local Density Approximation (LDA), which assumes the exchange-correlation energy depends only on local electron density, or the Generalized Gradient Approximation (GGA), which improves upon LDA by including the spatial variation of the electron density, not just the local value. These methods are experimentally validated primarily under low-pressure conditions

(Duffy et al. [2015]).

Interior models in the literature vary in how they incorporate the EOS. Some adopt detailed thermal profiles and self-consistent, temperature-dependent EOS formulations, while others assume isothermal or adiabatic interiors, thereby simplifying thermal effects. To implement EOSs in practical modeling, isothermal formulations such as the Birch-Murnaghan and Vinet equations are used. These semi-empirical models are calibrated against high-pressure experimental data, such as that from diamond anvil cells or shock compression experiments. The Birch-Murnaghan EOS is based on a finite strain expansion and is common in geophysics, though its accuracy can be limited by the order of expansion and choice of strain variable. On the other hand, the Vinet EOS, derived from interatomic potential theory, usually matches experimental results at very high pressures better than the Birch-Murnaghan EOS. As a result, the Vinet EOS is favored in studies involving a broad range of materials (Cohen et al. [2000]). Both Birch-Murnaghan and Vinet formulations can be extended to include thermal effects using models such as the Mie-Grüneisen-Debye formulation, which adds a temperature-dependent pressure correction linked to lattice vibrations (Duffy et al. [2015]).

While isothermal or adiabatic simplifications can reduce computational complexity or help isolate specific structural variables, they risk overlooking important variations introduced by thermal expansion, electronic effects, and phase transitions at high pressures. For example, as highlighted by Duffy et al. [2015], mineralogical phase transitions such as the transformation from perovskite to post-perovskite or the breakdown of silicates into oxides can subtly alter a planet's internal density structure. However, their impact on the global mass-radius relationship is often negligible, particularly when averaged over broad compositional regimes (Swift et al. [2011]). Furthermore, for high-density materials, temperature typically has a modest influence on the EOS and the resulting mass-radius relationships (Seager et al. [2007]), favoring the use of simplified thermal assumptions in certain regimes without significantly compromising accuracy. It is important to note that, while temperature has a relatively minor effect on the mass-radius relationship under super-Earth conditions, thermal properties remain essential for modeling internal energy transport and melting behavior, particularly in convecting regions where the Grüneisen parameter influences both the temperature gradient and melting temperatures of planetary materials (Duffy et al. [2015]).

At sufficiently extreme pressures, such as those deep within the interiors of large super-Earths or icy giants, all materials are expected to approach the Thomas-Fermi-Dirac (TFD) limit, in which the material behaves like a degenerate electron gas surrounding atomic nuclei. In this regime, pressure is primarily determined by electron degeneracy and the TFD approximation offers an adequate EOS description (Grasset et al. [2009], Seager et al. [2007]). However, most planetary interiors fall within an intermediate pressure regime ($\sim 200 - 10000$ GPa) that lies beyond the reach of most experimental techniques and below the applicability domain of the TFD model. Studies like Fortney et al. [2007], Wagner et al. [2012] suggest that, in this regime, EOS uncertainty results in radius variation of about $2 - 3\%$ for a given mass planet (Duffy et al. [2015]). Thus, the choice of EOS formulation often reflects a balance between physical fidelity and computational tractability, tailored to the specific planetary context.

1.8 Implications of internal structure for planetary evolution

A planet's internal structure and composition define how it stores and recycles heat and volatiles, shaping its surface and atmospheric environment over geological timescales. In this context, interior models are key to understanding a planet's long-term geological and atmospheric evolution and, ultimately, its potential habitability (Noack and Lasbleis [2020]), because they can constrain structural parameters such as core size, interior composition, and volatile inventory. These parameters not only influence a planet's thermal evolution but also determine how volatiles like H_2O and CO_2 are stored and exchanged between the interior and the atmosphere. For instance, Seager et al. [2007] highlight that detailed interior models, coupled with atmospheric modeling, are essential for inferring features like deep liquid water oceans. Such features cannot be identified from mass-radius relationships alone but may instead be revealed through observations of a saturated water vapor atmosphere. Similarly, Noack et al. [2014] emphasize that a planet's internal structure controls how efficiently it can retain atmospheric CO_2, which in turn affects surface conditions and the possibility of stable liquid water.

Understanding the coupling between a planet's internal structure and its atmospheric composition is especially critical when considering the early evolutionary stages of rocky planets. Many of them, especially those forming close to their stars or undergoing frequent collisions during accretion, are expected to begin in a fully or partially molten state, forming so-called global magma oceans (Lichtenberg and Miguel [2025]). More specifically, a magma ocean refers to a deep, planet-wide layer of molten silicate rock that forms when internal temperatures exceed the solidus of man-

tle material. Such magma oceans play a central role in partitioning volatiles between the planetary interior and the atmosphere. In the early stages, volatiles such as H_2O can dissolve efficiently in the molten mantle. However, as the mantle cools and begins to crystallize, these volatiles are increasingly outgassed into the atmosphere, shaping both its initial composition and thermal structure (Lebrun et al. [2013], Salvador et al. [2017], Lichtenberg and Miguel [2025]). As a result, the atmospheric mole fraction of H_2O can, for example, serve as a tracer of recent mantle solidification, providing insights into the ongoing volatile exchange between the interior and atmosphere during the late stages of magma ocean evolution (Nicholls et al. [2024]).

In this context, magma ocean modeling becomes particularly important for bridging a planet's bulk interior properties with its initial atmospheric composition and volatile budget. It offers a window into the coupled evolution of a planet's surface and atmosphere during its formative stages, and forms a critical component of interior-atmosphere coupling in habitability assessments. A key factor in this evolution is the rheological transition, which represents the critical melt fraction (typically around $40 - 60\%$) at which the mantle shifts from behaving like a solid to behaving like a liquid. This transition governs the mantle's viscosity and therefore fundamentally alters the planet's internal dynamics, including how efficiently it can transport heat, redistribute chemical elements, and outgas volatiles to the atmosphere. Because it marks the boundary between solid-like and fluid-like behavior, the rheological transition plays a decisive role in determining the longevity and efficiency of magma ocean-driven processes and in shaping the planet's long-term thermal and atmospheric evolution (Lichtenberg and Miguel [2025] and references therein).

The internal evolution of rocky planets can diverge significantly depending on their magma ocean crystallization dynamics, with two main scenarios particularly worth highlighting. In the classical bottom-up scenario, the mantle cools adiabatically and begins to crystallize from the core-mantle boundary upward (Elkins-Tanton and Seager [2008], Solomatov [2007]). This leads to efficient internal mixing, rapid progression toward the rheological transition (within 10^3–10^4 years), substantial volatile uptake, and eventual outgassing. In contrast, in more inhomogeneous scenarios, crystallization may initiate at intermediate depths or near the surface. This behavior arises from differences in mantle melting curves under pressure, as demonstrated by Bower et al. [2018], who compare the melting behavior reported by Stixrude et al. [2009] and Andrault et al. [2011]. These divergent pathways can result in order-of-magnitude differences in magma ocean cooling timescales and drive the emergence of atmospheres with distinct volatile compositions (Lichtenberg and Miguel [2025]).

1.9 Objective of this thesis

This thesis makes use of PROTEUS, a modular Python framework designed to simulate the coupled evolution of planetary interiors and atmospheres over geological timescales (Lichtenberg et al. [2021], Johnstone et al. [2021], Graham et al. [2021], Nicholls et al. [2024, 2025]). The framework enables time-dependent simulations by integrating physical modules for mantle convection, volatile cycling, atmospheric loss, and stellar forcing (Nicholls et al. [2024]). Within PROTEUS, the interior evolution of rocky planets can be handled by Aragog, a Python package that models the one-dimensional thermal and dynamical evolution of rocky mantles in a solid, molten, or mixed-phase state. Aragog is primarily a Python-based implementation of the original SPIDER code developed in C, with some modifications (Bower et al. [2018]). For more details on the overall working principles of PROTEUS, and in particular its interior dynamics module Aragog, which is most relevant to the present study, refer to Section 2.6.

While PROTEUS enables studies of processes relevant to the thermochemical evolution of rocky exoplanets, its original implementation uses a simplified interior structure model limiting its applicability. In particular, it cannot accurately model planets more massive than Earth or those with multi-layer structures defined by user-specified core mass fractions. Additionally, in the original approach, the interior radius is iteratively adjusted within the mantle evolution solver to match the target mass, a method that becomes increasingly inefficient for more massive or compositionally complex planets.

To address these limitations, this thesis integrates Zalmoxis, an independent one-dimensional planetary interior structure solver, into PROTEUS. Zalmoxis determines planetary structure by self-consistently solving the internal structure equations, enabling accurate modeling of rocky exoplanets over a broad mass range as fully differentiated planets with two or three distinct compositional layers based on user-defined core mass fractions. Coupling Zalmoxis with the Aragog mantle evolution module allows PROTEUS to use the self-consistent internal structure solution (including radial profiles of pressure, density, and gravity) as an input for simulating mantle dynamics, effectively decoupling structure determination from thermal evolution and improving both stability and computational performance.

It is worth noting that Zalmoxis does not compute the thermal profile of the planetary interior, as

its structure calculation is based on a temperature-independent equation of state. This simplification is well justified since several studies have shown that incorporating temperature dependence or phase transitions into the EOS does not significantly improve the accuracy of mass-radius estimates for solid exoplanets (Seager et al. [2007], Duffy et al. [2015], Unterborn and Panero [2019]). This is because such models are far more sensitive to bulk compositional parameters, particularly core mass fraction, volatile content, and the presence or absence of atmospheric envelopes, than to uncertainties in the EOS of the rocky interior. For the purposes of this thesis, adopting a temperature-independent EOS and a simplified structural model is therefore sufficient to capture the first-order effects of composition on planetary structure.

Given these considerations, the primary objectives of this thesis are summarized as follows:

- To develop and extend Zalmoxis for modeling the internal structure of rocky exoplanets across a wide mass and composition range, including super-Earths and sub-Neptunes;
- To integrate Zalmoxis into the PROTEUS framework for simulating the coupled thermal and structural evolution of rocky exoplanets;
- To enable robust coupling between Zalmoxis and the Aragog mantle evolution module, allowing for more self-consistent simulations of thermochemical evolution;
- To explore how effectively the Zalmoxis-Aragog pipeline within PROTEUS models the evolution of fully molten rocky exoplanets across $1 - 7 M_\oplus$ under the current limitations of Aragog.

The remainder of this thesis is structured as follows: Section 2 presents a detailed description of the methodology, including the development and implementation of the Zalmoxis code, both as a standalone tool and integrated within the PROTEUS framework. This section also provides an overview of the existing PROTEUS framework and the under-development Aragog mantle evolution module, thereby contextualizing their respective roles in the simulation workflow, as Aragog utilizes outputs from Zalmoxis within PROTEUS. Section 3 reports on the validation and performance of Zalmoxis, including a fiducial case study demonstrating its use within PROTEUS. Additionally, Section 3 explores the capability of the coupled Zalmoxis-Aragog pipeline within PROTEUS to simulate the evolution of fully molten rocky exoplanets across the $1 - 7 M_\oplus$ range, under the current limitations of Aragog. A discussion of the results is presented in Section 4, and the thesis concludes with a summary of key findings and future work directions in Section 5.

2 METHODOLOGY

2.1 Overview of methods

To model the internal structure and composition of solid exoplanets, the one-dimensional, spherically symmetric planetary interior model Zalmoxis was implemented and substantially extended in the context of this thesis. The code solves the standard set of planetary structure equations under the assumption of hydrostatic and thermodynamic equilibrium, integrating from the planet's center to its surface.

The original version of Zalmoxis was a minimal implementation designed solely to model Earth, with a fixed two-layer structure and hardcoded parameters. To enable its use for a broader range of planetary types, the code was significantly extended to support up to three distinct layers (core, mantle, and volatile-rich envelope) and can now model planets with masses up to 50 $M_\oplus$. With these extensions, users can now specify input parameters such as total mass, layer-specific mass fraction, and material compositions, provided an appropriate EOS is available to relate pressure and density.

The extended Zalmoxis implementation supports key planetary materials including iron (Fe), magnesium silicate ($MgSiO_3$), and water (H_2O), allowing simulations of rocky super-Earths and icy water worlds of up to 50 $M_\oplus$ (see Fig. 2.1). The upgraded model was also integrated into the PROTEUS framework, following the modular design principles of its static interior solver, to facilitate coupled interior–atmosphere evolution simulations.

2.2 Interior model

The internal structure of a spherically symmetric planetary body in hydrostatic and thermodynamical equilibrium is determined by integrating a system of coupled differential equations that describe how mass, pressure, and gravitational acceleration vary with radial distance from the center of the planet.

The first equation describes how the enclosed mass $m(r)$ changes with radius r:

$$\frac{dm(r)}{dr} = 4\pi r^2 \rho(r) \tag{2.1}$$

where $\rho(r)$ is the density at radius r, corresponding to the spherical shell thickness dr.

The second equation represents the condition of hydrostatic equilibrium, where the inward gravitational force is balanced by the outward pressure

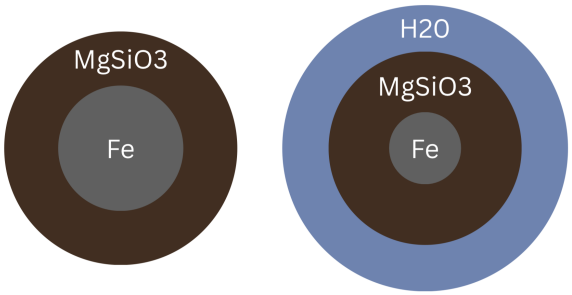

Figure 2.1: Schematic representations of planetary types that can be modeled with Zalmoxis, following Seager et al. [2007]. Left: Super-Earths composed of 32.5% Fe core and 67.5% $MgSiO_3$ mantle by mass. Right: Ganymede-like water-rich planets consisting of 45% H_2O, 48.5% $MgSiO_3$, and 6.5% Fe by mass. The figures are approximately to scale in terms of planetary radius for a 1 Earth-mass planet. Zalmoxis also supports modeling of differentiated core-less planets with silicate mantles and water ice layers, as well as pure iron, pure silicate, and pure water ice compositions.

gradient:

$$\frac{dP(r)}{dr} = -\rho(r)g(r) \tag{2.2}$$

where $P(r)$ is the pressure at radius r and $g(r)$ is the local gravitational acceleration.

The third equation describes how the gravitational acceleration $g(r)$ varies with radius r:

$$\frac{dg(r)}{dr} = 4\pi G\rho(r) - \frac{2g(r)}{r} \tag{2.3}$$

and is obtained by differentiating the gravitational acceleration (Noack et al. [2016]):

$$g(r) = \frac{Gm(r)}{r^2} \tag{2.4}$$

and then substituting Eq. 2.1 and 2.4 appropriately.

Together, Eq. 2.1 to 2.3 are solved numerically alongside an appropriate EOS, which provides the necessary relation between pressure $P(r)$ and density $\rho(r)$ (see Sect. 2.4). The integration of Eq. 2.1 to 2.3 is performed using a numerical solver (`solve_ivp` with the Runge-Kutta method) and proceeds outward from the planetary center to the surface over a discretized radial grid. At the planet's center ($r = 0$), the inner boundary conditions set the central pressure to an initial guess, while both mass and gravity are initialized to zero, consistent with physical expectations.

The outer boundary conditions are defined by a target surface pressure, chosen as 1 atm (representing Earth-like surface conditions), and the total mass of the planet. The solver iteratively adjusts the central pressure and density profiles to match this target at the planet's surface. During integration, material transitions (such as from core to mantle or mantle to an outer volatile layer) are handled by comparing the enclosed mass to user-defined mass fractions that specify layer boundaries.

At each step, the relevant EOS is applied depending on the local composition and pressure regime to accurately capture the density-pressure relationship for each material layer (e.g., iron core, silicate mantle, water envelope). The iterative process continues until convergence is achieved, specifically when the calculated total planetary mass and surface pressure match the user-defined boundary conditions within specified numerical tolerances. The resulting radial profiles of pressure, density, and gravity represent a self-consistent interior structure solution that satisfies the physical constraints of mass, pressure, and composition throughout the planet.

In addition to the planetary interior structure equations (Eq. 2.1 to 2.3), several assumptions and empirical scaling relations are implemented in Zalmoxis to initialize the integration and guide convergence. One key input is an initial estimate of the planet's radius, which is required to set up the radial grid. This is done using a mass-radius scaling law derived by Noack and Lasbleis [2020] as a function of total planetary mass M_p and weight iron fraction X_{Fe}:

$$R_p = 1000(7030 - 1840\, X_{\mathrm{Fe}}) \left(\frac{M_p}{M_\oplus}\right)^{0.282} \tag{2.5}$$

where $M_\oplus$ is Earth's mass.

Equation 2.5 accounts for the dependence of bulk density on iron content. Notably, X_{Fe} here refers to the total weight fraction of iron in the planet, not just the mass fraction located in the core.

Initial estimates for the mass of individual layers are also provided. The core mass M_{core} is evaluated as:

$$M_{\mathrm{core}} = X_{\mathrm{CMF}} M_p \tag{2.6}$$

where X_{CMF} is the core mass fraction of the planet.

Similarly, if an additional compositional layer on top of the core and mantle is present (such as an water outer layer), the combined mass of the core and mantle is evaluated using:

$$M_{\mathrm{core+IM}} = (X_{\mathrm{CMF}} + X_{\mathrm{IMF}}) M_p \tag{2.7}$$

where X_{CMF} and X_{IMF} are the mass fractions of the core and mantle, respectively. The remaining planetary mass fraction is then attributed to the outer water layer.

An initial estimate for the central pressure is required to start the numerical integration of the interior structure equations. This estimate is obtained using a scaling relation derived from dimensional

analysis of the hydrostatic equilibrium equation, given by:

$$P_p = P_E \left(\frac{M_p}{M_E}\right)^2 \left(\frac{R_p}{R_E}\right)^{-4} \tag{2.8}$$

where R_E is Earth's radius and P_E is the Earth's pressure at its center of $\sim 365\,\mathrm{GPa}$ (Nimmo [2015]).

2.3 Setup parameters

Zalmoxis requires a number of other parameters that define the physical setup and numerical behavior of a given simulation. These are organized into functional categories in the configuration file, as follows:

Input Parameters This category specifies the fundamental property of the planet that acts as the primary input for the internal structure model.

- `planet_mass`: Total mass of the planet in kg (set to Earth's mass in the default configuration file).

Assumptions and Initial Guesses The following parameters define the initial compositional structure of the planet and help the solver converge on a physically consistent solution:

- `core_mass_fraction`: Fraction of the total planetary mass allocated to the core (e.g., 0.325 for Earth).
- `inner_mantle_mass_fraction`: Fraction of the total planetary mass assigned to a distinct silicate mantle layer beneath the outer volatile layer. Introduced to describe three-layer planets, this parameter is the second mass fraction needed to specify the interior structure after the core mass fraction. Currently, it differentiates between a silicate mantle and an outer water ice shell. Throughout the rest of this thesis, this parameter will be referred to as the *secondary mass fraction parameter*s.
- `weight_iron_fraction`: Planetary iron fraction by weight, used for providing an initial estimate of the planet's radius using Eq. 2.5.

Equation of State Specifies the material model to be used for the planet's internal layers:

- `choice`: Determines which tabulated EOS to apply (e.g., `Tabulated:iron/silicate`, `Tabulated:water`).

Calculation Settings These settings define the resolution of the planetary interior model:

- `num_layers`: The number of concentric layers into which the planet is divided is set to 150 in the default configuration. While increasing this number can improve radial resolution, it also leads to slightly higher computational cost. However, the yielded model results remain largely consistent beyond this default setting, indicating that 150 layers offer a sufficient balance between accuracy and efficiency.

Iterative Process Parameters These parameters govern the nested iterative solver, described in more detail in Section 2.5:

- `max_iterations_outer`, `tolerance_outer`: Control the outer loop, which ensures overall convergence of mass and, implicitly, radius. The convergence tolerance is interpreted in SI mass units within the code (set to 10^{-3} in the default configuration file).
- `max_iterations_inner`, `tolerance_inner`: Control the inner loop, used for convergence of the density profile. The convergence tolerance is expressed in SI density units in the code (set to 10^{-4} in the default configuration file).
- `relative_tolerance`, `absolute_tolerance`: Passed to the numerical integrator (`solve_ivp`) to control integration accuracy (set to 10^{-5} and 10^{-6} respectively in the default configuration file).

Surface Pressure Adjustment After initial integration, the surface pressure may not match a target value. This block defines how to adjust central pressure to achieve a match:

- `target_surface_pressure`: The desired pressure at the outer boundary in Pa (set to 1 atm for Earth-like surface conditions in the default configuration file).
- `pressure_tolerance`: Allowed deviation of the surface pressure in Pa from the target surface pressure (set to $10^9\,\mathrm{Pa}$ in the default configuration file).
- `max_iterations_pressure`: Number of iterations allowed for pressure convergence.
- `pressure_adjustment_factor`: Scaling factor used to update the central pressure guess in response to mismatches at the surface. If the model's calculated surface pressure differs from the target by ΔP, the next central pressure guess is updated by subtracting $\Delta P \times$ `pressure_adjustment_factor`. A factor > 1 accelerates convergence but may risk overshooting; a factor < 1 slows convergence but increases stability. This factor is set to

1.1 in the default configuration file and has been tested to work robustly for simulations of planets with masses between 1 and 50 $M_\oplus$, for both planetary types described in Fig. 2.1.

2.4 Equations of state

To close the system of differential equations governing planetary interiors, an EOS must be specified for each material layer considered. As mentioned by Seager et al. [2007], Duffy et al. [2015], Unterborn and Panero [2019], the inclusion of temperature-dependent EOSs or the modeling of phase transitions does not significantly enhance the accuracy of bulk composition estimates derived from mass and radius measurements of solid exoplanets. Consequently, this work adopts zero-temperature EOSs ($\sim 300\,\mathrm{K}$), which offer computational efficiency while remaining physically motivated for the modeling of planetary interiors.

The EOSs for iron, silicates, and water used in this study are adopted from the parametrizations provided by Seager et al. [2007], developed for a wide range of planetary masses. Their framework assumes uniform low interior temperatures and applies distinct EOS prescriptions depending on the pressure regime: below 200 GPa, fits to experimental static compression data are used; above $\sim$ 10000 GPa, the TFD theoretical EOS is adopted due to the breakdown of conventional electron gas assumptions; and in the intermediate regime, Vinet and Birch-Murnaghan fits are applied to Fe and $MgSiO_3$, respectively.

Accordingly, the EOSs adopted in Zalmoxis are shown in Figure 2.2 and are as follows (see Section 3 of Seager et al. [2007] and references therein for further details):

- Core: Iron, modeled in Seager et al. [2007] using the Vinet fit to the ϵ-phase EOS of Fe and TFD theory;
- Mantle: Silicate, modeled in Seager et al. [2007] using the fourth-order Birch-Murnaghan EOS fit to $MgSiO_3$ perovskite and TFD theory;
- Outer water layer: Water ice, modeled in Seager et al. [2007] using experimental data, DFT predictions for water ice in phases VIII and X, and TFD theory.

The outer water layer is included only when modeling water-rich planets, where a volatile-rich envelope overlays a rocky (iron-silicate) interior. Following the methodology of Seager et al. [2007], Zalmoxis iteratively transitions between material layers based on specified mass fractions, beginning from an initial mass guess. This approach enables the simulation of layered, compositionally differentiated interiors with EOSs appropriate for each material over the relevant pressure ranges. Two primary classes of planets are supported by Zalmoxis: rocky super-Earths, composed of an iron core and silicate mantle, and water-rich planets, which additionally feature an outer envelope composed of H_2O. Below, the configuration setups required to model each of these classes within Zalmoxis are described, along with relevant physical assumptions and examples.

2.4.1 Super-Earths

To simulate a rocky exoplanet with an Earth-like composition, Zalmoxis can be configured to model a fully differentiated two-layer structure consisting of an iron core and a silicate mantle. A common choice in the literature for such rocky planets is a CMF of 32.5%, which reflects the typical value inferred for Earth and is often used as a baseline for modeling terrestrial exoplanets. This is implemented in Zalmoxis by setting a core mass fraction of 0.325 and a weight iron fraction of 0.325, under the assumption that all of the planet's iron resides in the core. Additionally, the equations of state for iron and silicate layers are selected from the models provided by Seager et al. [2007], as discussed above.

It is important to note that the secondary mass fraction parameter must be set to zero in this case because it is only relevant when modeling three-layer planets. This parameter was introduced to allow users to specify a second independent mass fraction when configuring interiors with more than two layers, such as in water-rich planets where both the core and mantle mass fractions must be defined explicitly. In two-layer models like these Super-Earths, only the core mass fraction is needed, and the mantle occupies the remainder of the planetary mass by default.

Such a configuration is not only suitable for modeling massive rocky exoplanets (super-Earths), but can also approximate the rocky cores of sub-Neptunes, planets with significant gas or volatile envelopes atop Earth-like interiors. Zalmoxis can in principle be used to approximate the interior structure of such cores, the modeling of gaseous envelopes and atmospheric layers lies beyond the scope of this thesis and is not considered further here.

2.4.2 Water-rich planets

To model water-rich planets, Zalmoxis supports fully differentiated three-layer configuration composed of an iron core, a silicate mantle, and an outer volatile-rich water ice layer. For instance, a representative composition, similar to that proposed for Ganymede by Seager et al. [2007], can be simulated by setting the core mass fraction to 6.5%

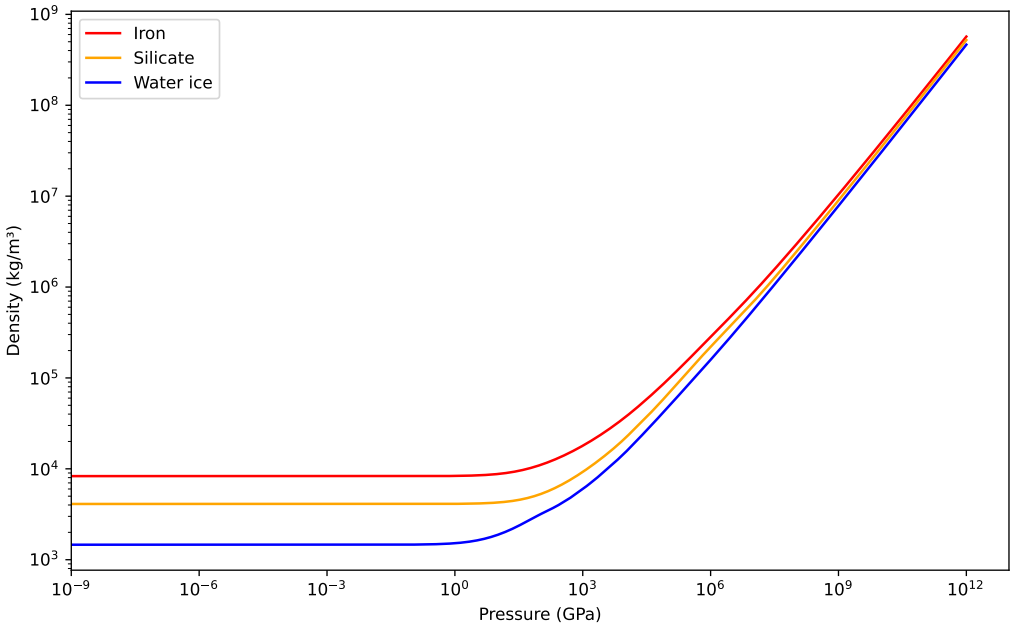

Figure 2.2: EOSs for iron, silicates, and water ice used in Zalmoxis, adopted from the parametrizations provided by Seager et al. [2007].

and the secondary mass fraction to 48.5%, leaving the remaining 45% for the water layer. Again, it is assumed that all the iron is fully contained in the core, so the weight iron fraction is set equal to the core mass fraction. The equations of state for the iron, silicate, and water ice layers are selected from the models provided by Seager et al. [2007], as discussed above. This setup enables the modeling of icy or volatile-rich exoplanets with layered interiors. While this structure is particularly suited for simulating water worlds, it could also serve as a basis for exploring more complex multi-layered planetary compositions. However, the inclusion of additional volatile species or atmospheric effects lies beyond the scope of this thesis.

2.5 Shooting Method

The shooting method is a numerical approach to solve boundary value problems by transforming them into initial value problems. Instead of attempting to satisfy boundary conditions at both ends simultaneously, the method starts by guessing unknown initial conditions (usually at the center of the domain) and then integrates the governing differential equations outward. After integration, the computed solution at the boundary is compared to the target boundary condition. If the boundary condition is not met, the initial guess is adjusted, and the integration is repeated. This iterative process continues until the solution converges within a predefined tolerance.

Within Zalmoxis, the shooting method is utilized to determine a self-consistent pressure and density profile throughout the planet that satisfies a specified surface pressure. Since the central pressure of the planet is initially unknown but required to solve the system of coupled differential equations governing mass, gravity, and pressure as functions of radius, an initial guess for the central pressure is made. The system of ODEs is then integrated outward from the center to the surface using `solve_ivp`. The pressure obtained at the surface is compared to the target surface pressure defined in the configuration. If the difference exceeds the prescribed tolerance, the central pressure guess is updated by applying the difference scaled by an adjustment factor, and the integration is repeated. To ensure numerical stability and physical consistency, Zalmoxis enforces positivity and convergence of all pressure values throughout the planetary interior, preventing numerical instabilities that could arise if pressure fails to converge or becomes nonphysical during the integration.

Zalmoxis is structured with three main nested iterative loops. The shooting method constitutes the innermost loop, responsible for adjusting the central pressure guess and performing the outward integration to ensure that the surface boundary condition on pressure is satisfied. Outside this innermost loop, additional iterative processes update the density profile based on the revised pressure, and recalculate parameters such as the planet's

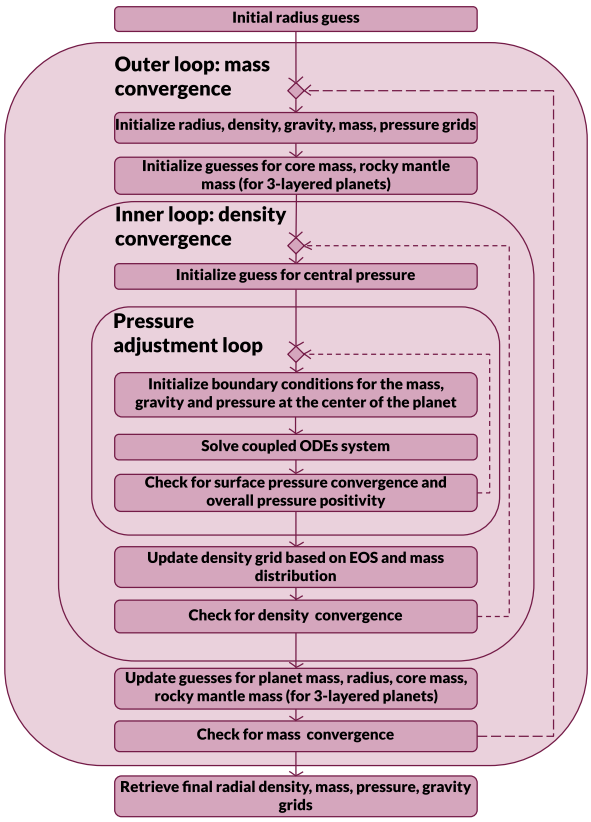

Figure 2.3: Schematic representation of the workflow in Zalmoxis, illustrating the iterative process from top to bottom. The process begins with an initial radius guess based on Eq. 2.5. Initial guesses and subsequent updates for core and rocky mantle masses are set using Eq. 2.6 and 2.7, respectively. The central pressure guess is set using Eq. 2.8. Dashed arrows trace the backward flow of control in the code, indicating which steps are repeated if convergence is not yet achieved. These nested iterations update the structural parameters until all physical and numerical constraints are satisfied.

radius and core-mantle boundary mass fractions. These nested iterations continue until the total planetary mass converges to the target value. Collectively, these iterations refine the planet's internal structure until all physical constraints, including total mass and surface pressure, are fulfilled. A schematic overview of this workflow is illustrated in Figure 2.3.

To illustrate its performance, Zalmoxis requires only 4 iterations and $\sim 5\,\mathrm{s}$ to compute the internal structure of a 1 $M_\oplus$ Earth-like planet, and 6 iterations with a runtime of $\sim 1.3\,\mathrm{min}$ for a 50 $M_\oplus$ Earth-like planet. These results demonstrate both fast convergence and computational efficiency, even for large planets, making Zalmoxis particularly well-suited for integration into larger planetary evolution models, such as PROTEUS, where minimizing computational overhead is crucial for exploring extensive parameter spaces.

2.6 General working principles of PROTEUS

This section first outlines the core workflow of the PROTEUS framework and then emphasizes key features of its interior dynamics module, Aragog, relevant to this study. An overview of the interconnected modules and processes handled by PROTEUS is illustrated in Figure 2.4, highlighting the interaction between the planetary interior, surface, and atmospheric escape processes.

Simulations in PROTEUS usually start with the planet in a fully molten state, where the interior and atmosphere are linked to facilitate heat transfer from the mantle to space. At each timestep, the stellar flux at the top of the atmosphere is updated based on the MORS stellar evolution models developed by Johnstone et al. [2021]. Interior evolution is handled by the Aragog module, which then computes the temperature at the top of the mantle, governed by surface boundary conditions that balance conductive heat transfer with outgoing radiative flux from the atmosphere. The

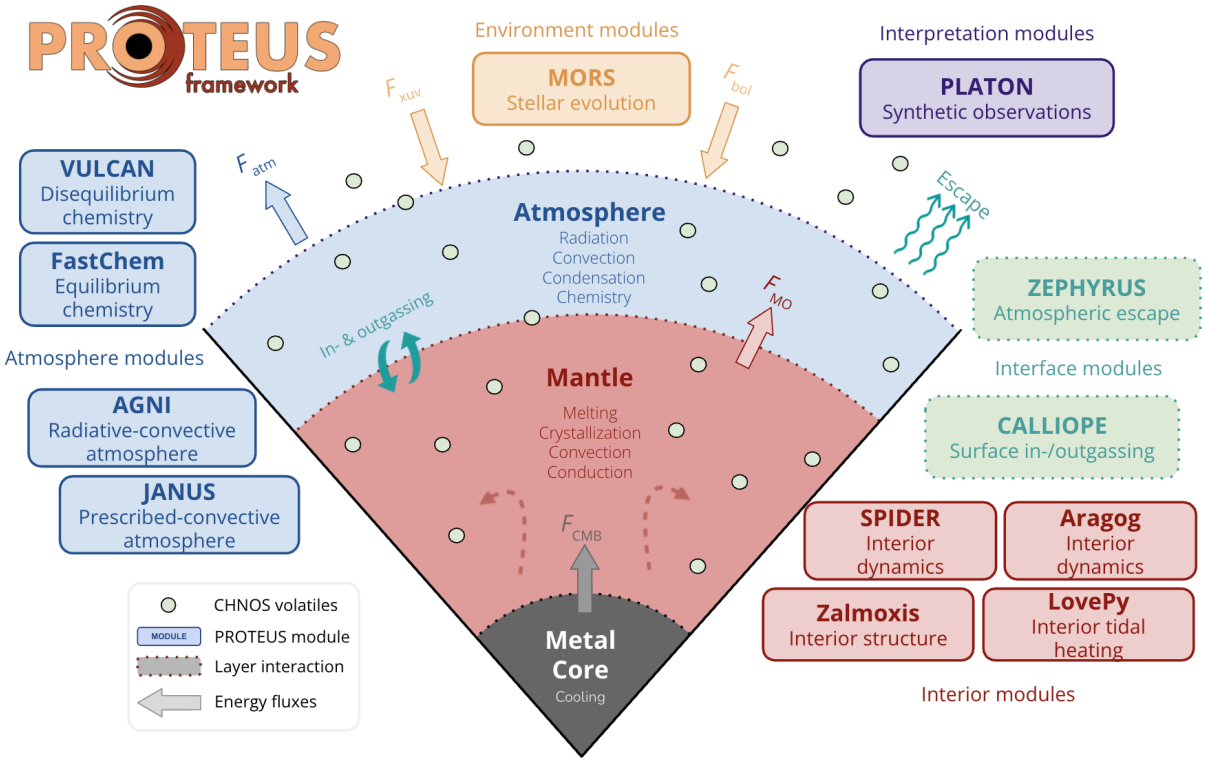

Figure 2.4: Modular architecture of the PROTEUS framework. PROTEUS is designed to simulate the coupled evolution of planetary interiors and atmospheres on geological timescales. It consists of interconnected modules categorized into interior, atmosphere, environment, interface, and interpretation components. Interior dynamics are handled by solvers such as Aragog and SPIDER, which model mantle convection, melting, and crystallization, while Zalmoxis provides a self-consistent solution to planetary internal structure. The LovePy module accounts for interior tidal heating. The AGNI and JANUS modules simulate radiative-convective or prescribed-convective atmospheric evolution, respectively, complemented by chemical models like FastChem (equilibrium) and VULCAN (disequilibrium). The framework also includes CALLIOPE for volatile in-/outgassing at the surface and ZEPHYRUS for atmospheric escape, with MORS controlling stellar forcing. Energy and volatile fluxes (e.g., F_{atm}, F_{XUV}, F_{bol}, F_{MO}, F_{CMB}) dynamically couple interior and atmospheric layers. The PLATON module enables the generation of synthetic observations for comparison with data. Modules exchange key variables like CHNOS volatiles and energy fluxes to enable time-dependent simulations of rocky exoplanet evolution. Figure by Emma Postolec, reproduced with permission from Lichtenberg et al. [in prep].

coupled system evolves forward in time by recalculating these fluxes and temperatures, enabling a consistent treatment of heat and volatile exchange between planetary layers. For a more detailed description of this coupled evolution and the model implementation, see Nicholls et al. [2024].

Additionally, at every timestep, PROTEUS checks whether predefined termination criteria are met to decide whether the simulation should stop. These criteria include reaching a specified number of iterations or model time, the solidification of the mantle (i.e., when the global melt fraction drops below a critical threshold, typically 0.01), achieving radiative equilibrium (where the difference between outgoing and incoming radiation falls within a set tolerance), or a drop in surface pressure below a specified value. If none of these conditions are satisfied, the system continues evolving, allowing PROTEUS to robustly simulate the transition from magma ocean states to solidified planetary interiors with coupled atmospheric evolution.

One of the key distinctions between Aragog and the SPIDER model is that Aragog operates in temperature space, whereas SPIDER was formulated in entropy space. As a result, the energy conservation equation, as well as the treatment of melt fraction, are expressed directly in terms of temperature in Aragog.

The energy conservation equation solved in Aragog reads:

$$\rho c_p \frac{\partial T}{\partial t} = -\nabla \cdot (\mathbf{J}_{cond} + \mathbf{J}_{conv}) + \rho H \tag{2.9}$$

with the conductive and convective heat fluxes defined respectively as:

$$\mathbf{J}_{cond} = -k \nabla T \tag{2.10}$$

$$\mathbf{J}_{conv} = -\rho c_p \kappa_h \left(\nabla T - (\nabla T)_S\right) \tag{2.11}$$

Here, ρ is the density of the mantle material, c_p is the specific heat capacity at constant pressure, T is the temperature, and H denotes internal heat production from radiogenic and tidal sources.

In the original SPIDER formulation, the total heat flux includes not only conductive and convective components ($\mathbf{J}_{cond}$ and $\mathbf{J}_{conv}$) but also additional contributions from mixing and gravitational separation between melt and solid phases. These are represented by $\mathbf{J}_{mix}$ and $\mathbf{J}_{grav}$, respectively, and are added to the total energy flux in the energy conservation equation (Eq. 2.9). However, these terms have not yet been implemented in Aragog and remain exclusive to SPIDER (Bower et al. [2018]). Their absence means that Aragog currently neglects the energetic effects of phase redistribution processes during melt migration, which may be important in fully capturing thermochemical evolution in partially molten planets.

Due to Aragog's temperature-based formulation, the melt fraction is computed using a linear interpolation between the solidus and liquidus temperatures:

$$\phi_{\text{no clip}} = \frac{T - T_{\text{solidus}}}{T_{\text{liquidus}} - T_{\text{solidus}}} \tag{2.12}$$

where T_{solidus} is the temperature below which the material is completely solid and T_{liquidus} is the temperature above which it is fully molten.

This formulation means that the melt fraction varies linearly with temperature between the solidus and liquidus limits. Below the solidus, is less than zero, indicating no melt, while above the liquidus, it exceeds one, implying a fully molten state. To maintain physical realism, Aragog clips the computed melt fraction to the range $[0, 1]$, ensuring that the final value reflects a physically valid proportion of molten material. This guarantees that the final melt fraction reflects a valid proportion of melted material, regardless of the computed value.

To run its interior evolution simulations, Aragog requires a discretized planetary mesh that contains pressure and density values as a function of depth. This mesh is initialized by solving for the hydrostatic pressure distribution within the planet using an equation of state. By default, Aragog adopts the Adams-Williamson EOS (AWEOS), which assumes adiabatic compression of a chemically homogeneous interior. The equation takes the form (Bower et al. [2018]):

$$P = -\frac{\rho_r g}{\beta}(e^{\beta z} - 1) \tag{2.13}$$

where ρ_r is a reference surface density, g is the gravitational acceleration, ρ_r is a quantity describing the compressibility of the material, and z is the depth (Bower et al. [2018]). SPIDER, and subsequently Aragog, assumes that g is approximately constant throughout the mantle and solves for ρ_r and β by applying a least-squares fit to the lower mantle's density profile (Dziewonski and Anderson [1981], Bower et al. [2018]).

However, the use of AWEOS is not suitable for higher-mass planetary simulations since the assumption of constant gravitational acceleration (g) throughout the mantle breaks down. In more massive planets, gravity varies significantly with depth due to increasing pressure and varying internal density. This variation affects the pressure and density profiles in a way that AWEOS's simplified exponential model cannot accurately capture. Moreover, AWEOS assumes a chemically homogeneous, adiabatic interior, which neglects the presence of compositional layering, that is used in modeling planetary interiors.

2.7 Zalmoxis in PROTEUS

The limitations associated with the use of AWEOS discussed in Sec. 2.6 motivate the introduction of Zalmoxis into PROTEUS. Zalmoxis computes self-consistent radial profiles of pressure, density, and gravity that account for depth-dependent variations in composition. These profiles replace the role previously filled by the AWEOS in Aragog, providing a more physically accurate discretized mesh. This enhanced mesh is then passed to Aragog, which uses it as the foundation for improved thermal evolution simulations.

Another key conceptual advancement introduced by integrating Zalmoxis into PROTEUS lies in how planetary radius is determined. In the original PROTEUS solver, the planetary interior was modeled using a root-finding algorithm, where the interior mantle evolution model iteratively adjusted the mantle radius until the target planetary mass was achieved. In contrast, Zalmoxis determines the planetary structure directly by solving the coupled internal structure equations. The resulting radial pressure, density, and gravity profiles for the mantle are then passed to the interior mantle evolution module, Aragog, which is executed once per model to compute thermochemical properties based on the converged structure, rather than being part of the iterative radius-determination process.

The integration of Zalmoxis into PROTEUS was accomplished by incorporating three core components from the Zalmoxis codebase. First, the main solver function, which executes the forward integration of the planetary structure, solves the coupled differential equations for mass, pressure, and radius under specified convergence constraints. Second, the material-specific density evaluation function is used to compute the local density from the equation of state, based on the local pressure and the material identity at each point within a planetary layer (e.g., core or mantle). Third, the system

of first-order differential equations governing the planet's internal structure is wrapped by an ODE coupling function, which ensures consistent integration across compositional boundaries.

Zalmoxis can be enabled within the PROTEUS framework by selecting it as the internal structure solver in the configuration file under the `structure` block. This allows planetary interiors to be modeled consistently within PROTEUS's broader evolutionary pipeline. To model the planetary types described in Sections 2.4.1 and 2.4.2, a minimal setup requires specifying the mass fraction of the core and, for three-layer planets, the secondary mass fraction of the silicate mantle. The remaining mass is automatically assigned to the outermost volatile layer (typically water ice). In addition, the total planetary weight iron fraction must be provided, along with the number of radial integration layers (commonly 100) to ensure sufficient resolution. Finally, appropriate equations of state must be selected, for example, tabulated models for iron and silicate for rocky planets, or models including water ice for volatile-rich planets with an Earth-like rocky interior.

Given a target planetary mass specified in the PROTEUS configuration file, the framework first subtracts any volatile contributions to isolate the dry mass of the planet. This volatile-stripped mass is then passed to Zalmoxis for structural modeling. This step ensures that the internal structure is solved only for the condensed (rocky and/or metallic) layers, excluding any low-density volatile envelopes that would otherwise distort the mass-radius relationship. The volatile mass fractions are handled separately and later reintegrated into the full planetary model after the structural solution is complete. This preprocessing step maintains consistency with the assumptions behind the tabulated equations of state used by Zalmoxis.

Under the aforementioned setup, Zalmoxis is responsible for the structural modeling of planetary interiors, while Aragog takes over the evolution of the thermal state once the structural model has been established. This clear separation of tasks provides two significant benefits. First, by decoupling the determination of structure from the subsequent evolutionary processes and removing the need for iterative root-finding, the overall computational runtime per model is substantially reduced, improving efficiency. Second, the integration of Zalmoxis expands the parameter space that can be explored, allowing robust structural modeling across a broader range of planetary masses, compositions, and thermal states than was previously possible.

3 RESULTS

3.1 Model Validation

Validation was conducted both within Zalmoxis and at the workflow level within PROTEUS. The physical accuracy and internal consistency of Zalmoxis outputs were assessed through key benchmark tests (detailed in the remainder of this Section), while the integrated Zalmoxis-PROTEUS workflow was cross-validated by comparing simulation outputs with and without Zalmoxis. This two-level validation confirms the robustness and reliability of the combined modeling approach, providing a solid foundation for the results presented in Sections 3.3 and 3.4.

Typical radial profiles of density, pressure, gravity, and enclosed mass produced by Zalmoxis are shown in Figure 3.1 for planets with masses from 1 to 10 $M_\oplus$. Increasing planetary mass results in higher core densities, pressures, and surface gravities. The pressure profiles smoothly approach zero near the planetary surface for all masses, indicating successful convergence to surface boundary conditions.

The density profiles in the top left panel of Figure 3.1 exhibit steeper gradients and higher central densities with increasing planetary mass, reflecting the increasing degree of compression experienced by the core and mantle materials under stronger gravitational confinement. For instance, while a 1 $M_\oplus$ planet has a central density just under $15000\,\mathrm{kg\,m^{-3}}$, the 10 $M_\oplus$ profile exceeds $25000\,\mathrm{kg\,m^{-3}}$ at the core.

The gravity profiles in the top right panel of Figure 3.1 peak at intermediate depths for each planet, near the core-mantle boundary, before decreasing toward the center and surface, features that are consistent with expectations for layered, spherically symmetric bodies with varying density. Larger planets reach surface gravities above $25\,\mathrm{m\,s^{-2}}$, compared to $10\,\mathrm{m\,s^{-2}}$ for the Earth-like $1M_\oplus$ case.

The pressure profiles shown in the bottom left panel of Figure 3.1 smoothly approach zero near the planetary surface for all masses, indicating successful convergence to surface boundary conditions. These profiles also scale non-linearly with mass, increasing sharply with depth and reaching several TPa in the cores of the more massive planets, following the expected trend from hydrostatic equilibrium under stronger gravity.

The enclosed mass curves shown in the bottom right panel of Figure 3.1 increase monotonically with radius, as expected, but show increasing curvature at depth for higher-mass planets. This reflects the growing concentration of mass toward the interior due to stronger compression effects. The relative compression of material is also visible in how the same radial extent (e.g., 8000 km) en-

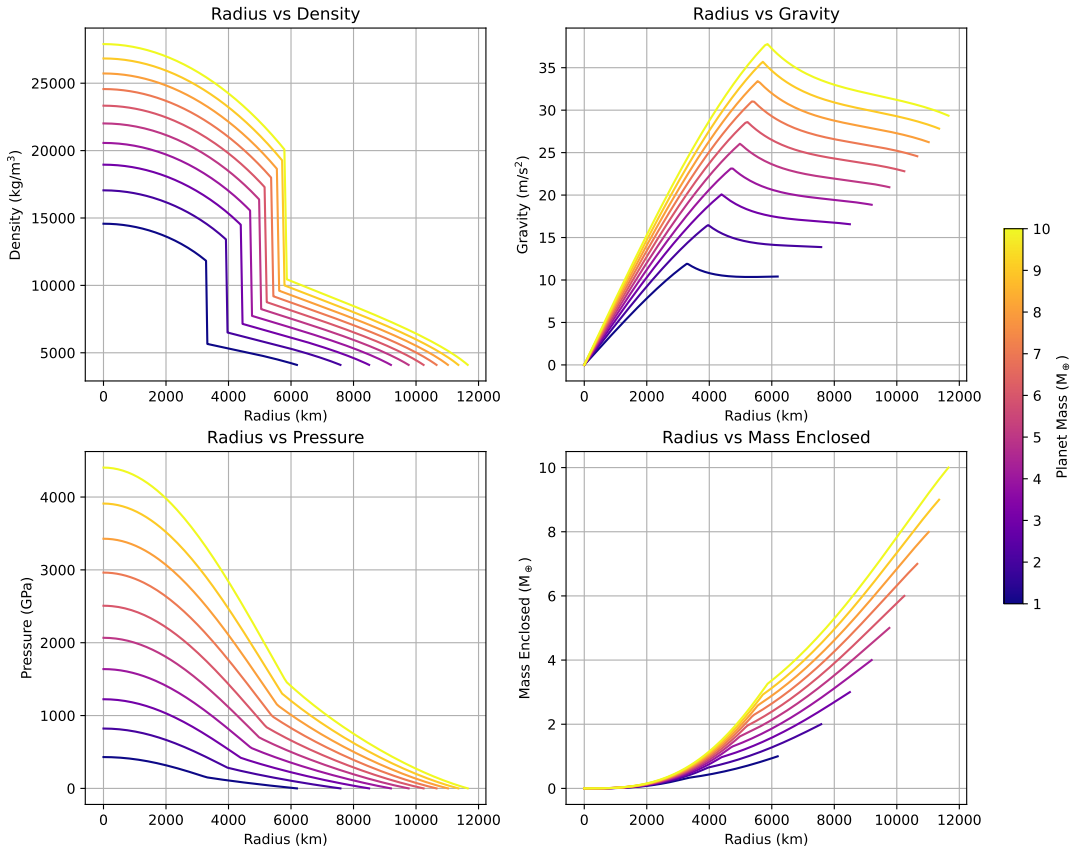

Figure 3.1: Density, gravity, pressure, and mass radial profiles from Zalmoxis for 1 to 10 $M_\oplus$ Earth-like rocky exoplanets (32.5% Fe core and 67.5% $MgSiO_3$ mantle by mass).

closes a greater fraction of total planetary mass for higher-mass planets.

For a rough comparison of pressure and gravity profiles, see the plots in Appendix A, which compare the results modeled with Zalmoxis with those from Boujibar et al. [2020] and Wagner et al. [2012] for Earth-like exoplanets. While deviations are more pronounced in these comparisons due to differing EOS assumptions relative to Seager et al. [2007], the overall trends in gravity and pressure profiles remain consistent, providing a reasonable qualitative validation of the model's output.

The physical accuracy and internal consistency of the profiles produced with Zalmoxis were further evaluated through two primary validation tests: (i) a mass-radius comparison against theoretical relations from Zeng et al. [2019], and (ii) a radial density profile comparison against models presented in Seager et al. [2007]. Both tests were performed with default configuration settings as described in Section 2.3 while adjusting for the appropriate EOS, mass and iron weight fractions of the relevant modeled planets as described in Sections 2.4.1 and 2.4.2. All validation routines are available in the `src/tests` directory of the Zalmoxis repository.

A total of 108 test cases were executed in parallel, completing in under 10 min, with all tests passing successfully. Each test case corresponded to a model generated for a fixed planetary mass. Specifically, 100 mass-radius tests were performed: 50 for terrestrial rocky compositions and 50 for water-rich compositions, covering 50 distinct planetary masses for each type. The remaining 8 tests involved radial density profile comparisons: 4 for each composition type, corresponding to 4 selected masses for comparison with Seager et al. [2007]. The specific test conditions for each case are further detailed in Sections 3.1.1 and 3.1.2 below.

3.1.1 Mass-radius test

The mass-radius relation computed with Zalmoxis was compared against reference curves from Zeng et al. [2019] over the $1 - 50 M_\oplus$ range for two representative compositions: a terrestrial rocky con-

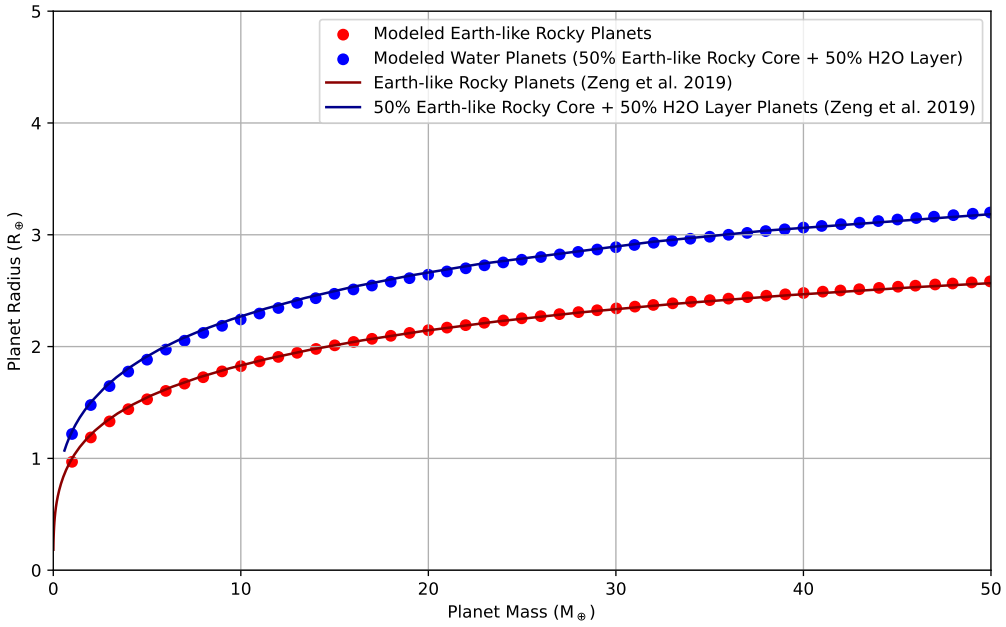

Figure 3.2: Modeled exoplanets against references curves from Zeng et al. [2019] for two cases: terrestrial rocky planets (32.5% Fe core and 67.5% $MgSiO_3$ mantle by mass) and water-rich planets (50% Earth-like rocky core and 50% H_2O outer layer by mass).

figuration (32.5% Fe core, 67.5% $MgSiO_3$ mantle by mass) and a water-rich configuration consisting of a 50% Earth-like rocky interior (16.25% Fe core, 33.75% $MgSiO_3$ mantle by mass) and a 50% H_2O outer layer by mass. The latter was benchmarked against the 300 K isotherm curve assuming a surface pressure of 1 mbar, as reported in Zeng et al. [2019]. The simulations assumed a surface pressure of 1 atm (101325 Pa); however, this discrepancy had negligible impact on the modeled radius due to the low compressibility of water in the relevant pressure regime.

The test was implemented using `pytest` and ran in parallel Zalmoxis for each integer mass in the $1 - 50 M_\oplus$ range. For each composition type, the modeled radius was extracted and compared to the linearly interpolated value of the corresponding reference curve from Zeng et al. [2019]. Agreement within 3% was set for the test to pass. This threshold is within the 5% relative accuracy typically considered acceptable for internal structure models (Luque and Pallé [2022], Lin et al. [2024]). All simulations satisfied this criterion, indicating that the EOS routines and internal structure integration produce physically consistent outputs across a broad range of planetary masses. These results are summarized in Figure 3.2.

3.1.2 Density profile test

The radial density profiles produced by Zalmoxis were validated against the internal structure models of Seager et al. [2007] for two compositions: a fully rocky planet (32.5% Fe, 67.5% $MgSiO_3$) and a mixed water-rich planet (6.5% Fe, 48.5% $MgSiO_3$, and the remainder as H_2O). Using these mass fractions, the test was implemented using `pytest` and ran Zalmoxis for planetary masses of 1, 5, 10, and 50 $M_\oplus$. The resulting density profiles were extracted and compared pointwise to interpolated reference profiles from Seager et al. [2007] by matching radial coordinates, using a relative tolerance of 24% or an absolute tolerance of 1000 $\mathrm{kg\,m^{-3}}$ to assess agreement. To prevent bias from sharp density discontinuities, such as those at the core-mantle boundary, regions surrounding these jumps were excluded from the comparison. Across all tested cases, the density profiles agreed with the reference within the specified tolerances, confirming the model's accuracy in reproducing planetary interior structures. The results of this test are presented in Figure 3.3.

3.2 Model Performance

3.2.1 Radius variability across composition space

Mass-radius relationships were validated for two representative bulk compositions that Zalmoxis is designed to simulate (see Section 3.1.1). These

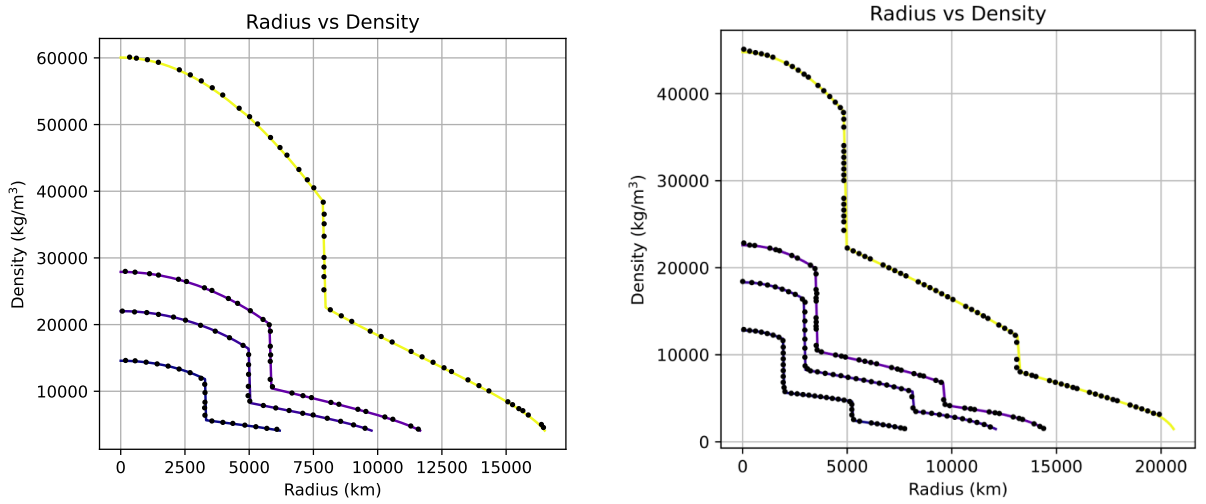

(a) Rocky planets with a 32.5% Fe core and a 67.5% $MgSiO_3$ mantle

(b) Water-rich planets with a 6.5% Fe core, a 48.5% $MgSiO_3$ mantle and a 45% H_2O

Figure 3.3: Comparison of modeled density radial profiles (solid lines) with reference models (scattered points) from Seager et al. [2007] for (a) rocky and (b) water-rich planet compositions. From bottom to top, the profiles correspond to planets with 1, 5, 10, and 50 $M_\oplus$. For each panel, each profile corresponds, from bottom to top, to a planetary mass of 1, 5, 10, and 50 $M_\oplus$.

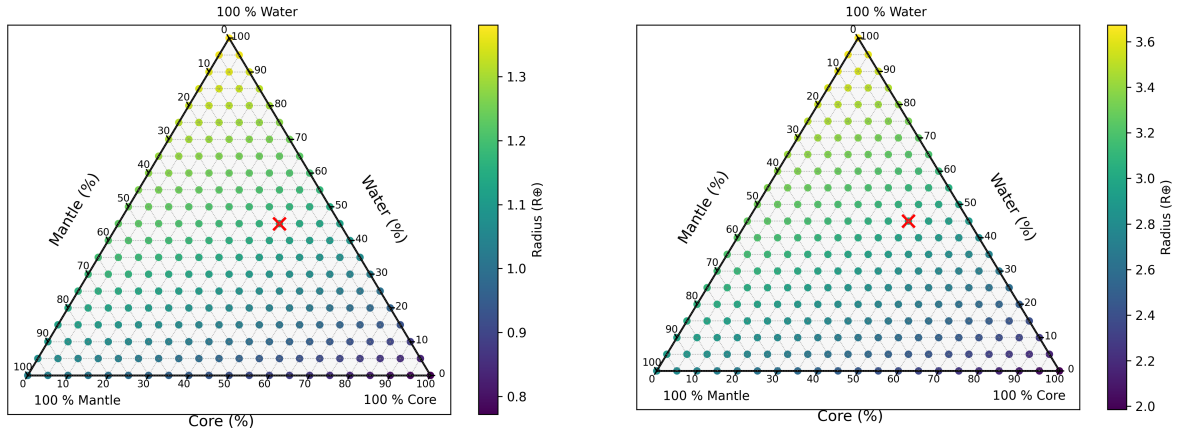

Figure 3.4: Ternary diagrams showing planetary radius variation as a function of iron core, silicate mantle, and water ice layer mass fractions for (a) 1 $M_\oplus$ and (b) 50 $M_\oplus$ planets in the water-rich configuration. Each point corresponds to a unique composition with the same total mass; colors indicate planetary radii normalized to Earth units ($R_\oplus$), as computed by Zalmoxis. Core, mantle, and water mass fractions are shown in percentage units. A reference composition with 40% core, 15% mantle, and 45% water is marked with a red cross. The diagrams highlight the significant radius variability that can arise at fixed mass due to differences in internal structure.

relationships, however, are not unique for three-layer planetary interiors composed of an iron core, silicate mantle, and an outer water ice layer. To illustrate the compositional degeneracy at fixed mass, ternary diagrams were generated for the water-rich configuration of Zalmoxis, following the approach outlined in Huang et al. [2022] and references therein. Boundary masses of 1 and 50 $M_\oplus$ were selected to explore the variability in radius across the full range of allowed layer mass fractions. The resulting ternary plots (Figure 3.4) show significant variation in planetary radius across composition space: at 1 $M_\oplus$, radii span more than $\sim 1.3 R_\oplus$, while at 50 $M_\oplus$, the variation exceeds $\sim 3.6 R_\oplus$. At fixed planetary mass, water-rich compositions generally yield the largest radii due to the low density of water compared to silicate or iron. These results emphasize that planetary radius alone does not uniquely determine interior structure, particularly for high-mass planets with diverse compositions.

3.2.2 Model runtime variability across composition space

To assess how composition affects computational performance, ternary diagrams were generated us-

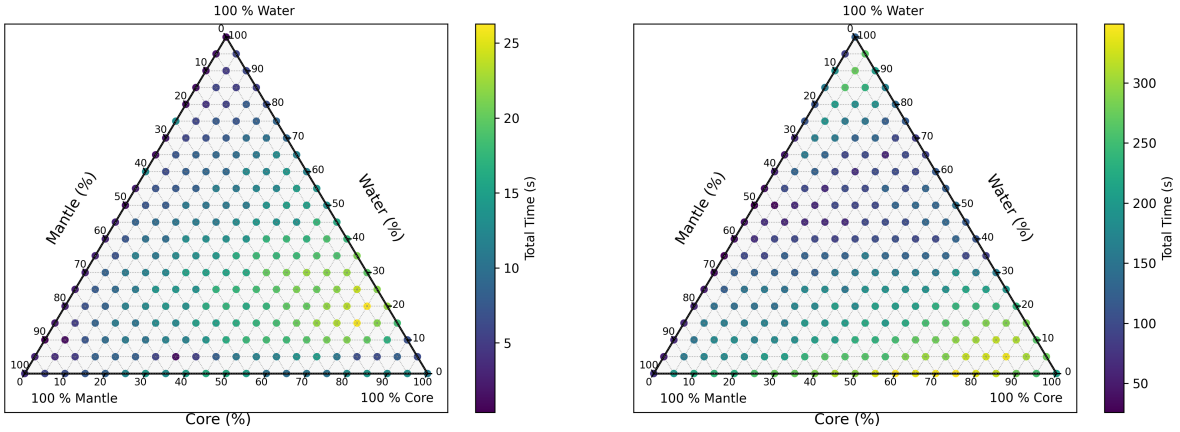

Figure 3.5: Ternary diagrams showing model runtime variation as a function of iron core, silicate mantle, and water ice layer mass fractions for (a) 1 $M_\oplus$ and (b) 50 $M_\oplus$ planets in the water-rich configuration. Each point corresponds to a unique composition with the same total mass; colors indicate model runtimes required to complete the simulations. as computed by Zalmoxis. Core, mantle, and water mass fractions are shown in percentage units. The diagrams illustrate how simulation time depends on both total mass and internal structure.

ing the same three-layer interior structure as in the radius analysis in Section 3.2.1, but displaying model runtime instead of radius. Overall, the runtime of Zalmoxis increases with total planetary mass. Ternary plots of model runtime (Figure 3.5) reveal that for 1 $M_\oplus$, simulations typically complete in under 26 seconds, while for 50 $M_\oplus$, runtimes complete in under 400 seconds. At fixed planetary mass, simulations of iron-rich compositions generally require the most time to converge. Runtime is observed to exhibit a weak correlation with the silicate mantle mass fraction, as indicated by the relatively uniform color distribution along the mantle axis in the ternary diagrams. This suggests that variations in mantle fraction have a smaller impact on model runtime compared to variations in core or water layer fractions.

3.3 Fiducial Case for Zalmoxis usage in PROTEUS

3.3.1 Setup and initial conditions

To assess the behavior of Zalmoxis in the broader planetary evolution context, a fiducial simulation was conducted using the PROTEUS framework. The modeled planet was a 1 $M_\oplus$ Earth-like rocky exoplanet with a core mass fraction and an iron weight fraction set to 0.325, under the assumption that all iron is sequestered in the core. The equation of state was selected to represent a metallic iron core and a silicate mantle, following the tabulated models from Seager et al. [2007].

The initial volatile inventory was defined using a simplified but physically motivated CHNOS composition to describe the hydrogen, carbon, nitrogen, and sulfur abundances. The total hydrogen content was set to $\mathrm{H}_{oceans} = 1.0$, corresponding to one Earth ocean equivalent of hydrogen mass, a common reference point in terrestrial planet modeling (Nicholls et al. [2024]). The carbon-to-hydrogen mass ratio was set to C/H = 1.0, and the nitrogen abundance was specified as $N = 1.0$ ppmw (parts per million by weight) relative to the mantle mass, in agreement with estimates for primitive Earth conditions (Wang et al. [2018], Nicholls et al. [2024]). The sulfur-to-hydrogen mass ratio was set to S/H = 2.0, representing a moderately sulfur-rich scenario that may influence redox state and outgassing behavior.

To resolve the early, rapid evolution of the planet with greater fidelity, the time-stepping parameters were carefully tuned from their default values. The absolute minimum time step was reduced from 10^4 to 10^2 years, and the relative minimum from 10^{-5} to 10^{-6}, enabling smaller steps during phases of rapid change. The initial step size was decreased from 30 years to 1 year, ensuring that the onset of mantle cooling and melt evolution was more accurately resolved. To further improve numerical precision during critical thermal transitions, the adaptive solver tolerances were tightened (with absolute and relative tolerances set to 0.005 and 0.05, respectively, from default values of 0.02 and 0.1). These modifications were made with the broader objective of determining whether similar evolutionary pathways, such as the persistence of deep magma oceans or delayed mantle solidification, can be triggered in higher-mass rocky planets under similar initial conditions (see Section 3.4).

While Zalmoxis computed the planet's initial interior structure, the subsequent thermal and compositional evolution was handled by the Aragog module. The initial temperature profile was prescribed as a linear gradient, ranging from a surface temperature of 3300 K to a basal temperature of

5077 K at the core-mantle boundary (CMB). Atmospheric escape was disabled for this simulation, isolating the effects of interior evolution. This setup resulted in an initially fully molten mantle, with the rheological front (RF) located just beneath the CMB. During the evolution, Aragog made use of the liquidus melting curves from Monteux et al. [2016]. The corresponding solidus curve was set in Aragog as a constant 600 K offset below the liquidus one from Monteux et al. [2016]. This offset choice was an approximation established to prevent unphysical crossovers between the two curves at high pressures above 400 GPa and provides a consistent approximation in a regime where experimental constraints are sparse and melting curves are typically extrapolated. This pair of melting curves was used to guide the modeling of melt generation and solidification throughout the mantle in the fiducial simulation.

Outgassing processes at the surface-interior interface were modeled using the CALLIOPE module. The atmosphere/interior boundary oxidation state was set to $\log_{10}(\Delta\text{IW}) = +2$, reflecting an oxidizing environment that promotes the release of volatiles like H_2O and CO_2 during partial melting. The thermal forcing from the host star was provided by the MORS module, with a stellar mass of $1M_\odot$ and an initial age of 300 Myr. Additionally, atmospheric evolution was simulated using the JANUS module in prescribed-convective mode, with no atmospheric chemistry (neither equilibrium nor disequilibrium) included in this run to isolate thermal and dynamical effects.

The results of the PROTEUS simulation under the setup described above are presented in Sections 3.3.2 and 3.3.3 below (Lichtenberg et al. [2021], Johnstone et al. [2021], Graham et al. [2021], Nicholls et al. [2024]). Figures 3.6-3.8 collectively illustrate the time-dependent thermal, compositional, and dynamical evolution of the planet's mantle during the magma ocean solidification phase. Together, these figures provide a comprehensive picture of how an initially molten mantle cools, crystallizes, and transitions toward a more rigid, less convective interior, while simultaneously influencing the planet's surface environment.

3.3.2 Thermal and dynamic evolution of the planet's interior

Figure 3.6 illustrates the thermal and physical evolution of the mantle over time for the fiducial case. The thermal state at $t = 0$ (not shown in Figure 3.6) corresponds to the initial condition of the model, where the mantle is fully molten: temperatures lie entirely above the liquidus, resulting in a melt fraction of $\phi = 100\%$ from the surface to the core–mantle boundary (CMB). The snapshot at $t = 1$ year, shown in Figure 3.6, captures the state after the first timestep of the simulation. At this stage, the planet has begun to cool slightly, and although the mantle remains predominantly molten, temperatures in the innermost layers have started to drop below the liquidus, leading to a modest decrease in melt fraction near the CMB. Under these conditions, the entire interior is characterized by low viscosity, high temperature, and vigorous convective activity. This initial state serves as the starting point for the mantle's thermal evolution, which is captured across ten subsequent snapshots that reveal the progressive cooling and crystallization.

At early times ($\sim 10^3$ years) in the planet's evolution, the mantle is fully molten down to $\sim$ 90 GPa and transitions to a mushy state at greater depths. This is shown by the light pink curve in panel (b) of Figure 3.6, where the melt fraction is 100% up to $\sim$ 90 GPa and decreases to intermediate values in the mushy region at higher pressures. Correspondingly, panel (a) of Figure 3.6 shows the temperature profile, which reflects this transition with a temperature gradient that remains above the liquidus up to 90 GPa (fully molten) and gradually decreases into the mushy region at greater depths. Notably, the temperature decrease in the bottom mantle over the duration of the simulation is less pronounced, with a drop of approximately 600 K, compared to the upper mantle, which cools by around 2300 K. As the mantle cools, solidification proceeds from the bottom up, with the mushy region moving upward as the melt fraction gradually decreases and the pressure-temperature gradient flattens. This outward-moving crystallization front marks the transition of mantle regions from fully molten to mushy, and eventually to fully solid states over time.

Initially, viscosity in panel (c) of Figure 3.6 is extremely low throughout the whole mantle due to the high melt fraction, allowing for vigorous convection. However, as solidification progresses, viscosity increases by several orders of magnitude, creating a pronounced rheological contrast between the still partially molten upper mantle and the mushier lower mantle, as illustrated by the curves at $t = 10^3$, $t = 2.1 \times 10^3$, and $t = 4.4 \times 10^3$ years. Over time, this contrast becomes less steep at $t = 9.2 \times 10^3$, $t = 1.9 \times 10^4$, and $t = 4.1 \times 10^4$ years, as the upper mantle continues to solidify. Eventually, when the mantle is nearly fully solidified, viscosity becomes approximately constant throughout the interior. This state is reached by the final snapshot at $t = 7.8 \times 10^5$ years, which corresponds to the termination criteria of the simulation, triggered when the global melt fraction falls below 0.01, as described in Section 1.9.

Correspondingly, the convective heat flux shown in panel (d) of Figure 3.6 is initially high, driven

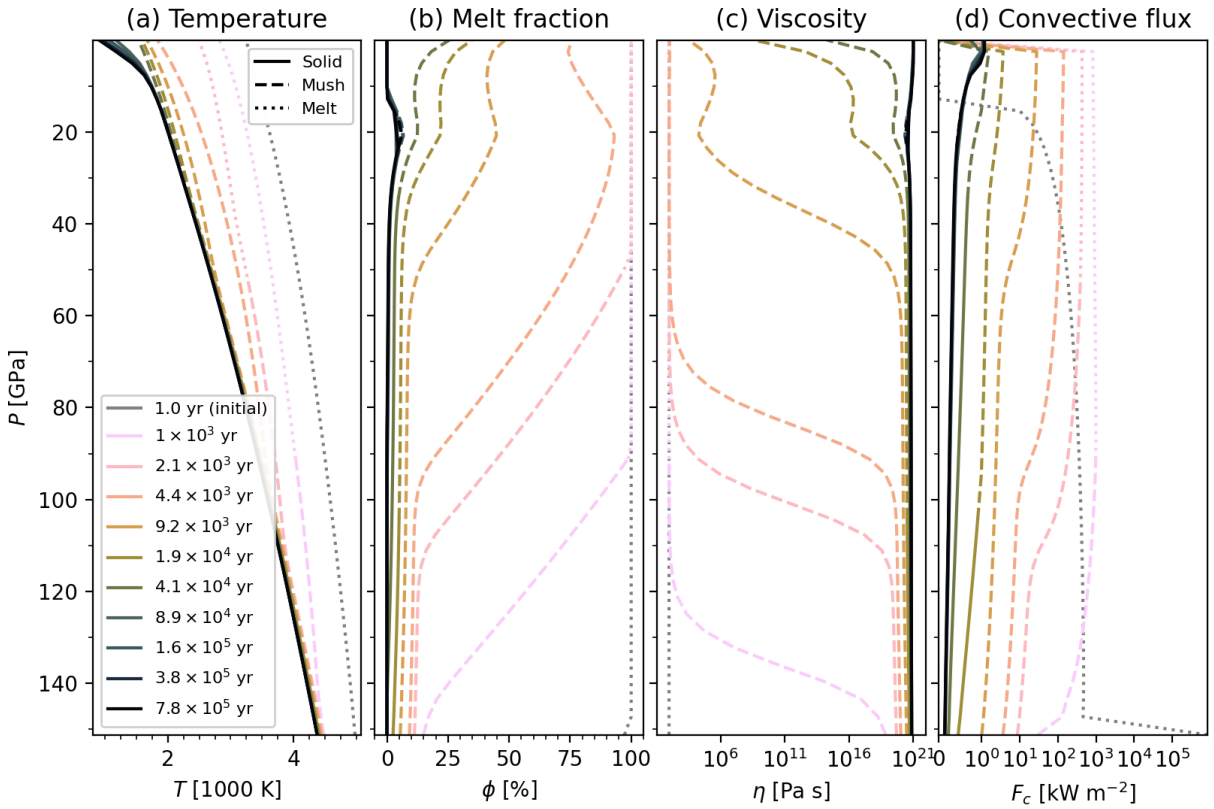

Figure 3.6: Pressure-dependent profiles of interior mantle properties at 11 selected time snapshots during the thermal evolution of the fiducial case. The snapshot at 1.0 year is included for reference to show the approximate initial thermal state. The remaining 10 snapshots are logarithmically spaced between 10^3 years and the end of the simulation time ($\sim 7.8 \times 10^5$ years). The different linestyles correspond to solid, mushy, and fully molten regions. **Panel (a)** Temperature T, showing cooling and crystallization over time. **Panel (b)** Melt fraction ϕ, showing how the initially molten mantle crystallizes from the top down. **Panel (c)** Dynamic viscosity η, spanning several orders of magnitude as the mantle solidifies. **Panel (d)** Convective flux F_c, indicating strong early heat transport followed by a decline as viscosity increases. **Note**: Pressure increases with depth, so the top of each panel corresponds to the surface, and the bottom represents the deep mantle near the core-mantle boundary (CMB).

by large temperature gradients and low viscosity, which facilitates efficient thermal transport. Over time, as the mantle cools and the melt fraction declines, the convective flux decreases significantly, especially in the deeper mantle, indicating a transition toward less efficient or potentially stagnant convection regimes.

Figure 3.7 complements the interior snapshots of Figure 3.6 by presenting the time evolution of the mantle's interior structure in pressure space, with four colormesh panels showing temperature, melt fraction, viscosity, and convective heat flux as functions of both pressure and time.

Panel (a) of Figure 3.7 shows temperature increasing linearly with pressure, with isotherms that remain relatively stable over time. This indicates a mantle that cools gradually while maintaining a stable temperature gradient, reflecting a steady loss of thermal energy from the interior.

Panel (b) of Figure 3.7 shows the melt fraction evolution. Early in the simulation, the upper mantle exhibits complete melting, as indicated by the white region extending down to about 150 GPa. With progressing time, a clear crystallization front moves upward, marking the transition from fully molten to partially molten (mushy) and finally to solid states. Notably, while the deepest mantle maintains a near-zero melt fraction for an extended period, intermediate-pressure regions between approximately 10 GPa and 40 GPa remain nearly fully molten until the end of the simulation.

Viscosity evolution is presented in panel (c) of Figure 3.7. At the beginning, viscosity is uniformly low throughout the mantle, reflecting the dominant influence of melt and high temperatures facilitating vigorous convection. As solidification advances, viscosity increases by many orders of magnitude, especially near the bottom of the mantle where crystallization is fastest. This leads to pronounced rheological layering, with low-viscosity partially molten upper layers overlying a high-viscosity, increasingly solid lower mantle. The transition from

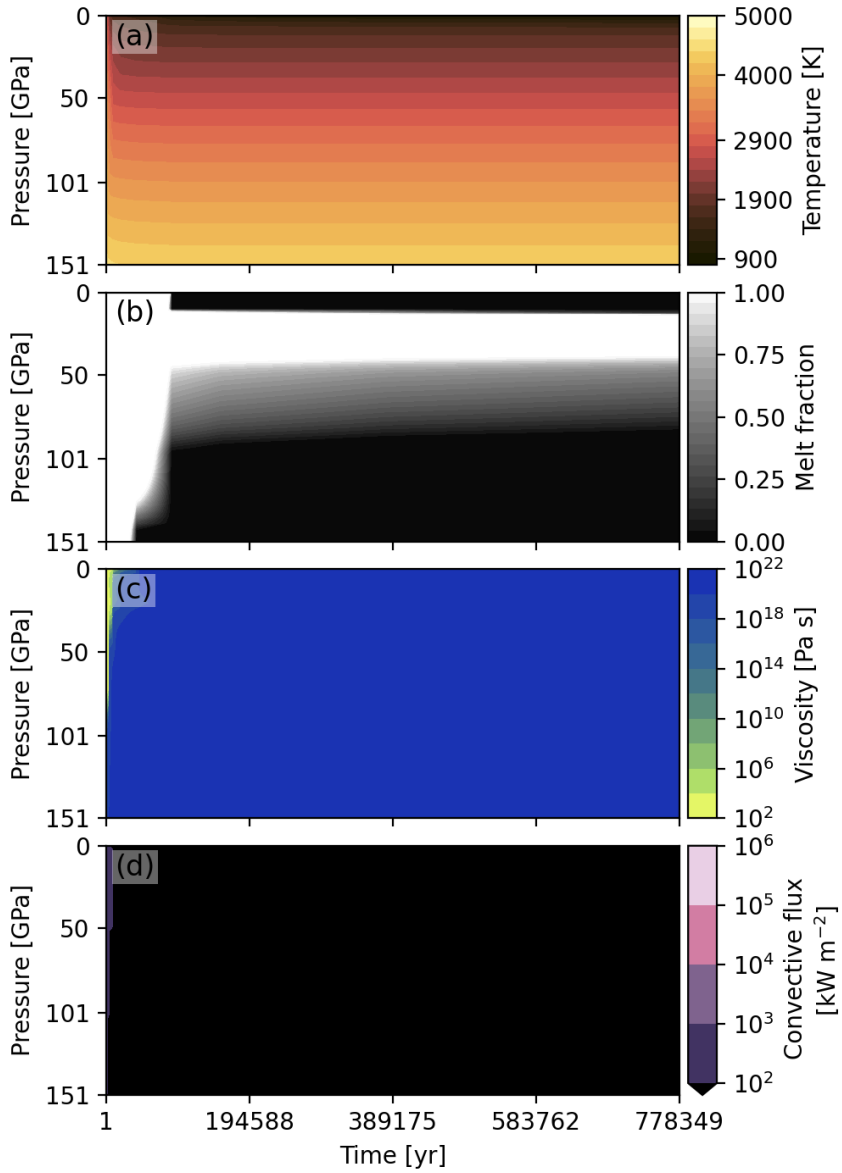

Figure 3.7: Time evolution of the planet's interior structure in pressure space. From top to bottom, the panels show temperature T, melt fraction ϕ, viscosity η, and convective heat flux F_c as a function of pressure and time. Each colormesh represents the radial profile of the corresponding quantity. **Note**: All panels share the same x-axis. Pressure increases with depth, so the top of each panel corresponds to the surface, and the bottom represents the deep mantle near the core-mantle boundary (CMB).

low to high viscosity is delayed in the upper mantle compared to the deeper regions. Over time, this rheological contrast gradually diminishes as the entire mantle solidifies, resulting in a high and nearly uniform viscosity by the end of the simulation.

Panel (d) of Figure 3.7 depicts the convective heat flux through the mantle. The flux is initially very high near the surface due to the large temperature gradients and low viscosity that promote efficient convective heat transport. However, as viscosity rises and melt fraction declines, the convective flux decreases, indicating a transition toward less efficient convection or even stagnant lid behavior, particularly in the deeper mantle. This decrease happens faster in the bottom mantle than in the upper regions.

3.3.3 Coupled evolution of the planet's interior, surface, and atmosphere

Figure 3.8 shows the time evolution of the planet's thermal and volatile state, including heat flux components, surface volatile pressures, surface and interior temperatures, surface volatile mixing ratios, the evolution of the rheological front and global melt fraction in the mantle, and the fraction of each volatile species retained in the interior over time.

Panel (a) of Figure 3.8 illustrates the temporal

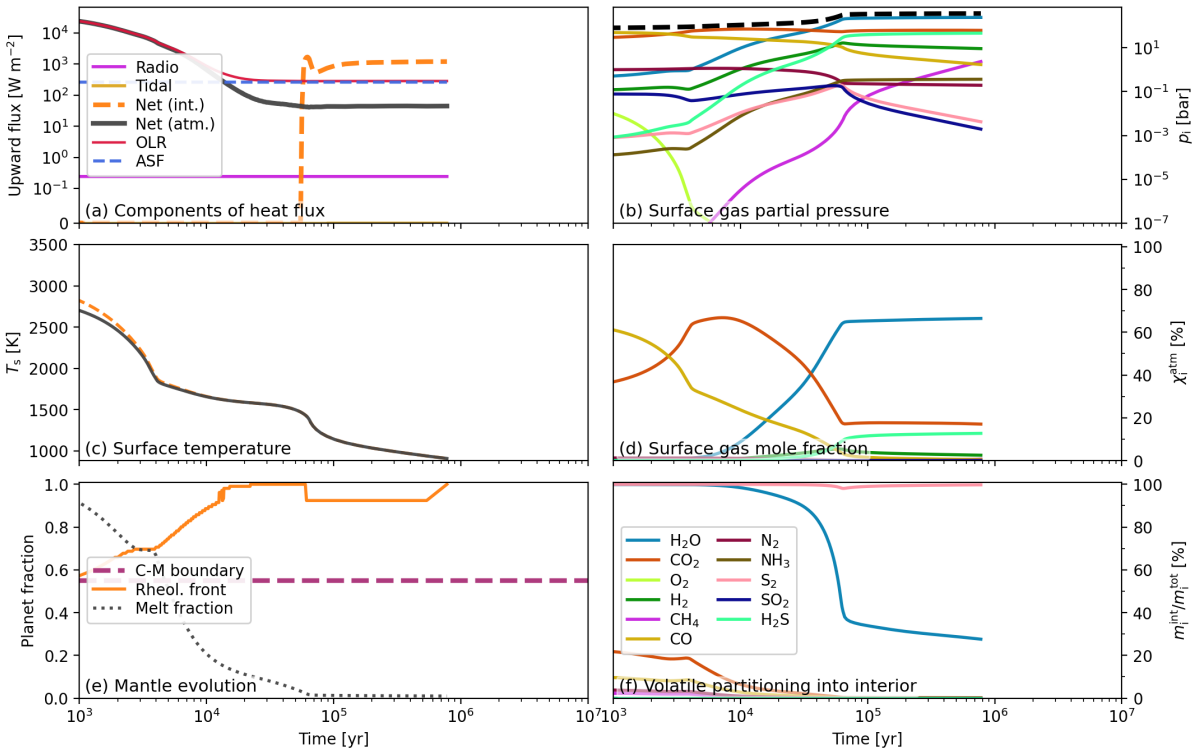

Figure 3.8: Time evolution of the planet's thermal and volatile state in the fiducial case with a linear initial temperature profile. **Panel (a)** Components of the upward heat flux. Solid lines show contributions from radiogenic heating (magenta), tidal heating (yellow), outgoing longwave radiation (red), and net atmospheric flux (gray). Dashed lines shows net internal flux (orange) and absorbed stellar flux at the surface (blue). **Panel (b)** Evolution of surface partial pressure for each volatile species (colored lines), with the dashed black line showing the total surface pressure. **Panel (c)** Surface temperature evolution. The solid line shows the atmospheric temperature at the surface, while the dashed orange line shows the temperature of the interior at the surface of the planet as it cools. **Panel (d)** Volume mixing ratio (VMR) of each volatile species at the surface. **Panel (e)** Evolution of the planet's mantle. The solid line marks the depth of the rheological front, normalized to the planet's radius (i.e., 1 corresponds to the surface, 0 to the center). The dashed horizontal line marks the location of the core-mantle boundary ($\sim 0.55 R_p$). The dotted line indicates the global melt fraction of the mantle, normalized to its maximum value of 1. Both the rheological front position and the global melt fraction are normalized to the planet's radius, but they represent distinct quantities: the front position refers to a physical depth, whereas the global melt fraction is a thermodynamic quantity derived from the local temperature relative to the solidus and liquidus, as defined in Eq. 2.12. **Panel (f)** Evolution of the interior volatile retention. Solid lines show the percentage of each volatile species remaining in the interior relative to its initial inventory, indicating the efficiency and timing of volatile outgassing over time. **Note**: All panels share the same x-axis. Pressure increases with depth, so the top of each panel corresponds to the surface, and the bottom represents the deep mantle near the core-mantle boundary (CMB).

evolution of various upward heat flux components from the planet's interior and atmosphere. The net atmospheric heat flux (gray) begins at a peak value of approximately $4.8 \times 10^4\,\mathrm{W\,m^{-2}}$ and steadily declines over time as the mantle cools and solidifies. Initially, the outgoing longwave radiation (OLR) flux (red) closely tracks the net atmospheric heat flux, indicating efficient thermal emission through the atmosphere during the early, high-temperature stages. As cooling progresses, the OLR flux asymptotically approaches the absorbed stellar flux (blue), stabilizing around $\sim 2.8 \times 10^2\,\mathrm{W\,m^{-2}}$, while the net atmospheric flux continues to decrease, reaching a value near $\sim 4.4 \times 10^1\,\mathrm{W\,m^{-2}}$ by the end of the simulation. Radiogenic and tidal heating contributions remain negligible throughout, with values below $1\,\mathrm{W\,m^{-2}}$. A notable feature occurs between approximately 5×10^4 and 6×10^4 years, where the net internal flux (orange) undergoes a sudden increase from near-zero values to a peak of roughly $\sim 1.7 \times 10^3\,\mathrm{W\,m^{-2}}$. Following this spike, the internal flux declines slightly and plateaus around $\sim 1.1 \times 10^3\,\mathrm{W\,m^{-2}}$.

Panel (c) of Figure 3.8 shows the temperature evolution of the atmosphere-interior boundary as the planet cools over time. At early times ($\sim 10^3$ years, both the atmosphere and surface are extremely hot with the magma ocean being partially

molten (see Figure 3.6) and the surface radiating energy away. During the subsequent cooling phase, the surface temperature rapidly decreases, as the latent heat is released during solidification. The dashed orange line (the interior temperature at the surface) evolves closer and closer to the solid line (the atmosphere temperature at the surface), indicating efficient energy transfer between surface and atmosphere down to $\sim 950\,\mathrm{K}$ after $\sim 4 \times 10^5$ years. Eventually, thermal equilibrium is reached between the atmosphere and the planetary interior at the surface, stabilizing at $\sim 910\,\mathrm{K}$. The observed inflection in the surface temperature curve around $\sim 4.4 \times 10^3$ years reflects transitions in the mantle's convective regime. As the melt fraction drops below $\sim 60\%$, the planet enters the rheological transition, causing a steep decline in convective efficiency (Lichtenberg and Miguel [2025]). This results in a shift from rapid to slower cooling, ultimately leading to the dominance of conductive heat transport as the mantle fully solidifies.

Panel (e) of Figure 3.8 shows the rheological front just above the mantle after $\sim 10^3$ years of evolution, indicating partial melting. This is consistent with the expected thermal evolution, as crystallisation first occured in the first year of the simulation, with ϕ dropping below 1 between $t = 0$ and $t = 1$ year (not visible in this panel but confirmed in the numerical output). In the following years, the RF gradually progressed upward as the planet cooled. Minor instabilities between $\sim 1 \times 10^4$ and $\sim 2 \times 10^4$ years caused by the algorithm of computing the RF's depth were observed near the planet's surface. The rheological front first reached the surface at $\sim 2.2 \times 10^4$ years (when the melt fraction of the planet is $\sim 10\%$). The front remained at the surface for an additional $\sim 3.7 \times 10^4$ years before going downwards to $\sim 0.92 R_p$. After this small recession, the front remained at $\sim 0.92 R_p$ for another $\sim 4.7 \times 10^5$ years before going upwards again to the surface in the next $\sim 2.4 \times 10^5$ years. Full crystallization of the mantle (defined as the point at which the global melt fraction decreases below 0.01) was achieved $\sim 7.8 \times 10^5$ years from the onset of crystallization.

Panels (b), (d), and (f) of Figure 3.8 collectively track the volatile behavior across the atmosphere and interior. Panel (b) depicts the temporal evolution of surface partial pressures for key volatile species. Early outgassing leads to substantial increases in the partial pressures of H_2O, H_2, H_2S, NH_3, and S_2. These pressures subsequently stabilize or decline as volatiles either condense, dissolve back into the melt, or partition into the planetary interior. The total atmospheric pressure correspondingly rises, with CO_2 and CO dominating the atmosphere after approximately 10^3 to 10^4 years. Approaching 10^5 years, H_2O becomes the prevailing atmospheric species and remains dominant until the mantle fully solidifies. Atmospheric O_2 is transient, rapidly decreasing to about 10^{-7} bar within 10^4 years of the simulation onset. Panel (d) depicts the mole fractions of surface volatiles. Notably, the mole fraction of CO_2 peaks early, whereas H_2O increases gradually, surpassing other species after roughly 3×10^4 years to become the dominant atmospheric constituent. Panel (f) further emphasizes the transition of H_2O from a major component of the interior reservoir to a dominant atmospheric constituent after approximately 10^4 years, although a substantial fraction of less than 30% remains trapped within the mantle by the end of the simulation.

3.4 Evolution of 1 to 7 $M_\oplus$ Earth-like rocky exoplanets

3.4.1 Setup and initial conditions

To further investigate the behavior of rocky exoplanets during their crystallization period across a broader planetary mass range, a set of simulations was performed for planets with masses spanning 1 to 7 $M_\oplus$. This range was sampled using linear mass increments as a first-order approach to systematically explore thermal and volatile evolution across typical super-Earth sizes. While this simplification does not account for the non-linear scaling of internal properties with mass, such as the fact that the transition from 1 to 2 $M_\oplus$ may yield more dramatic changes in interior structure and dynamics than from 6 to 7 $M_\oplus$, it provides a controlled baseline for identifying broad trends.

Each simulation was initialized with a fully molten mantle and used the same underlying physical and numerical setup as described in Section 3.3.1, with the planetary mass, surface temperature, and basal temperature at the core-mantle boundary varied between runs (see Table 3.1). Adopting a fully molten mantle as a common initial condition, corresponding to a global melt fraction of $\Phi_{\mathrm{global}} = 100\%$, ensures that differences in solidification behavior arise primarily from intrinsic planetary properties, such as mass-dependent pressure and heat retention, rather than from variations in initial melt distribution. This common thermal baseline provides a consistent reference point for analyzing the evolution of the rheological front and the associated thermal dynamics across planetary masses.

However, achieving a fully molten mantle requires careful setup of the initial thermal conditions, particularly for higher-mass planets, whose deep interiors are more resistant to complete melting due to stronger pressure effects and enhanced heat retention. As planetary mass increases, progressively higher basal and surface temperatures are needed to exceed the liquidus throughout the

Table 3.1: Parameter variations across simulation runs. The columns show: planetary mass, surface temperature, and basal temperature at the core-mantle boundary. All other parameters follow the fiducial case setup in Section 3.3.1.

Mass [$M_\oplus$]	Surface T [K]	Basal T [K]
1	3300	5077
2	3300	6838
3	3900	7946
4	3990	9280
5	3990	10515
6	3990	11734
7	4000	12673

mantle. To prevent premature termination of simulations under these extreme thermal conditions, volatile escape was disabled in all runs.

One important factor in achieving the intended thermal state was the choice of the initial temperature profile. While an adiabatic profile would be more physically appropriate for a vigorously convecting mantle, the current implementation of Aragog only supports this option reliably for planets with masses $\lesssim 2M_\oplus$, due to a dimensional mismatch error at higher masses. A comparative test for the fiducial case presented in Section 3.3 also showed that linear profiles result in slightly earlier surface crystallization and faster mantle solidification compared to adiabatic ones, though both profiles captured the essential aspects of the thermal evolution. For consistency and numerical stability across the full mass range, a linear temperature profile was used in all simulations.

A second key consideration in achieving the intended thermal state was ensuring that solidification began within a consistent timescale across the planetary mass range. The objective was to establish initial thermal conditions that not only yielded a fully molten mantle at the start of the simulation ($t = 0$), but also triggered the onset of solidification, manifested as the formation and upward progression of the rheological front, within the first year. To achieve this under the time-stepping conditions described in Section 3.3.1, the surface and basal temperatures were systematically varied, while all other parameters were held fixed. This approach aimed to constrain the timing of solidification onset, allowing direct comparison of crystallization dynamics as a function of planetary mass. As a result, it was observed that temperatures set below this threshold resulted in partial melting and an initial state inconsistent with the intended fully molten mantle. Conversely, setting the initial temperatures excessively high, particularly for more massive planets, resulted in a fully molten mantle with such an elevated thermal state that the early formation and upward propagation of the rheological front were substantially delayed. Although solidification inevitably occurred as the planet cooled over longer timescales, the rheological front remained stalled deep in the mantle during the early stages of the simulation. This delay in crystallization onset was inconsistent with the intended thermal evolution, which assumed that solidification would begin within the first year. The challenge was therefore to strike a balance: the initial thermal state needed to be sufficiently high to ensure full mantle melting, yet low enough to permit early formation and upward propagation of the rheological front within the first year of simulation.

For all simulations, the PROTEUS model applied a set of predefined termination criteria as described in Section 1.9. Lower-mass planets (1 and 2 $M_\oplus$) terminated upon mantle solidification, with the global melt fraction dropping below the critical threshold of 1%. Intermediate-mass planets (3 to 5 $M_\oplus$) reached radiative equilibrium before full solidification and were thus stopped at that point. In contrast, higher-mass planets (6 and 7 $M_\oplus$) remained partially molten and did not meet either condition within the simulation time window, so they were terminated upon reaching the maximum simulation time of 4.567 billion years.

The results of the PROTEUS simulation under the setup described above are presented in Sections 3.4.2 and 3.4.3 below (Lichtenberg et al. [2021], Johnstone et al. [2021], Graham et al. [2021], Nicholls et al. [2024]). Figures 3.9-3.10 illustrate how initial thermal conditions and planetary mass influence the simulation duration, the degree of mantle solidification at the end of the runs under the specified termination criteria, and the final surface conditions. Figures 3.11, 3.12, 3.13, and 3.14 collectively show the time evolution of global melt fraction, total surface pressure, surface magma temperature, and surface H_2O pressure, respectively, for planets of different masses. Together, these figures provide a comprehensive picture of the coupled interior-atmosphere evolution of rocky planets during the early cooling and outgassing phases from initially molten conditions.

3.4.2 Dependence of crystallization and surface conditions on planetary mass

The results of the simulations for fully molten planets with 1 to 7 $M_\oplus$ masses (shown in Figures 3.9 and 3.10) reveal the dependence of both interior crystallization and surface conditions on planetary mass. Corresponding plots illustrating the mantle's thermal and volatile evolution for these simulations (similar to Figures 3.6-3.8) can be found in Appendix B.

Figure 3.9 shows that higher initial basal temperatures in massive planets generally result in elevated final melt fractions. More specifically, for

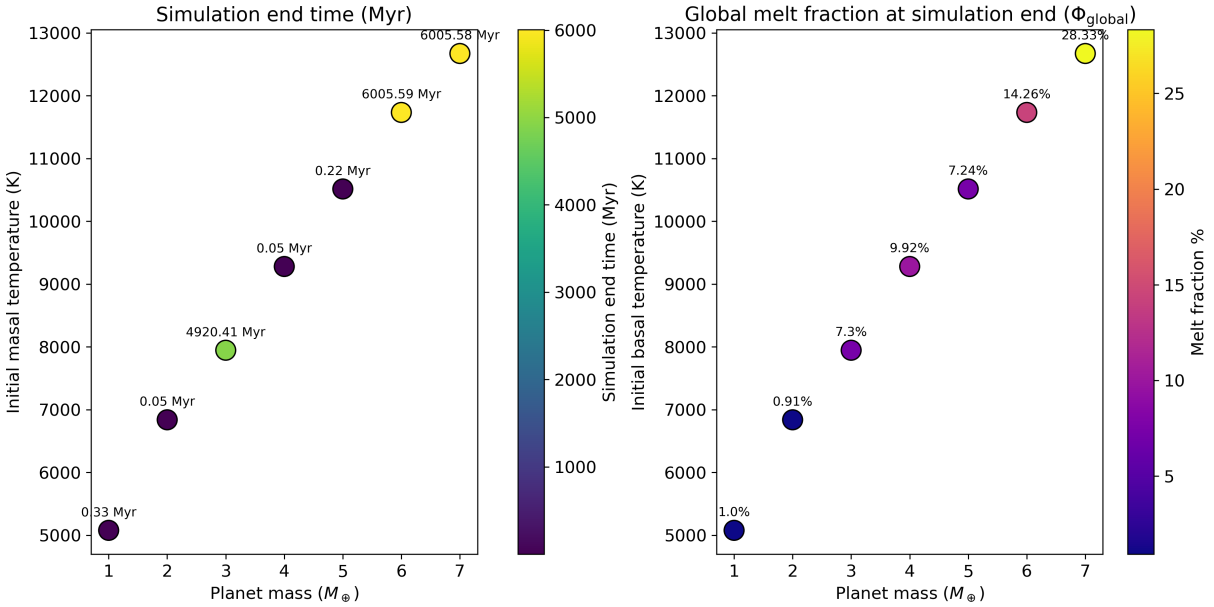

Figure 3.9: Simulation end results for varying planetary masses and initial basal temperatures. Left: Simulation end time for each model run. Right: Final global melt fraction (Φ_{global}) at the end of each simulation.

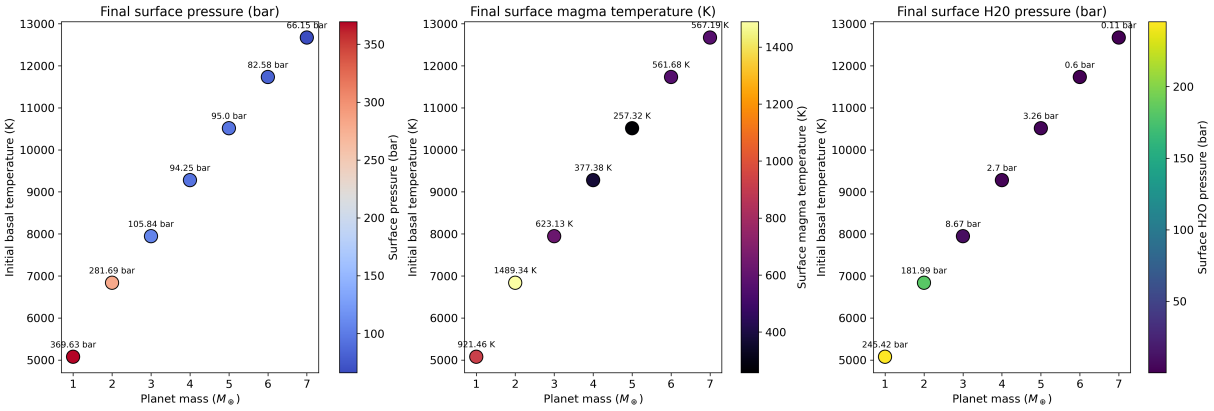

Figure 3.10: Final surface conditions as a function of planet mass and initial basal temperature. Each panel shows the outcome of simulations initialized with fully molten mantles, varying by planetary mass and basal temperature. Left: Final total surface total pressure, capturing the buildup of atmospheric volatiles. Center: Final surface magma temperature, reflecting the final thermal state of the surface. Right: Final surface H_2O pressure, indicating the extent of outgassed H_2O.

planets with 1 to 2 $M_\oplus$, complete solidification is achieved within the simulation time, with final global melt fractions falling below 1%, indicating a fully crystallized mantle. In contrast, more massive planets ($3-5M_\oplus$) exhibit significantly slower cooling rates, leading to melt fractions exceeding 7% after billions of years. These planets reach a stable energy balance and partially crystallized interior before achieving full solidification. For the most massive cases (6 and 7 $M_\oplus$), neither solidification nor radiative equilibrium is reached within the maximum simulation time of 4.567×10^9 years. These planets retain substantial residual melt, with final global melt fractions of approximately 14% and 28%, respectively.

In parallel, Figure 3.10 illustrates how surface conditions also vary with planetary mass. Final total surface pressures (left panel) generally decrease with increasing mass. A similar trend is observed in the final surface H_2O pressure (right panel), which drops sharply from over 200 bar for $1M_\oplus$ to less than 1 bar for $7M_\oplus$. However, when comparing final magma temperatures in the middle panel of Figure 3.10, it is important to consider the simulation termination conditions. Among the lower-mass planets (1 and 2 $M_\oplus$), which terminated upon mantle solidification (global melt fraction $< 1\%$), the 2 $M_\oplus$ planet exhibits a notably higher final temperature compared to the 1 $M_\oplus$ planet. For the intermediate-mass planets (3 to 5 $M_\oplus$) that terminated after reaching radiative equilibrium, the final magma temperatures generally

decrease with increasing planetary mass. Finally, the higher-mass planets (6 and 7 $M_\oplus$) retain intermediate final magma temperatures between 560 K and 570 K, lower than the 3 $M_\oplus$ case (≈620 K) but higher than the 4 $M_\oplus$ (≈380 K) and 5 $M_\oplus$ (≈260 K) planets. This pattern for higher-mass planets arises because they have not yet reached radiative equilibrium or complete solidification within the simulation window and will be discussed further in Section 4.4.

3.4.3 Time evolution of interior and atmospheric properties

To complement the summary results shown in Figures 3.9-3.10, Figures 3.11 and 3.12 illustrate the full time evolution of the global melt fraction and surface magma temperature, respectively, for all planetary masses considered. Meanwhile, Figures 3.13 and 3.14 present the corresponding time profiles of total surface pressure and surface H_2O pressure, respectively, highlighting the early atmospheric evolution and volatile outgassing processes across the different planetary masses.

Among all simulated cases, the low-mass planets ($1-2M_\oplus$) exhibit the earliest progression toward solidification. Their global melt fraction profiles (see Figure 3.11) are the smoothest across all masses, with the 2 $M_\oplus$ case lying below the 1 $M_\oplus$ profile throughout the simulation. This indicates a more rapid and sustained crystallization in the 2 $M_\oplus$ planet, likely explaining why it fully solidifies earlier than its lower-mass counterpart. Correspondingly, these planets are the first to reach a stable plateau in surface magma temperature, doing so within the first $\sim 10^4 - 2 \times 10^4$ years (see Figure 3.12). These low-mass planets also maintain higher total surface pressures and surface H_2O pressures throughout the simulation compared to their more massive counterparts in Figures 3.13 and 3.14.

In contrast to the low-mass planets, the intermediate-mass cases ($3 - 5M_\oplus$) exhibit more prolonged and irregular cooling behavior. Their global melt fraction profiles reflect this irregularity, with noticeable fluctuations both before and after $\sim 10^4$ years (see Figure 3.11). The 3 $M_\oplus$ planet displays the most aggressive drop in melt fraction, while the 5 $M_\oplus$ case initially lags behind the 4 $M_\oplus$ planet within the first $\sim 10^4$ years of the simulation. However, a crossover occurs shortly after the $\sim 10^4$ years timestep, and by the end of the simulation, the 5 $M_\oplus$ planet exhibits a slightly lower final melt fraction than the 4 $M_\oplus$ case. The surface magma temperature profiles of these planets take longer to stabilize and show non-monotonic evolution, as shown in Figure 3.12. Among them, the 3 $M_\oplus$ case is the least efficient at cooling, maintaining higher temperatures for longer durations. The 5 $M_\oplus$ temperature curve initially drops below that of the 4 $M_\oplus$ planet around $\sim 10^4$ years, suggesting more efficient early cooling. However, a crossover follows shortly after, where the 5 $M_\oplus$ curve rises above the 4 $M_\oplus$ profile and remains higher until $\sim 6.5 \times 10^4$ years. At that point, the 5 $M_\oplus$ planet continues cooling, ultimately reaching a lower final temperature than the 4 $M_\oplus$ planet, which by then has already achieved radiative equilibrium. Moreover, the total surface pressure and surface H_2O pressure scale inversely with mass in this group in Figures 3.13 and 3.14. The 3 $M_\oplus$ planet outgasses more effectively, maintaining consistently higher surface pressure profiles than the 4 $M_\oplus$ and 5 $M_\oplus$ planets across the simulation window. This trend is mirrored in the surface H_2O pressure profiles.

For the most massive planets ($6 - 7M_\oplus$), neither full solidification nor radiative surface equilibrium is reached within the simulation time frame. Their global melt fraction profiles (see Figure 3.11) remain higher than those of smaller planets beyond $\sim 10^5$ years, indicating that these planets retain substantial interior melt for extended periods. Despite their partially molten interiors, the surface magma temperatures of these planets (see Figure 3.12) eventually fall below those of less massive planets, pointing to relatively efficient surface cooling during the early evolutionary phase (within the first $\sim 3 \times 10^5$ years). Nevertheless, the 6 and 7 $M_\oplus$ planets do not cool below the 4 and 5 $M_\oplus$ cases by the end of the simulations, which were terminated upon reaching the maximum runtime. The total surface pressure and surface H_2O pressure scale inversely with mass within this group too, as evident in Figures 3.13 and 3.14. The 6 $M_\oplus$ planet outgasses more efficiently, resulting in consistently higher total surface pressure and surface H_2O pressure profiles than those of the 7 $M_\oplus$ planet throughout the simulation.

4 DISCUSSION

4.1 Standalone use of Zalmoxis: strengths and limitations

Despite increasing interest in exoplanet interior characterization, few open-source tools are available for detailed structural modeling. One notable exception is MAGRATHEA, a spherically symmetric interior structure code developed by Huang et al. [2022]. However, as MAGRATHEA is written in C++, it may be less accessible to researchers who primarily work in high-level scientific computing environments. In this context, Zalmoxis offers a Python-based, modular, and user-friendly alternative for constructing physically consistent planetary interiors. Its design supports a wide range of compositions and structural configurations, making it well-suited for both standalone applications and in-

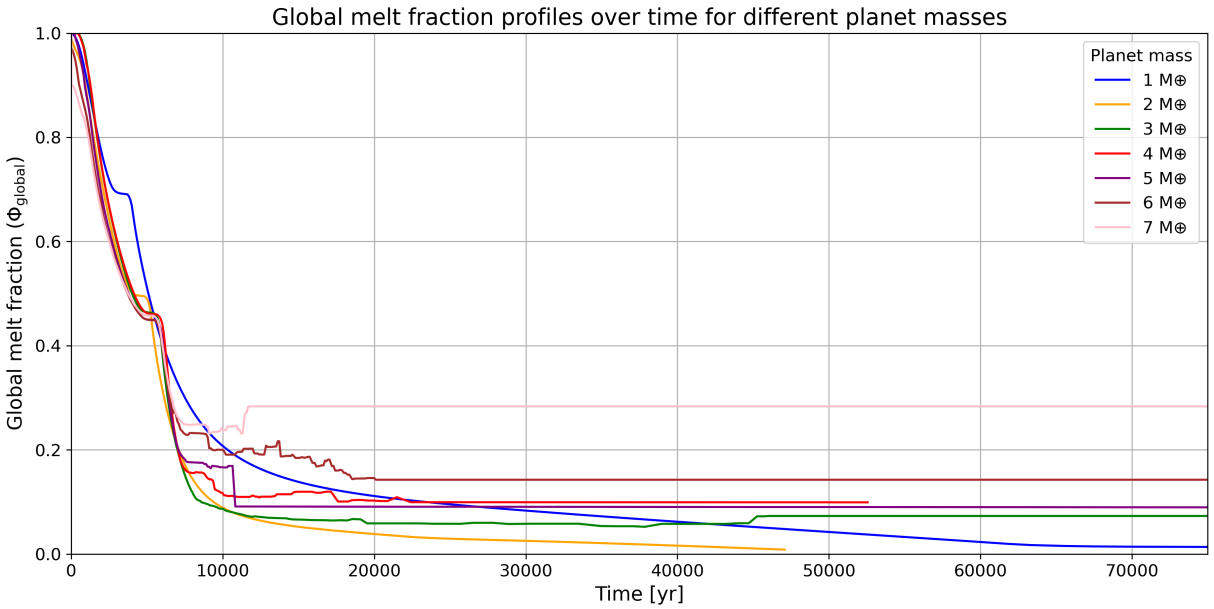

Figure 3.11: Global melt fraction evolution over time for planets ranging from 1 to 7 $M_{\oplus}$. The plot shows the time-dependent global melt fraction (Φ_{global}) from fully molten initial states to solidification. The time axis is clipped at 75000 years to focus on the period of active crystallization. Beyond this cutoff, the melt fraction profiles become horizontal, indicating that the planets have reached near-complete solidification or thermal equilibrium.

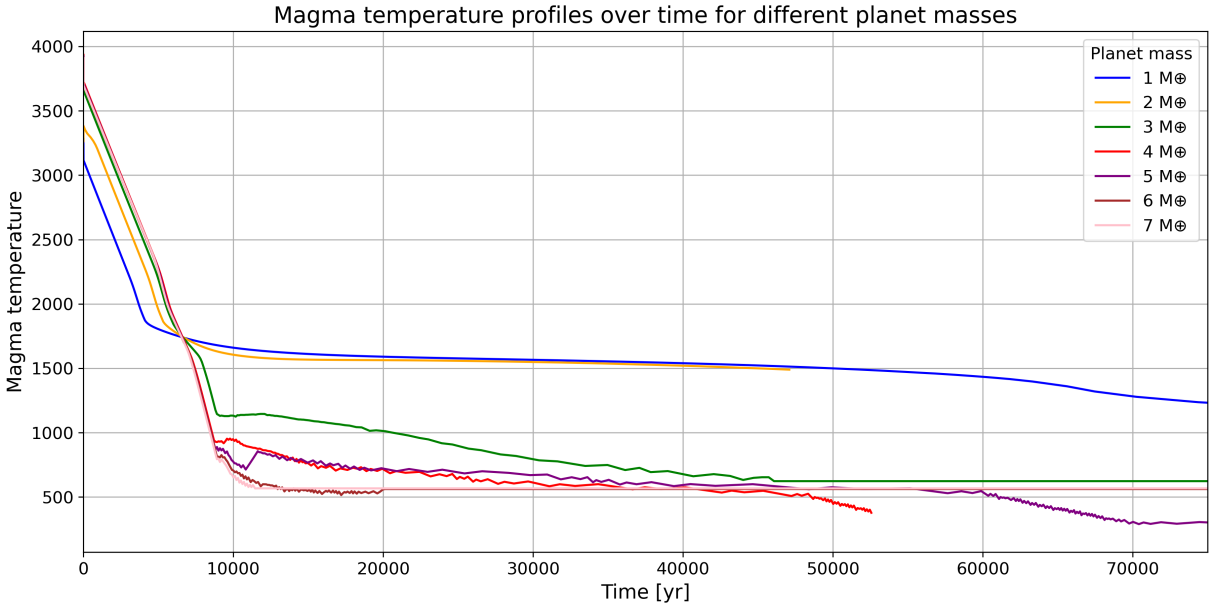

Figure 3.12: Surface magma temperature evolution over time for planets ranging from 1 to 7 $M_{\oplus}$, starting from fully molten initial conditions. The time axis is limited to 75000 years to focus on the early cooling phase. Beyond this cutoff, the temperature profiles become horizontal, indicating thermal stabilization at the surface.

tegration within broader simulation pipelines such as PROTEUS.

Zalmoxis, as a standalone tool, offers flexibility in modeling a wide range of differentiated planetary interior structures, from rocky super-Earths to water-rich worlds. By allowing compositional variations in the iron core, silicate mantle, and water ice layer, Zalmoxis enables users to construct physically consistent interior profiles across diverse planet types, including pure-component models (e.g., pure Fe, $MgSiO_3$, or H_2O) and layered configurations with or without a metallic core. While Zalmoxis is capable of modeling Earth-like and water-rich planets with adjustable mass fractions to reflect realistic differentiation scenarios, it cannot currently fully model sub-Neptunes, only their rocky or icy cores. In particular, Zalmoxis does not support the treatment of extended H_2/He-rich envelopes, limiting its applicability to planets with substantial gaseous atmospheres. Moreover, it does

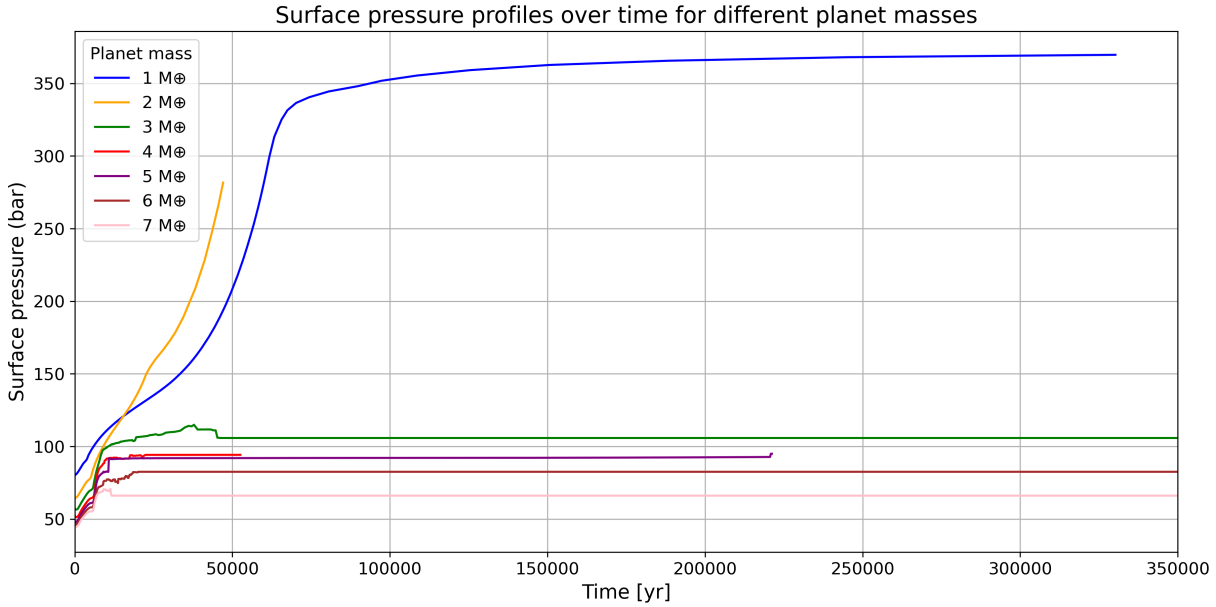

Figure 3.13: Total surface pressure evolution over time for planets ranging from 1 to 7 $M_{\oplus}$, starting from fully molten initial conditions. The time axis is limited to 350000 years to highlight early atmospheric evolution. Beyond this cutoff, the profiles become horizontal, indicating that outgassing has ceased and the total surface pressure has stabilized.

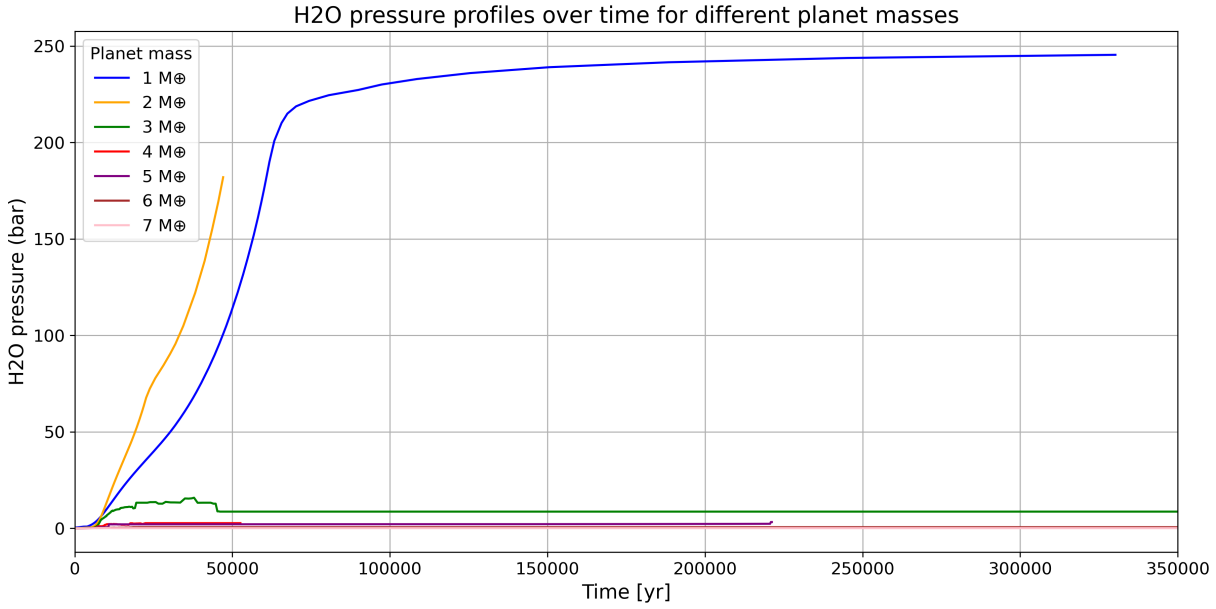

Figure 3.14: Evolution of surface H_2O pressure over time for planets ranging from 1 to 7 $M_{\oplus}$. The time axis is limited to 350000 years to emphasize the early stages of outgassing. Beyond this point, the profiles flatten, indicating that most of the H_2O has already been released to the surface.

not account for exotic atmospheric compositions such as silicate-rich atmospheres, which can occur on the hottest super-Earths due to vaporization of refractory materials (Duffy et al. [2015], Schaefer et al. [2012]).

In this work, "water-rich planets" are defined as those composed of an iron core, a silicate mantle, and an outer water ice layer. However, depending on pressure conditions, the water may exist in various solid phases (e.g., high-pressure ices), liquid, or even vapor form. While Zalmoxis currently treats only pure water ice layers, future versions could benefit from a phase-dependent water EOS to capture transitions relevant for deep exoplanetary interiors. Such refinements are important because the presence and phase of water have significant implications for planetary properties. Notably, water is widely recognized as a critical factor for habitability, influencing melting behavior, mantle rheology, and potentially the likelihood of plate tectonics,

all processes that fundamentally shape a planet's geodynamics and surface environment (Korenaga [2010], Duffy et al. [2015]). Therefore, accurately representing the diverse phases of water and their thermophysical effects is essential for realistic modeling of water-rich exoplanets and assessing their potential habitability.

A key avenue to enhance Zalmoxis's flexibility would be to increase its modularity by allowing users to select different phase diagrams and equations of state for each planetary layer, similar to the approach taken by MAGRATHEA. This would enable the modeling of diverse planetary interiors with customized mineralogical and thermodynamic assumptions, thereby accommodating new experimental or theoretical data as they become available. Such modular design would also facilitate comparative studies exploring the impact of different EOS formulations on interior structure predictions and improve the adaptability of Zalmoxis for a wide range of planetary types.

Another promising direction for extending Zalmoxis is to better account for the broad diversity of super-Earth interiors, including planetary types with no direct analogs in our Solar System. This presents a considerable challenge, as the lack of well-studied baseline compositions and structures limits our ability to constrain interior models reliably. For example, carbon-rich planets represent a potentially novel regime of planetary interiors, composition, and evolution that differs substantially from familiar silicate- and iron-dominated bodies. These planets may host interiors dominated by carbides or diamond phases, requiring new equations of state and mineralogical models distinct from the conventional oxide- and silicate-based frameworks (Duffy et al. [2015]).

Moreover, even for more familiar terrestrial super-Earth compositions, the mantle mineralogy may encompass a wider range of phases than currently modeled. Key mantle constituents such as MgO, FeO, CaO, Al_2O_3, and SiO_2 are under exploration under the extreme pressures and temperatures characteristic of super-Earth interiors (Duffy et al. [2015]). Incorporating such compositional and mineralogical diversity into Zalmoxis would improve its applicability to the rapidly expanding population of exoplanets and help capture the true range of planetary structure and evolution beyond the Solar System.

In addition, the current version of Zalmoxis assumes sharp compositional boundaries and fully differentiated interiors, which may not reflect the true complexity of planetary structures. For instance, geochemical and geophysical evidence from Earth and other solar system bodies suggests that iron is not strictly confined to the core, but also exists in appreciable quantities in the mantle, either as metallic iron or oxidized forms such as FeO in silicate minerals (Duffy et al. [2015]). This distribution affects the planet's density profile and internal structure. Extending Zalmoxis to model such mixed-phase or partially differentiated compositions could provide a more accurate representation of planetary interiors, especially for exoplanets whose bulk properties may diverge significantly from solar system analogs. Existing Python-based tools like ExoPlex (Unterborn et al. [2018], Unterborn and Panero [2019], Schulze et al. [2021]) have begun addressing this complexity by incorporating mantle mineralogies based on Mg, Fe, Si, and O compositions for planets in the 0.1 to $\sim 2M_\oplus$ mass range, offering a useful benchmark for expanding Zalmoxis in a similar direction. Moreover, ExoPlex allows users to specify a target radius and solve for the corresponding planetary mass (Unterborn et al. [2018]), a feature not yet available in Zalmoxis. Adding this capability would significantly enhance its versatility for exoplanet interior modeling, particularly in cases where the planetary radius is well constrained by observations, but the mass remains uncertain.

Beyond composition, thermal structure modeling is another critical area for future development. At present, Zalmoxis does not calculate any temperature distribution within the planet. Incorporating a self-consistent thermal profile would significantly enhance the model's physical realism. This is particularly important during early planetary stages, when latent heat release and vigorous convection strongly affect the internal energy balance. As noted by Bower et al. [2018], the temperature structure inside a solidifying magma ocean deviates from a simple adiabatic gradient due to latent heat transport driven by convection. Thus, even an approximate treatment of these effects would better couple thermal and structural calculations, making Zalmoxis more robust for diverse planetary interior applications.

Finally, computational efficiency is an important consideration for interior structure solvers, particularly in the context of large parameter studies or integration within forward modeling pipelines. Zalmoxis computes the internal structure of a $1M_\oplus$ Earth-like planet in approximately 5 s. This is slower than MAGRATHEA, which achieves convergence in an average of 0.69 seconds, and also slower than ExoPlex, which takes about 1.46 seconds (Huang et al. [2022]). Thus, improving the runtime performance of Zalmoxis could significantly enhance its utility, particularly for large-scale or time-sensitive applications.

The results presented in ternary diagrams in Section 3.2 illustrate that model runtimes vary as a function of interior structure and planetary mass, consistent with findings for MAGRATHEA

by Huang et al. [2022]. Generally, computational time increases with planetary mass due to the increased complexity of higher-mass interiors. Iron-rich compositions consistently require longer runtimes, likely due to the stiffer equations of state associated with iron cores, while runtime exhibits only a weak dependence on mantle fraction, a trend which was also observed by Huang et al. [2022]. The capacity to simulate hundreds of compositions cases within seconds to minutes makes the model well suited for applications requiring large-scale parameter sweeps, including Monte Carlo methods and Bayesian inference frameworks. Future work could investigate additional dependencies among interior parameters to further refine model performance and accuracy.

4.2 Implications of Zalmoxis usage within PROTEUS

The integration of Zalmoxis into the PROTEUS pipeline significantly enhances its physical realism in modeling planetary structure and composition. Prior to this implementation, Aragog utilized the AWEOS to generate internal density and pressure profiles (see Section 2.6), which imposed significant limitations, particularly for simulations of high-mass planets. By replacing AWEOS with Zalmoxis-generated profiles, PROTEUS now implements more accurate structural inputs for thermal evolution calculations, including depth-dependent variations in pressure, density, gravity, and composition.

However, the current implementation of Zalmoxis in PROTEUS assumes a static EOS regime when computing the planet's state at the start of its evolution, without explicitly accounting for its initial thermal phase. While Aragog subsequently handles phase-dependent EOS behavior during the planet's interior evolution, the initialization in Zalmoxis could be made more consistent by dynamically assigning the appropriate EOS based on the planet's starting thermal state. For instance, although Zalmoxis already uses a solid-phase EOS when the planet is initially solidified, it could be further improved by selecting a liquid EOS when the planet begins in a fully molten state and a mixed-phase EOS when it starts in a partially molten (mushy) regime. Although phase transitions are second-order effects compared to compositional parameters like core mass fraction or volatile content, they still significantly influence internal energy transport and melting behavior, as highlighted by Duffy et al. [2015]. Therefore, while the current initialization is reasonably adequate, incorporating phase-aware EOS selection in Zalmoxis would improve internal consistency and may enhance the fidelity of thermal and structural evolution modeling when coupled with Aragog.

In addition to enhancing physical accuracy, the integration of Zalmoxis also improves computational efficiency. By computing the internal structure in advance and passing a converged profile to Aragog, Zalmoxis eliminates the need for iterative root-finding procedures within the thermal evolution solver. This decouples structural convergence from Aragog's evolutionary loop, allowing the thermal evolution to proceed on a fixed, physically consistent interior structure. As a result, simulations of higher-mass planets, which were previously not feasible in PROTEUS due to limitations in structural modeling, are now possible and run efficiently.

4.3 Implications of the fiducial case

The fiducial case presented in Section 3.3 demonstrates overall the expected thermal and structural evolution of a fully molten, Earth-mass (1 $M_\oplus$) rocky planet undergoing secular cooling. By using Zalmoxis for the initial interior structure setup and Aragog for subsequent thermal evolution, the simulation achieves a physically self-consistent picture of mantle crystallization. The results reveal a characteristic bottom-up solidification process, accompanied by an increase in mantle viscosity and a corresponding decline in convective heat transport, in line with theoretical expectations for such a planetary interior (Nicholls et al. [2024], Lichtenberg and Miguel [2025]).

More specifically, starting from a fully molten mantle with high initial temperatures and an oxidizing surface environment, the model traces the planet's transition from a vigorously convecting, low-viscosity interior to a more rigid and thermally stratified state over nearly $\sim 8 \times 10^5$ years or ~ 0.8 Myr. This magma ocean lifetime lies at the lower end of the range reported by Lebrun et al. [2013], who found that the duration of the magma ocean phase can vary between 0.8 and 2 Myr depending on the choice of mantle solidus and liquidus curves. During this time, the lower mantle cools relatively slowly, losing about 600 K, while the upper mantle experiences a much steeper temperature drop exceeding 2300 K, establishing a pronounced thermal gradient that drives changes in mantle rheology and convection. As solidification proceeds, mantle viscosity increases by orders of magnitude, reducing convective heat transport efficiency and causing an overall decline in heat flux. As the planet's solidification rate decreases, the melt fraction declines more slowly. Concurrent volatile outgassing, particularly of H_2O, builds atmospheric reservoirs early on, before stabilizing as interior volatile sources diminish.

Despite the global melt fraction dropping below 1% by the end of the simulation, several unphysical features in the rheological front evolution reveal

limitations in Aragog's current method for computing the RF. Most notably, panel (b) of Figure 3.6 shows a persistent bump-like feature beginning around 4.4×10^3 years, associated with a region between approximately 10 GPa and 40 GPa that remains nearly fully molten throughout the simulation (see panel (b) of Figure 3.7). Since the RF is computed as the depth at which the melt fraction reaches a fixed threshold of 0.3, this persistent high-melt region introduces degeneracies in locating the front. In such cases, the threshold intersects the melt profile at multiple depths, and since the current method simply picks the point closest to the threshold, is introducing ambiguity. This selection method breaks the expected monotonic behavior of RF propagation in bottom-up solidification, resulting in unstable features in Figure 3.8(e). For example, minor instabilities in the RF position between $\sim 1 \times 10^4$ and $\sim 2 \times 10^4$ years are due to the 0.3 melt fraction threshold crossing the melt profile twice in that time window, near the surface and deeper within the mantle. This creates ambiguity in selecting the correct depth for the RF, leading to erratic jumps. Similarly, the apparent recession of the RF, where the front moves downward to $\sim 0.92 R_p$ after stalling at the surface, reflects another unphysical behavior. In this later stage, the simulation enters an almost fully molten regime, and the RF should be computed from the global melt fraction being $< 1\%$. However, the corresponding 1% melt fraction line again intersects the profile at two radial positions, causing the same ambiguity. These behaviors point to two key limitations: the persistent bump-like melt-fraction feature between 10 GPa and 40 GPa, which is non-physical and still under investigation in Aragog, and the broader issue that the current threshold-based RF tracking method is only suited for monotonic, bottom-up solidification and fails in scenarios involving more complex thermal evolution with multiple melt-fraction intersections.

Moreover, while the overall trends in outgoing longwave radiation and net atmospheric flux in Figure 3.8(a) align with those reported by Nicholls et al. [2024], the abrupt behavior of the net internal flux appears anomalous. Although the sustained non-zero net internal flux observed from $\sim 7 \times 10^4$ years onward in the simulation shown in Figure 3.8(a) may reflect continued cooling, as also noted by Nicholls et al. [2024], the sharp spike between 5×10^4 and 6×10^4 years is likely unphysical. Plausible explanations for this behavior are the concurrent rheological front instabilities and the persistent high-melt region between 10 GPa and 40 GPa. Furthermore, unlike the continuous overlap of net upward atmospheric and internal heat fluxes seen by Nicholls et al. [2024], which suggests robust coupling between interior and atmosphere, the near-zero net flux observed in Figure 3.8(a) implies weakened or disrupted interior-atmosphere coupling during this phase. This discrepancy suggests that the current implementation of the coupling method in Aragog is not yet fully stable or accurate, likely due to the underlying limitations in melt fraction calculation described earlier.

4.4 Implications of the study of the evolution of 1 to 7 $M_\oplus$ Earth-like rocky exoplanets

4.4.1 Model limitations and challenges

Before interpreting the results presented in Section 3.4, it is important to consider the known limitations of Aragog, some of which, due to reasons not yet understood, were already discussed in Section 4.3. These primarily involve the bump-like feature observed between approximately 10 GPa and 40 GPa, as well as the non-monotonic behavior of the net internal flux. Consequently, the simulation results across the 1 to 7 $M_\oplus$ mass range in Section 3.4 should be regarded as experimental in nature, with considerable future work needed to make them fully reliable. Only the $1 - 2 M_\oplus$ planets reach full solidification and exhibit the expected bottom-up crystallization behavior consistent with previous studies (Nicholls et al. [2024]), while the results for planets with masses $\geq 3 M_\oplus$ remain questionable and should be interpreted with caution.

A further major limitation, not previously discussed, contributing to the unreliability of results for planets with masses $\geq 3 M_\oplus$ arises from the melting curve data implemented in Aragog. More specifically, the liquidus melting curves from Monteux et al. [2016] are paired with a simplified solidus curve approximated as a constant 600 K offset below the liquidus to avoid unphysical crossovers at pressures above 400 GPa. While this approach provides a consistent approximation in regimes where experimental constraints are sparse and melting curves must be extrapolated, it reduces confidence in the model predictions above roughly $300 - 400$ GPa. This limitation likely explains the irregular cooling behavior and non-physical features observed in intermediate and high-mass planet simulations presented in Section 3.4. Moreover, since Aragog computes energy fluxes locally (Bower et al. [2022]), inaccuracies in high-pressure melting behavior propagate through the thermal evolution, making results for planets above 2 $M_\oplus$ unreliable. Additionally, the current numerical melting curve limit at 1 TPa restricts simulations of planets with $\geq 8 M_\oplus$, preventing solidification onset from being reached despite repeated attempts. The current Aragog implementation also suffers from dimensional mismatch errors for planets above $\sim 2 M_\oplus$ when initializing the mantle's thermal profile using an adiabat. Therefore, extending the melting

curve parameter space and incorporating adiabatic thermal gradients for higher-mass planets are essential future improvements. Once the melting curve parameter space in Aragog is extended and the adiabatic thermal gradient functions correctly for planets with masses $\geq 3M_{\oplus}$, more systematic explorations, potentially through grid-based parameter sweeps based on Bayesian inference, could better constrain the molten-solid transition regime as a function of planetary mass and improve the physical reliability of the modeled thermal evolution.

4.4.2 Trends in crystallization timescales and melt fractions

Despite these limitations, some preliminary observations can still be made from the results presented in Section 3.4. First, a clear dependence of crystallization timescales on planetary mass emerges in Figure 3.9. Higher-mass planets, which begin with elevated basal temperatures to establish a fully molten state, generally resist solidification longer, resulting in sustained higher melt fractions, as also noted by Nicholls et al. [2024]. Indeed, while lower-mass planets ($\leq 2M_{\oplus}$) rapidly solidify their mantles within relatively short geological timescales, reaching near-complete crystallization early in their evolution, more massive planets exhibit significantly prolonged solidification phases, with substantial interior melt fractions persisting over billions of years. As Nicholls et al. [2024] pointed out, this behavior arises because higher-mass planets indeed tend to retain heat longer and possess deeper magma oceans, resulting in slower cooling rates. Moreover, the cooling rate decreases as solidification advances, mainly due to the latent heat released during crystallization, which reduces the rate of cooling (Foley et al. [2020], Sahu et al. [2025]). As a result, planets in the $3-5M_{\oplus}$ range cool more slowly, reaching radiative equilibrium before attaining complete solidification. In contrast, 6 and 7 $M_{\oplus}$ achieve neither, suggesting that under the assumed initial and boundary conditions, their solidification timescales may exceed the age of the system, and further crystallization would continue beyond the modeled time span. Extending the simulation time for $6-7M_{\oplus}$ planets and performing simulations for planets beyond $> 7M_{\oplus}$ would be valuable to further explore whether these trends persist or new behaviors emerge at the upper mass range of rocky planets.

The time evolution of global melt fraction profiles in Figure 3.11 provides further insight into the mass-dependent crystallization behavior described earlier. For the low-mass planets ($1-2M_{\oplus}$), the profiles show a smooth and monotonic decline over time, indicating relatively uniform cooling and efficient crystallization throughout the mantle. However, the observation that the 2 $M_{\oplus}$ case maintains lower melt fractions than the 1 $M_{\oplus}$ case throughout the simulation and completes solidification significantly earlier (0.05 Myr vs. 0.33 Myr) is somewhat unexpected. In general, higher-mass planets are anticipated to retain heat longer due to their larger thermal reservoirs and slower cooling rates Sahu et al. [2025]. This apparent deviation from the anticipated trend needs further investigation once the current limitations related to the Aragog implementation, as described above, are resolved. In contrast, intermediate-mass planets ($3-5M_{\oplus}$) exhibit more complex and irregular behavior. Their melt fraction profiles display fluctuations, particularly around and after $\sim 10^4$ years, which reflect variations in the dynamic evolution of the crystallizing mantle. These irregularities may result from inaccuracies in the high-pressure melting behavior incorporated in Aragog, which affect thermal evolution at pressures above roughly $300-400$ GPa. For the most massive planets ($6-7M_{\oplus}$), their global melt fraction profiles remain consistently higher than those of smaller planets beyond $\sim 10^5$ years, indicating that these planets retain substantial interior melt for extended periods, in agreement with Nicholls et al. [2024].

4.4.3 Magma temperature evolution and cooling pathways

The simulation results in Figure 3.10 highlight a possible mass-dependent suppression of volatile outgassing during early planetary cooling. Although larger planets may initially contain greater volatile inventories, the slower cooling in massive mantles inhibits efficient degassing. Consequently, total surface atmospheric pressures and surface H_2O pressures are markedly lower on higher-mass planets at the end of the simulations, implying that atmospheric development in these worlds could be hindered or delayed. This interpretation is supported by the time-evolution profiles shown in Figures 3.13 and 3.14, where low-mass planets maintain higher total surface pressures and surface H_2O pressures throughout the simulation compared to their more massive counterparts. Within the intermediate mass range ($3-5M_{\oplus}$), both total surface pressure and surface H_2O pressure scale inversely with planetary mass. For example, the 3 $M_{\oplus}$ planet outgasses more efficiently, sustaining consistently higher surface pressure profiles than the 4 $M_{\oplus}$ and 5 $M_{\oplus}$ planets over the full simulation duration. This trend is similarly reflected in the surface H_2O pressure profiles. A comparable inverse mass dependence is observed in the high-mass group ($6-7M_{\oplus}$), where the 6 $M_{\oplus}$ planet exhibits more effective outgassing, resulting in higher total surface pressure and surface H_2O pressure profiles relative to the 7 $M_{\oplus}$ planet throughout the simulation period. No-

tably, H_2O becomes the most dominant outgassed volatile in the atmosphere only for the planets that achieve complete mantle solidification, namely the 1 and 2 $M_\oplus$ cases, as seen in the right panels of Figures B.7, B.8, and B.9 in Appendix B. This is line with observations made by Nicholls et al. [2024] that recently solidified planets typically host atmospheres consisting primarly of H_2O- or H_2 in the absence of escape. Furthermore, planets with masses greater than 3 $M_\oplus$ tend to develop CO_2-dominated atmospheres, which could explain their delayed solidification. The outgassing of such an opaque gas can induce a strong greenhouse effect, significantly delaying the planet's cooling process (Nicholls et al. [2024] and references therein). Overall, these results reinforce the conclusion that increasing planetary mass tends to suppress volatile release during the early cooling phase, likely due to prolonged mantle melt retention and slower cooling rates.

Interpreting the dependence of final magma temperatures on planetary mass is less straightforward than for surface pressure trends, as seen in the middle panel of Figure 3.10 and the magma temperature profiles in Figure 3.12. Simulation termination criteria vary across the mass range and play an important role. For low-mass planets (1 and 2 $M_\oplus$), simulations end upon mantle solidification (global melt fraction $< 1\%$). Here, the 2 $M_\oplus$ planet shows a notably higher final magma temperature than the 1 $M_\oplus$ case despite solidifying earlier (0.05 Myr vs. 0.33 Myr). This could be because the 2 $M_\oplus$ planet, having a larger thermal reservoir and higher internal pressures, retains more latent heat during rapid crystallization, resulting in a higher equilibrium temperature at solidification compared to the 1 $M_\oplus$ planet. This trend does not extend to intermediate-mass planets (3–5 $M_\oplus$), where simulations terminate upon reaching radiative equilibrium rather than complete solidification. In this mass range, final magma temperatures generally decrease with increasing mass, reflecting more efficient surface cooling in mantles that remain partially molten within the simulation timeframe. However, this apparent reversal may not reflect a true physical trend but rather result from differing termination criteria and Aragog's imperfect treatment of internal heat flux. Supporting this, net internal heat fluxes for planets above 3 $M_\oplus$ (see Figures B.8 and B.9 in Appendix B) show patterns consistent with partial decoupling between internal evolution and surface conditions: a persistent non-zero flux, a sharp spike, slight decline, then leveling off. This indicates surface temperature stabilization is governed more by atmospheric radiative balance than ongoing mantle crystallization. The surface magma temperature profiles in Figure 3.12 further add complexity: low-mass planets stabilize early, intermediate masses show delayed, non-monotonic cooling with temperature crossovers, and the most massive planets cool efficiently early on but remain hotter than some intermediate masses at simulation end. These puzzling results and the deviation from expected mass-dependent cooling warrant further study once current limitations in the Aragog implementation are addressed.

4.4.4 Comparison with previous studies and future directions

Simulating the thermal and volatile evolution of massive rocky exoplanets remains challenging, particularly when it comes to choosing realistic initial volatile budgets. In this thesis, a fixed volatile inventory was assumed and atmospheric escape was neglected for simplicity. However, prior research highlights that atmospheric escape plays a crucial role in planetary cooling, especially for Earth-like lava planets with large water inventories. For instance, Hamano et al. [2015] demonstrate that planets with water inventories equivalent to about 10 Earth oceans may cool primarily through atmospheric escape (Nicholls et al. [2024]). Similarly, Schaefer et al. [2016] showed how volatile loss can dramatically reshape secondary atmospheres, as exemplified by their study of GJ 1132b (1.62 $M_\oplus$, 1.16 $R_\oplus$). Since larger planets generally hold greater water inventories, their atmospheres may contain substantial water vapor, which prolongs mantle solidification (Sahu et al. [2025]). This underscores the importance of physically plausible initial volatile budgets for future models of magma ocean evolution and volatile cycling in massive terrestrial exoplanets. Given the difficulty of estimating initial water content precisely, a range of plausible inventories is typically explored in the literature (Dorn and Lichtenberg [2021], Bower et al. [2022], Hamano et al. [2015]).

While the GJ 1132b study of Schaefer et al. [2016] demonstrates the importance of atmospheric escape for volatile evolution, their thermal model uses a simplified parameterization. Only two bulk temperatures, a mantle-potential temperature and a surface temperature, are being tracked, and switching between a magma-ocean and a solid-state convection regime takes places with a prescribed thermal boundary layer. Interior-atmosphere coupling is handled in a single "box" in the sense that mass exchange and heat loss are applied uniformly, without resolving how melt fraction and volatile content vary with depth or feed back on one another from cell to cell. By contrast, the Zalmoxis-Aragog pipeline within the PROTEUS framework solves the radial structure and energy balance layer-by-layer. Melt fraction, density, pressure, and volatile solubility are updated self-consistently

at every depth step, so that changes in one layer propagate throughout the mantle and into the atmosphere in real time. This higher-resolution approach has the potential to capture feedbacks that a two-temperature parameterisation cannot, for example, how a deep melt reservoir or a compositionally stratified layer can delay or accelerate surface cooling. Consequently, incorporating atmospheric escape into future simulations with the Zalmoxis-Aragog pipeline within the PROTEUS framework and allowing the initial water inventory to vary will provide a more realistic test of whether massive rocky planets can cool and solidify under volatile-rich conditions. Revisiting Schaefer et al. [2016]'s GJ 1132b case using PROTEUS would be a natural next step to explore how depth-dependent thermal evolution affects volatile distribution and solidification timing.

Simplified parameterized magma ocean models like Schaefer et al. [2016] continue to be widely used to interpret recent JWST observations. For example, Zieba et al. [2023] apply this approach to TRAPPIST-1c, concluding that its lack of a thick CO_2-rich atmosphere likely reflects either significant atmospheric loss or a volatile-poor formation history. Their model, adapted from Schaefer et al. [2016], triggers the transition from a magma ocean to a passive outgassing regime once surface temperatures fall below the silicate melting point, but does not treat interior evolution in a fully self-consistent, depth-resolved manner. Similarly, the recently developed coupled interior-atmosphere SERPINT model by Sahu et al. [2025] simulates GJ 486b's thermal and atmospheric evolution assuming Earth-like interiors and a water inventory of 10 Earth oceans, finding substantial atmospheric water retention after cooling. SERPINT's thermal evolution model, also adapted from Schaefer et al. [2016], starts with a partially solidified lower mantle and lacks a depth-resolved volatile transport scheme. In contrast, the PROTEUS pipeline continuously tracks melt fraction, pressure, and volatile solubility across depth and time, enabling more realistic coupling between deep interior and surface processes. As atmospheric characterization of planets around M dwarfs advances, using such detailed, depth-resolved models will be crucial to distinguish between low initial volatile inventories and escape-driven volatile depletion.

Moreover, just like the model presented in Sahu et al. [2025], the PROTEUS framework is also constrained to one dimension and thus cannot capture the three-dimensional nature of mantle convection and surface-atmosphere interactions. As Sahu et al. [2025] point out, real planetary mantles convect in three dimensions at spatially variable rates, potentially leading to chemical and thermal heterogeneities. This limitation becomes particularly relevant for tidally locked exoplanets like GJ 486b, where hemispheric differences in surface temperature may result in asymmetrical cooling, outgassing, and escape processes. For instance, Meier et al. [2024] showed that the dayside of GJ 486b may experience faster cooling and atmospheric loss compared to the nightside, potentially giving rise to persistent winds from the cold to the hot hemisphere. Such dynamical effects are inherently inaccessible to 1D models like PROTEUS and SERPINT, underscoring the importance of developing higher-dimensional treatments in future studies to fully capture spatial variability in planetary evolution.

Finally, although this study explored a limited range of planetary masses due to time constraints, grid-based parameter sweeps would provide a more comprehensive understanding of the non-linear scaling of internal properties with mass. For instance, because the transition in interior structure and dynamics from 1 to 2 $M_\oplus$ may be significantly more dramatic than changes observed between 6 and 7 $M_\oplus$, there is a clear need for dense sampling in the lower-mass regime. Future work applying the Zalmoxis-Aragog-PROTEUS modeling framework to characterize benchmark rocky exoplanets, such as GJ 1132b (Schaefer et al. [2016]), TRAPPIST-1c (Zieba et al. [2023]), and GJ 486b (Sahu et al. [2025]), will be crucial for capturing more realistic constraints on their volatile inventories, thermal evolution, and atmospheric retention, improving interpretation of current and future observations.

5 CONCLUSIONS

This work has introduced and validated Zalmoxis, an open-source Python-based planetary structure modeling tool for the interiors of terrestrial exoplanets such as super-Earths and sub-Neptunes. Given an input mass of up to 50 $M_\oplus$ and specified core mass fraction(s), Zalmoxis uses a shooting method to solve the radial planetary structure in terms of mass, density, pressure, and gravity from the core to the surface.

Zalmoxis is flexible, supporting a wide range of differentiated interiors, from rocky super-Earths to water-rich worlds, by allowing variable compositions in the iron core, silicate mantle, and water ice layers. It handles pure-component and layered models with or without metallic cores, covering diverse planetary types. Additionally, Zalmoxis is computationally efficient, solving structures in seconds to minutes, enabling rapid exploration of broad parameter spaces for systematic interior studies. Despite its strengths, Zalmoxis has some limitations. It cannot model extended gaseous envelopes or complex atmospheres, limiting its use for sub-Neptunes and gas-rich planets. Water is treated as a single ice

phase, ignoring its complex behavior under varying pressures and temperatures. The assumption of fully differentiated interiors with sharp boundaries oversimplifies mixed-phase mineralogy. Future improvements should include phase-dependent equations of state, mineralogical diversity, mixed interiors, and thermal profiles to enhance accuracy and expand applicability.

Integration of Zalmoxis into the PROTEUS pipeline enables consistent thermochemical and volatile evolution simulations for massive planets previously difficult to model, while improving computational efficiency. The combined Zalmoxis-Aragog framework successfully captures key processes like bottom-up solidification and volatile outgassing in an Earth-mass magma ocean case, though some non-physical melt fraction features remain under investigation.

This thesis also used the Zalmoxis-Aragog pipeline to model the thermal and structural evolution of rocky exoplanets from 1 to 7 $M_{\oplus}$. Simulations reproduce expected solidification for low-mass planets ($1 - 2M_{\oplus}$), but results for higher masses ($\geq 3M_{\oplus}$) are uncertain due to limitations in melting curve data and thermal modeling at high pressures, causing unreliable melt and heat flux profiles. Preliminary results show crystallization timescales increase with mass, leading to longer magma ocean lifetimes, slower cooling, and suppressed volatile outgassing on massive planets, potentially delaying atmospheric development. Volatile release, especially H_2O, is more efficient on lower-mass planets that solidify quickly. Final magma temperatures vary complexly with mass, influenced by model limits and termination criteria. Future work will extend melting curve data and improve thermal gradient modeling to better assess massive rocky exoplanet evolution and habitability.

Simulating the thermal and volatile evolution of massive rocky exoplanets remains challenging due to uncertainties in initial volatile inventories and the critical role of atmospheric escape, which was neglected in this study for simplicity. Prior work demonstrates that atmospheric escape, especially for planets with large water inventories, can significantly influence cooling and atmospheric composition, highlighting the need to explore a range of plausible volatile budgets in future models. Existing parameterized models, like those by Schaefer et al. [2016]), use simplified approaches that lack self-consistent, depth-resolved interior evolution. By contrast, the PROTEUS framework tracks melt fraction, pressure, and volatile solubility continuously across depth and time, enabling a more realistic representation of interior-surface feedbacks. Incorporating atmospheric escape and variable initial volatile inventories in future simulations with PROTEUS will better constrain magma ocean evolution and volatile cycling in massive terrestrial exoplanets. However, both PROTEUS and comparable models like SERPINT (Sahu et al. [2025]) remain one-dimensional and cannot capture three-dimensional mantle convection or hemispheric differences critical for tidally locked planets, motivating future development of higher-dimensional models. Applying the PROTEUS-based framework to well-studied benchmark exoplanets such as GJ 1132b, TRAPPIST-1c, and GJ 486b will enhance understanding of their volatile and thermal histories, aiding interpretation of current and forthcoming observational data.

Overall, Zalmoxis represents a significant advance in open-source modeling of exoplanet interiors, laying a foundation for future enhancements incorporating improved mineral physics, complex phase transitions, and a wider diversity of planetary compositions. Its integration within the PROTEUS pipeline further enhances its value by enabling coupled simulations of planetary thermochemical evolution for diverse studies. This mix of flexibility, speed, and accuracy makes Zalmoxis an important tool for studying the interiors and development of super-Earths, sub-Neptunes, and water-rich planets, helping improve interpretation of observations and support future exoplanet missions.

DATA AVAILABILITY

PROTEUS and Aragog are open source software available on GitHub. Zalmoxis, developed during this thesis, is now also hosted on GitHub.

ACKNOWLEDGEMENTS

Academic and research support

I would first like to sincerely thank my supervisor, Tim Lichtenberg, for his invaluable feedback, ideas, and motivation, always supporting my ambitious research goals. Without his guidance and encouragement, I would not have had the opportunity to pursue this research.

I am also very grateful to the Forming Worlds Lab research group for providing such a welcoming and collaborative environment during group meetings. Special thanks go to Mariana and Emma for their invaluable assistance in smoothing the installation of PROTEUS, which significantly accelerated my workflow for this thesis. Their patience and thoughtful feedback in answering my questions were deeply appreciated.

Tools and resources

I wish to acknowledge the use of Grammarly and ChatGPT for language editing support, as well as

GitHub Copilot for suggestions during code development. These tools were used to support clarity in writing and efficiency in coding.

Personal acknowledgements

To Nadia, my most supportive friend and thesis study buddy, thank you for encouraging me to come into the research office every day and for making the work environment pleasant and motivating. I also wish to thank my dear Martin, a fervent supporter of my dreams, who embraced my passion for astronomy as a beautiful part of who I am.

I am profoundly thankful for my family back home, especially my parents, whose tremendous support, love, and sacrifices have made my journey possible. I also want to dedicate my gratitude to both of my grandmothers. Although they may not have fully understood what I was studying, they were always proud in their hearts and I believe they are proud now, watching from between the stars.

I am also deeply grateful to the country in which I was born, Romania. In its honor, I named my code *Zalmoxis*, after the deity of the Getae and Dacians, ancient people of the lower Danube region (present-day Romania and Bulgaria). The name is derived from the Thracian word zamol, meaning "earth", symbolizing not only a deep connection to my roots but also the foundation of my work, including the study of planetary interiors.

Finally, I wish to acknowledge my former high school astronomy professor and mentor, Dan Oniciuc, who first introduced me to the wonders of astronomy and inspired me to dream big. I hope he is smiling while reading these lines, perhaps thinking about his little supernova. I am also deeply grateful to George Teleman for his unconditional and generous support throughout my academic journey. I also wish to thank all those who continue to hold a place in my life and contribute to it in countless meaningful ways.

REFERENCES

A. Aitta. Venus' internal structure, temperature and core composition. *Icarus*, 218(2):967–974, 2012. ISSN 0019-1035. doi:https://doi.org/10.1016/j.icarus.2012.01.007. URL https://www.sciencedirect.com/science/article/pii/S001910351200022X.

Denis Andrault, Nathalie Bolfan-Casanova, Giacomo Lo Nigro, Mohamed A. Bouhifd, Gaston Garbarino, and Mohamed Mezouar. Solidus and liquidus profiles of chondritic mantle: Implication for melting of the earth across its history. *Earth and Planetary Science Letters*, 304(1):251–259, 2011. ISSN 0012-821X. doi:https://doi.org/10.1016/j.epsl.2011.02.006. URL https://www.sciencedirect.com/science/article/pii/S0012821X1100077X.

S Bloot, Y Miguel, M Bazot, and S Howard. Exoplanet interior retrievals: core masses and metallicities from atmospheric abundances. *Monthly Notices of the Royal Astronomical Society*, 523 (4):6282–6292, June 2023. ISSN 1365-2966. doi:10.1093/mnras/stad1873. URL http://dx.doi.org/10.1093/mnras/stad1873.

A. Boujibar, P. Driscoll, and Y. Fei. Super-earth internal structures and initial thermal states. *Journal of Geophysical Research: Planets*, 125(5), May 2020. doi:10.1029/2019je006124.

Dan J. Bower, Patrick Sanan, and Aaron S. Wolf. Numerical solution of a non-linear conservation law applicable to the interior dynamics of partially molten planets. *Physics of the Earth and Planetary Interiors*, 274: 49–62, January 2018. ISSN 0031-9201. doi:10.1016/j.pepi.2017.11.004. URL http://dx.doi.org/10.1016/j.pepi.2017.11.004.

Dan J. Bower, Kaustubh Hakim, Paolo A. Sossi, and Patrick Sanan. Retention of water in terrestrial magma oceans and carbon-rich early atmospheres. *The Planetary Science Journal*, 3(4):93, April 2022. ISSN 2632-3338. doi:10.3847/psj/ac5fb1. URL http://dx.doi.org/10.3847/PSJ/ac5fb1.

Ronald E. Cohen, Oguz Gülseren, and Russell J. Hemley. Accuracy of equation of state formulations, 2000. URL https://arxiv.org/abs/cond-mat/9905389.

Caroline Dorn and Tim Lichtenberg. Hidden water in magma ocean exoplanets. *The Astrophysical Journal Letters*, 922(1):L4, November 2021. ISSN 2041-8213. doi:10.3847/2041-8213/ac33af. URL http://dx.doi.org/10.3847/2041-8213/ac33af.

Caroline Dorn, Amir Khan, Kevin Heng, James A. Connolly, Yann Alibert, Willy Benz, and Paul Tackley. Can we constrain the interior structure of rocky exoplanets from mass and radius measurements? *Astronomy amp; Astrophysics*, 577, May 2015. doi:10.1051/0004-6361/201424915.

Caroline Dorn, Dan J. Bower, and Antoine Rozel. *Assessing the Interior Structure of Terrestrial Exoplanets with Implications for Habitability*, page 3111–3135. Springer International Publishing, 2018. ISBN 9783319553337. doi:10.1007/978-3-319-55333-7_66. URL http://dx.doi.org/10.1007/978-3-319-55333-7_66.

Courtney D. Dressing, David Charbonneau, Xavier Dumusque, Sara Gettel, Francesco Pepe, Andrew Collier Cameron, David W. Latham, Emilio Molinari, Stéphane Udry, Laura Affer, and et al. The mass of kepler-93b and the composition of terrestrial planets. *The Astrophysical Journal*, 800(2):135, Feb 2015. doi:10.1088/0004-637x/800/2/135.

T. Duffy, N. Madhusudhan, and K.K.M. Lee. Mineralogy of super-earth planets. *Treatise on Geophysics*, page 149–178, 2015. doi:10.1016/b978-0-444-53802-4.00053-1.

Adam M. Dziewonski and Don L. Anderson. Preliminary reference earth model. *Physics of the Earth and Planetary Interiors*, 25(4):297–356, Jun 1981. doi:10.1016/0031-9201(81)90046-7.

Linda T. Elkins-Tanton and Sara Seager. Ranges of atmospheric mass and composition of super-earth exoplanets. *The Astrophysical Journal*, 685(2):1237, oct 2008. doi:10.1086/591433. URL https://dx.doi.org/10.1086/591433.

Linda T. Elkins-Tanton and Sara Seager. Coreless terrestrial exoplanets. *The Astrophysical Journal*, 688(1):628–635, Nov 2008. doi:10.1086/592316.

Bradford J Foley, Christine Houser, Lena Noack, and Nicola Tosi. The heat budget of rocky planets. In *Planetary Diversity*, 2514-3433, pages 4–1 to 4–60. IOP Publishing, 2020. ISBN 978-0-7503-2140-2. doi:10.1088/2514-3433/abb4d9ch4. URL https://dx.doi.org/10.1088/2514-3433/abb4d9ch4.

J. J. Fortney, M. S. Marley, and J. W. Barnes. Planetary radii across five orders of magnitude in mass and stellar insolation: Application to transits. *The Astrophysical Journal*, 659(2): 1661–1672, Apr 2007. doi:10.1086/512120.

J. J. Fortney, S. H. Glenzer, M. Koenig, B. Militzer, D. Saumon, and D. Valencia. Frontiers of the physics of dense plasmas and planetary interiors: Experiments, theory, and applications. *Physics of Plasmas*, 16(4), April 2009. ISSN 1089-7674. doi:10.1063/1.3101818. URL http://dx.doi.org/10.1063/1.3101818.

Yan-Xiang Gong and Ji-Lin Zhou. The silicate and carbon-rich models of corot-7b, kepler-9d and kepler-10b. *Research in Astronomy and Astrophysics*, 12(6):678–692, May 2012. ISSN 1674-4527. doi:10.1088/1674-4527/12/6/008. URL http://dx.doi.org/10.1088/1674-4527/12/6/008.

R. J. Graham, Tim Lichtenberg, Ryan Boukrouche, and Raymond T. Pierrehumbert. A multispecies pseudoadiabat for simulating condensable-rich exoplanet atmospheres. *The Planetary Science Journal*, 2(5):207, Oct 2021. doi:10.3847/psj/ac214c.

O. Grasset, J. Schneider, and C. Sotin. A study of the accuracy of mass-radius relationships for silicate-rich and ice-rich planets up to 100 earth masses. *The Astrophysical Journal*, 693(1):722–733, Mar 2009. doi:10.1088/0004-637x/693/1/722.

Keiko Hamano, Hajime Kawahara, Yutaka Abe, Masanori Onishi, and George L. Hashimoto. Lifetime and spectral evolution of a magma ocean with a steam atmosphere: Its detectability by future direct imaging. *The Astrophysical Journal*, 806(2):216, Jun 2015. doi:10.1088/0004-637x/806/2/216.

George Helffrich, Ramon Brasser, and Anat Shahar. The chemical case for mercury mantle stripping. *Progress in Earth and Planetary Science*, 6(1), Dec 2019. doi:10.1186/s40645-019-0312-z.

Chenliang Huang, David R Rice, and Jason H Steffen. Magrathea: an open-source spherical symmetric planet interior structure code. *Monthly Notices of the Royal Astronomical Society*, 513(4):5256–5269, April 2022. ISSN 1365-2966. doi:10.1093/mnras/stac1133. URL http://dx.doi.org/10.1093/mnras/stac1133.

C. P. Johnstone, M. Bartel, and M. Güdel. The active lives of stars: A complete description of the rotation and xuv evolution of f, g, k, and m dwarfs. *Astronomy amp; Astrophysics*, 649, May 2021. doi:10.1051/0004-6361/202038407.

Jun Korenaga. On the likelihood of plate tectonics on super-earths: Does size matter? *The Astrophysical Journal*, 725(1), Nov 2010. doi:10.1088/2041-8205/725/1/l43.

Sébastien Le Maistre, Attilio Rivoldini, Alfonso Caldiero, Marie Yseboodt, Rose-Marie Baland,

Mikael Beuthe, Tim Van Hoolst, Véronique Dehant, William M. Folkner, Dustin Buccino, and et al. Spin state and deep interior structure of mars from insight radio tracking. *Nature*, 619 (7971):733–737, Jun 2023. doi:10.1038/s41586-023-06150-0.

T. Lebrun, H. Massol, E. Chassefière, A. Davaille, E. Marcq, P. Sarda, F. Leblanc, and G. Brandeis. Thermal evolution of an early magma ocean in interaction with the atmosphere. *Journal of Geophysical Research: Planets*, 118(6):1155–1176, Jun 2013. doi:10.1002/jgre.20068.

Tim Lichtenberg and Yamila Miguel. *Super-Earths and Earth-like exoplanets*, page 51–112. Elsevier, 2025. ISBN 9780323997638. doi:10.1016/b978-0-323-99762-1.00122-4. URL http://dx.doi.org/10.1016/B978-0-323-99762-1.00122-4.

Tim Lichtenberg, Dan J. Bower, Mark Hammond, Ryan Boukrouche, Patrick Sanan, Shang-Min Tsai, and Raymond T. Pierrehumbert. Vertically Resolved Magma Ocean-Protoatmosphere Evolution: H_2, H_2O, CO_2, CH_4, CO, O_2, and N_2 as Primary Absorbers. *Journal of Geophysical Research (Planets)*, 126(2):e06711, February 2021. doi:10.1029/2020JE006711.

Tim Lichtenberg et al. Title tbd. in preparation, in prep.

Zifan Lin, Saverio Cambioni, and Sara Seager. Most high-density exoplanets are unlikely to be remnant giant-planet cores, 2024. URL https://arxiv.org/abs/2410.12640.

Rafael Luque and Enric Pallé. Density, not radius, separates rocky and water-rich small planets orbiting m dwarf stars. *Science*, 377(6611): 1211–1214, September 2022. ISSN 1095-9203. doi:10.1126/science.abl7164. URL http://dx.doi.org/10.1126/science.abl7164.

A. Léger, F. Selsis, C. Sotin, T. Guillot, D. Despois, D. Mawet, M. Ollivier, A. Labèque, C. Valette, F. Brachet, B. Chazelas, and H. Lammer. A new family of planets? "ocean-planets". *Icarus*, 169(2):499–504, June 2004. ISSN 0019-1035. doi:10.1016/j.icarus.2004.01.001. URL http://dx.doi.org/10.1016/j.icarus.2004.01.001.

Nikku Madhusudhan, Kanani K. M. Lee, and Olivier Mousis. A possible carbon-rich interior in super-earth 55 cancri e. *The Astrophysical Journal*, 759(2):L40, October 2012. ISSN 2041-8213. doi:10.1088/2041-8205/759/2/l40. URL http://dx.doi.org/10.1088/2041-8205/759/2/L40.

Nikku Madhusudhan, Matthew C. Nixon, Luis Welbanks, Anjali A. A. Piette, and Richard A. Booth. The interior and atmosphere of the habitable-zone exoplanet k2-18b. *The Astrophysical Journal Letters*, 891(1):L7, February 2020. ISSN 2041-8213. doi:10.3847/2041-8213/ab7229. URL http://dx.doi.org/10.3847/2041-8213/ab7229.

W.F. McDonough. Compositional model for the earth's core. *Treatise on Geochemistry*, page 547–568, 2003. doi:10.1016/b0-08-043751-6/02015-6.

Tobias G. Meier, Dan J. Bower, Tim Lichtenberg, Mark Hammond, Paul J. Tackley, Raymond T. Pierrehumbert, José A. Caballero, Shang-Min Tsai, Megan Weiner Mansfield, Nicola Tosi, and et al. Geodynamics of super-earth gj 486b. *Journal of Geophysical Research: Planets*, 129(10), Oct 2024. doi:10.1029/2024je008491.

Antoine Mocquet, Pascal Rosenblatt, Véronique Dehant, and Olivier Verhoeven. The deep interior of venus, mars, and the earth: A brief review and the need for planetary surface-based measurements. *Planetary and Space Science*, 59(10):1048–1061, 2011. ISSN 0032-0633. doi:https://doi.org/10.1016/j.pss.2010.02.002. URL https://www.sciencedirect.com/science/article/pii/S0032063310000437. Comparative Planetology: Venus-Earth-Mars.

J. Monteux, D. Andrault, and H. Samuel. On the cooling of a deep terrestrial magma ocean. *Earth and Planetary Science Letters*, 448:140–149, Aug 2016. doi:10.1016/j.epsl.2016.05.010.

NASA Exoplanet Archive. Exoplanet archive plotting tools. https://exoplanetarchive.ipac.caltech.edu/exoplanetplots/, 2025. URL https://exoplanetarchive.ipac.caltech.edu/exoplanetplots/.

Harrison Nicholls, Tim Lichtenberg, Dan J. Bower, and Raymond Pierrehumbert. Magma Ocean Evolution at Arbitrary Redox State. *Journal of Geophysical Research (Planets)*, 129(12):2024JE008576, December 2024. doi:10.1029/2024JE008576.

Harrison Nicholls, Raymond T. Pierrehumbert, Tim Lichtenberg, Laurent Soucasse, and Stef Smeets. Convective shutdown in the atmospheres of lava worlds. , 536(3):2957–2971, January 2025. doi:10.1093/mnras/stae2772.

F. Nimmo. Energetics of the core. *Treatise on Geophysics*, page 27–55, 2015. doi:10.1016/b978-0-444-53802-4.00139-1.

L. Noack, M. Godolt, P. von Paris, A.-C. Plesa, B. Stracke, D. Breuer, and H. Rauer. Can the interior structure influence the habitability of a

rocky planet? *Planetary and Space Science*, 98: 14–29, Aug 2014. doi:10.1016/j.pss.2014.01.003.

L. Noack, D. Höning, A. Rivoldini, C. Heistracher, N. Zimov, B. Journaux, H. Lammer, T. Van Hoolst, and J.H. Bredehöft. Water-rich planets: How habitable is a water layer deeper than on earth? *Icarus*, 277:215–236, Oct 2016. doi:10.1016/j.icarus.2016.05.009.

Lena Noack and Marine Lasbleis. Parameterisations of interior properties of rocky planets. *Astronomy amp; Astrophysics*, 638, Jun 2020. doi:10.1051/0004-6361/202037723.

L. A. Rogers and S. Seager. A framework for quantifying the degeneracies of exoplanet interior compositions. *The Astrophysical Journal*, 712(2):974–991, March 2010. ISSN 1538-4357. doi:10.1088/0004-637x/712/2/974. URL http://dx.doi.org/10.1088/0004-637X/712/2/974.

Chandan K. Sahu, Liton Majumdar, Sudipta Mridha, and Harshit Krishna. Unveiling the interior structure and thermal evolution of super-earth gj 486b, 2025. URL https://arxiv.org/abs/2501.09963.

A. Salvador, H. Massol, A. Davaille, E. Marcq, P. Sarda, and E. Chassefière. The relative influence of h2o and co2 on the primitive surface conditions and evolution of rocky planets. *Journal of Geophysical Research: Planets*, 122(7): 1458–1486, Jul 2017. doi:10.1002/2017je005286.

Laura Schaefer, Katharina Lodders, and Bruce Fegley. Vaporization of the earth: Application to exoplanet atmospheres. *The Astrophysical Journal*, 755(1):41, Jul 2012. doi:10.1088/0004-637x/755/1/41.

Laura Schaefer, Robin D. Wordsworth, Zachory Berta-Thompson, and Dimitar Sasselov. Predictions of the atmospheric composition of gj 1132b. *The Astrophysical Journal*, 829(2):63, September 2016. ISSN 1538-4357. doi:10.3847/0004-637x/829/2/63. URL http://dx.doi.org/10.3847/0004-637X/829/2/63.

J. G. Schulze, J. Wang , J. A. Johnson, B. S. Gaudi, C. T. Unterborn, and W. R. Panero. On the probability that a rocky planet's composition reflects its host star. *The Planetary Science Journal*, 2 (3):113, Jun 2021. doi:10.3847/psj/abcaa8.

S. Seager, M. Kuchner, C. A. Hier-Majumder, and B. Militzer. Mass-radius relationships for solid exoplanets. *The Astrophysical Journal*, 669(2): 1279, nov 2007. doi:10.1086/521346. URL https://dx.doi.org/10.1086/521346.

V. Solomatov. 9.04 - magma oceans and primordial mantle differentiation. In Gerald Schubert, editor, *Treatise on Geophysics*, pages 91–119. Elsevier, Amsterdam, 2007. ISBN 978-0-444-52748-6. doi:https://doi.org/10.1016/B978-044452748-6.00141-3. URL https://www.sciencedirect.com/science/article/pii/B9780444527486001413.

C Sotin, O Grasset, and A Mocquet. Mass–radius curve for extrasolar earth-like planets and ocean planets. *Icarus*, 191(1):337–351, Nov 2007. doi:10.1016/j.icarus.2007.04.006.

Lars Stixrude, Nico de Koker, Ni Sun, Mainak Mookherjee, and Bijaya B. Karki. Thermodynamics of silicate liquids in the deep earth. *Earth and Planetary Science Letters*, 278(3–4):226–232, Feb 2009. doi:10.1016/j.epsl.2008.12.006.

D. C. Swift, J. H. Eggert, D. G. Hicks, S. Hamel, K. Caspersen, E. Schwegler, G. W. Collins, N. Nettelmann, and G. J. Ackland. Mass-radius relationships for exoplanets. *The Astrophysical Journal*, 744(1):59, Dec 2011. doi:10.1088/0004-637x/744/1/59.

P.J. Tackley, M. Ammann, J.P. Brodholt, D.P. Dobson, and D. Valencia. Mantle dynamics in super-earths: Post-perovskite rheology and self-regulation of viscosity. *Icarus*, 225(1):50–61, July 2013. ISSN 0019-1035. doi:10.1016/j.icarus.2013.03.013. URL http://dx.doi.org/10.1016/j.icarus.2013.03.013.

C. T. Unterborn and W. R. Panero. The pressure and temperature limits of likely rocky exoplanets. *Journal of Geophysical Research: Planets*, 124(7): 1704–1716, Jul 2019. doi:10.1029/2018je005844.

Cayman T. Unterborn, Steven J. Desch, Natalie R. Hinkel, and Alejandro Lorenzo Jr. Inward migration of the trappist-1 planets as inferred from their water-rich compositions, 2018. URL https://arxiv.org/abs/1706.02689.

Diana Valencia, Richard J. O'Connell, and Dimitar Sasselov. Internal structure of massive terrestrial planets. *Icarus*, 181 (2):545–554, April 2006. ISSN 0019-1035. doi:10.1016/j.icarus.2005.11.021. URL http://dx.doi.org/10.1016/j.icarus.2005.11.021.

Diana Valencia, Dimitar D. Sasselov, and Richard J. O'Connell. Radius and structure models of the first super-earth planet. *The Astrophysical Journal*, 656(1):545–551, Feb 2007. doi:10.1086/509800.

F. W. Wagner, N. Tosi, F. Sohl, H. Rauer, and T. Spohn. Rocky super-earth interiors. *Astronomy amp; Astrophysics*, 541, May 2012. doi:10.1051/0004-6361/201118441.

Haiyang S. Wang, Charles H. Lineweaver, and Trevor R. Ireland. The elemental abundances (with uncertainties) of the most earth-like planet. *Icarus*, 299:460–474, 2018. ISSN 0019-1035. doi:https://doi.org/10.1016/j.icarus.2017.08.024. URL https://www.sciencedirect.com/science/article/pii/S0019103517302221.

Li Zeng, Dimitar D. Sasselov, and Stein B. Jacobsen. Mass–radius relation for rocky planets based on prem. *The Astrophysical Journal*, 819(2):127, March 2016. ISSN 1538-4357. doi:10.3847/0004-637x/819/2/127. URL http://dx.doi.org/10.3847/0004-637X/819/2/127.

Li Zeng, Stein B. Jacobsen, Dimitar D. Sasselov, Michail I. Petaev, Andrew Vanderburg, Mercedes Lopez-Morales, Juan Perez-Mercader, Thomas R. Mattsson, Gongjie Li, Matthew Z. Heising, Aldo S. Bonomo, Mario Damasso, Travis A. Berger, Hao Cao, Amit Levi, and Robin D. Wordsworth. Growth model interpretation of planet size distribution. *Proceedings of the National Academy of Sciences*, 116 (20):9723–9728, April 2019. ISSN 1091-6490. doi:10.1073/pnas.1812905116. URL http://dx.doi.org/10.1073/pnas.1812905116.

Sebastian Zieba, Laura Kreidberg, Elsa Ducrot, Michaël Gillon, Caroline Morley, Laura Schaefer, Patrick Tamburo, Daniel D. B. Koll, Xintong Lyu, Lorena Acuña, Eric Agol, Aishwarya R. Iyer, Renyu Hu, Andrew P. Lincowski, Victoria S. Meadows, Franck Selsis, Emeline Bolmont, Avi M. Mandell, and Gabrielle Suissa. No thick carbon dioxide atmosphere on the rocky exoplanet trappist-1c. *Nature*, 620 (7975):746–749, June 2023. ISSN 1476-4687. doi:10.1038/s41586-023-06232-z. URL http://dx.doi.org/10.1038/s41586-023-06232-z.

A APPENDIX

This appendix provides a comparison between the results modeled with Zalmoxis (presented in Section 3.1) and those from Boujibar et al. [2020] and Wagner et al. [2012] for Earth-like exoplanets.

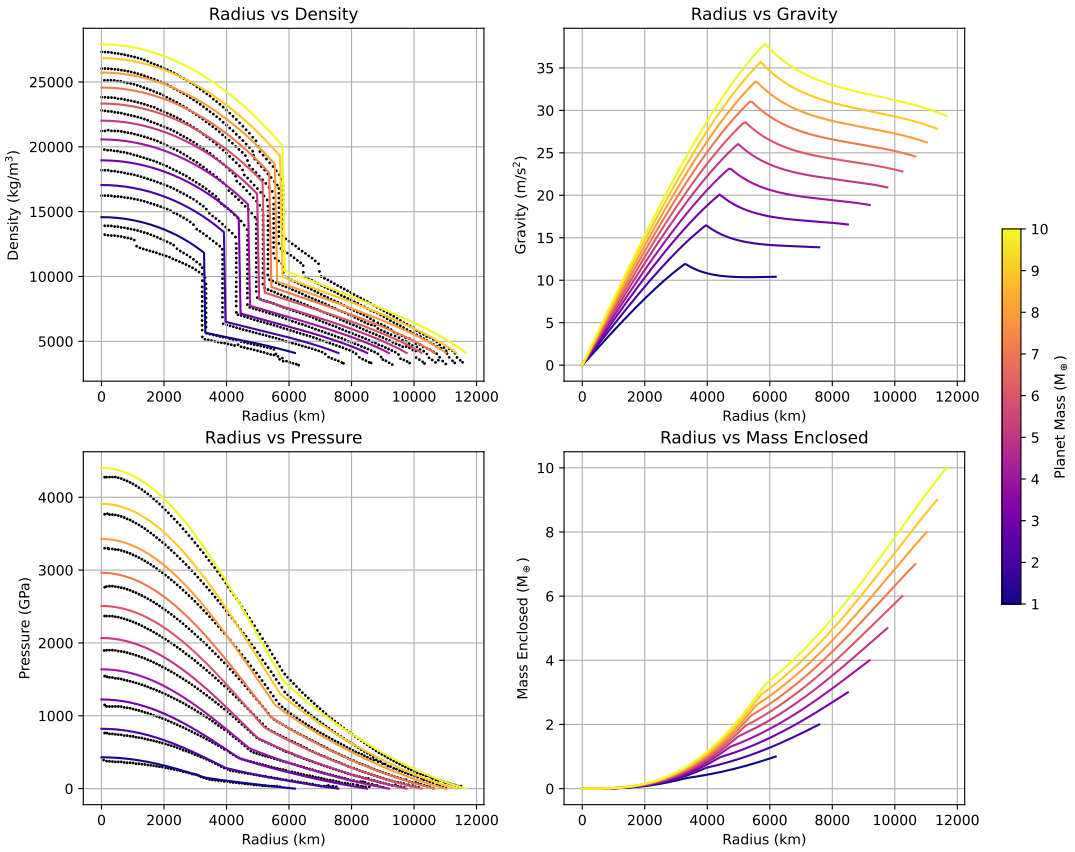

Figure A.1: Comparison of modeled density, gravity, pressure, and mass radial profiles (solid lines) with reference models (scattered points) from Boujibar et al. [2020] for Earth-like rocky exoplanets with 32.5% Fe core and 67.5% $MgSiO_3$ mantle by mass. For each panel, each profile corresponds, from bottom to top, to a planetary mass of 1 to 10 $M_\oplus$ in 1 $M_\oplus$ increments. Note that only density and pressure profiles were available in Boujibar et al. [2020]; the gravity and enclosed mass panels are shown here solely for completeness of the modeled output.

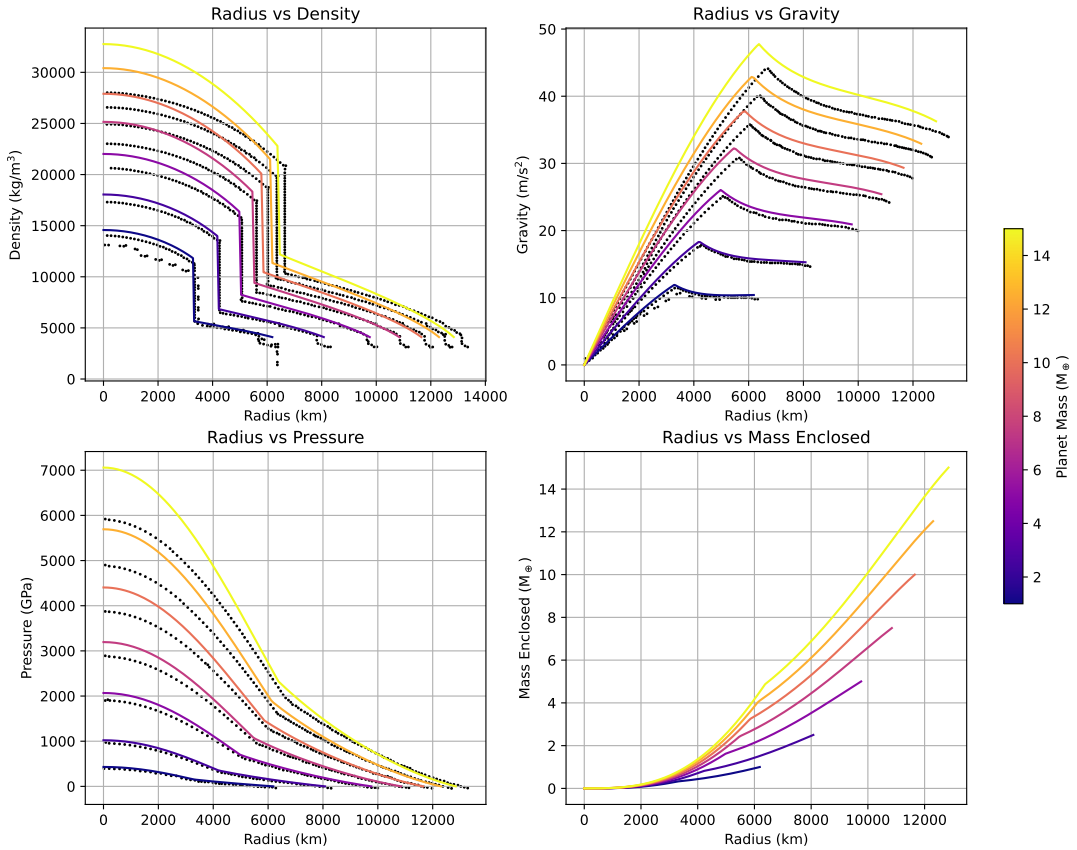

Figure A.2: Comparison of modeled density, gravity, pressure, and mass radial profiles (solid lines) with reference models (scattered points) from Wagner et al. [2012] for Earth-like rocky exoplanets with 32.5% Fe core and 67.5% $MgSiO_3$ mantle by mass. For each panel, each profile corresponds, from bottom to top, to a planetary mass of 1 to 15 $M_\oplus$ in 2.5 $M_\oplus$ increments. Note that only density, pressure, and gravity profiles were available in Wagner et al. [2012]; the enclosed mass panel is shown here solely for completeness of the modeled output.

B APPENDIX

This appendix contains plots from the simulations of the thermal and volatile evolution of Earth-like rocky exoplanets with masses ranging from 1 to 7 $M_\oplus$, as discussed in Section 3.4. The figures presented here correspond to and mirror Figures 3.6–3.8 shown for the fiducial case in Section 3.3.

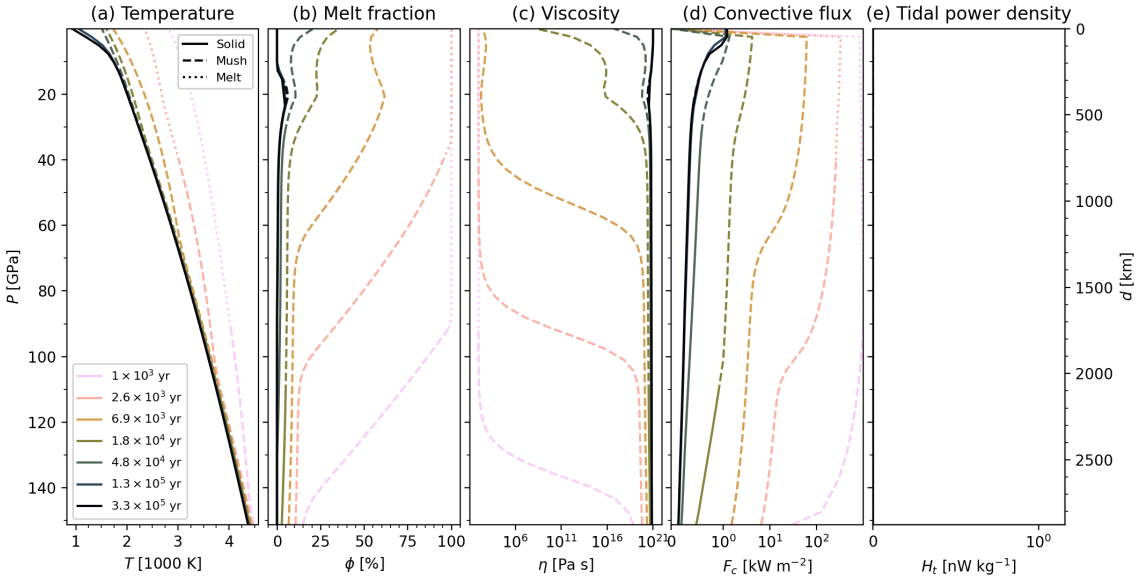

(a) 1 $M_\oplus$ planet

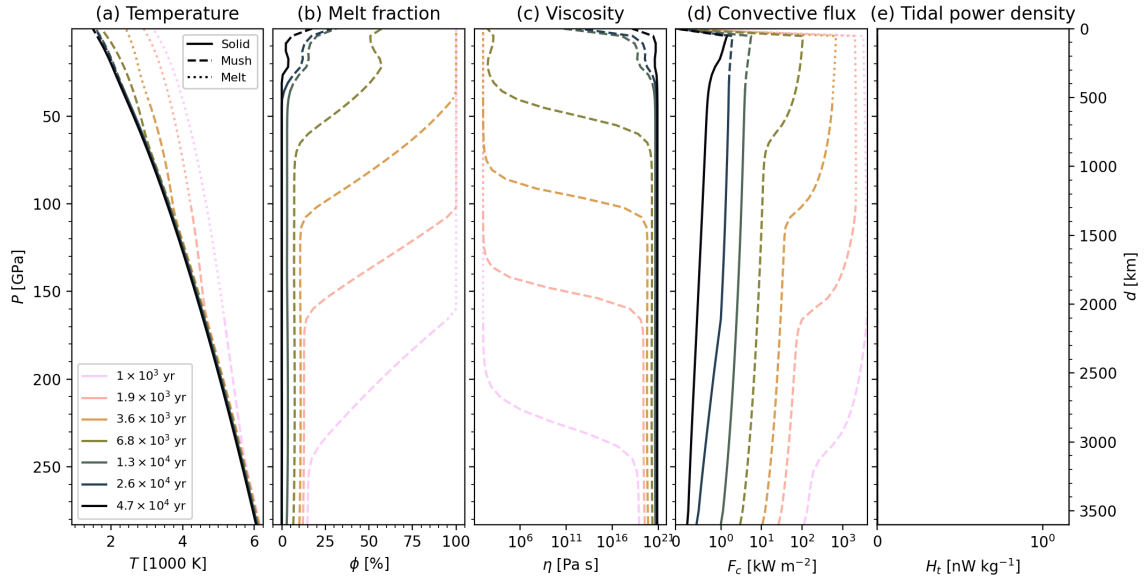

(b) 2 $M_\oplus$ planet

Figure B.1: Pressure-dependent profiles of interior mantle properties for 1 and 2 $M_\oplus$ planets. Panel descriptions follow those in Figure 3.6.

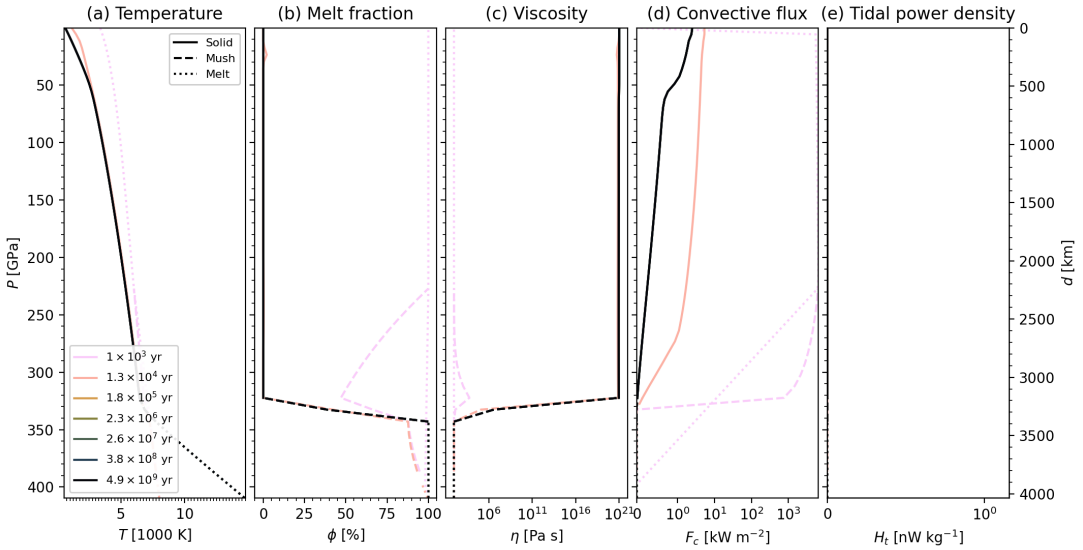

(a) 3 $M_\oplus$ planet

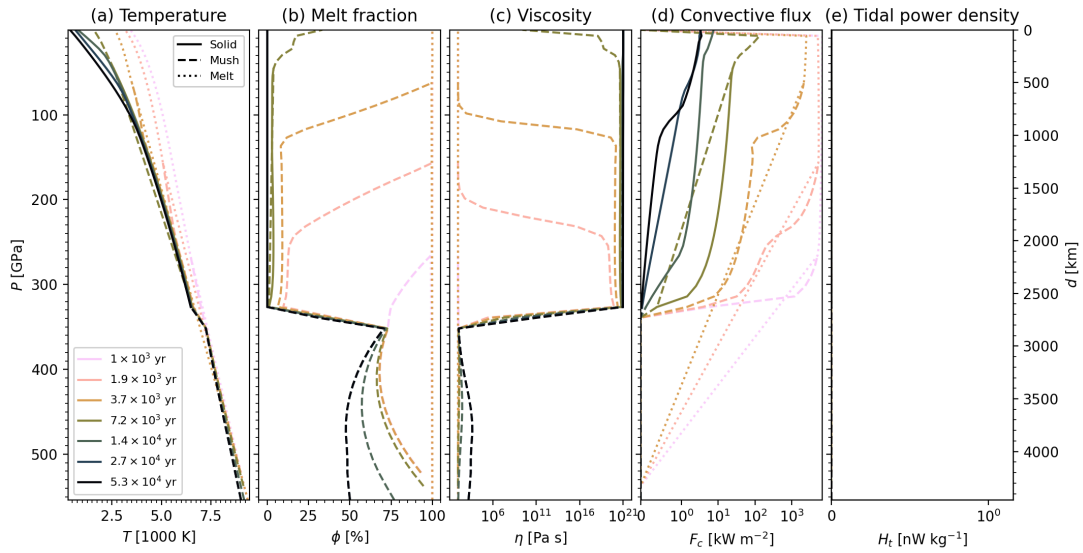

(b) 4 $M_\oplus$ planet

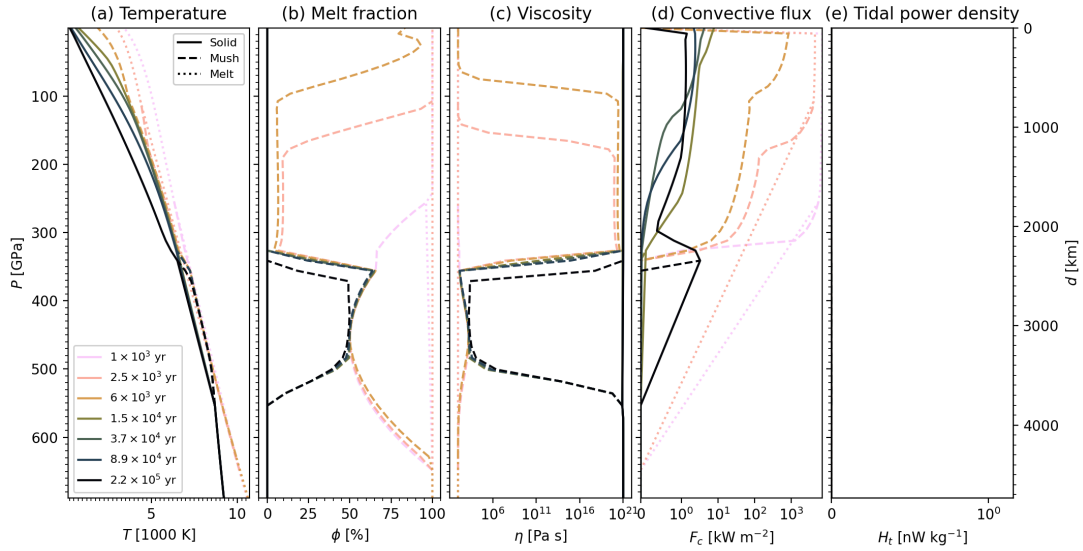

(c) 5 $M_\oplus$ planet

Figure B.2: Pressure-dependent profiles of interior mantle properties for 3, 4, and 5 $M_\oplus$ planets. Panel descriptions follow those in Figure 3.6.

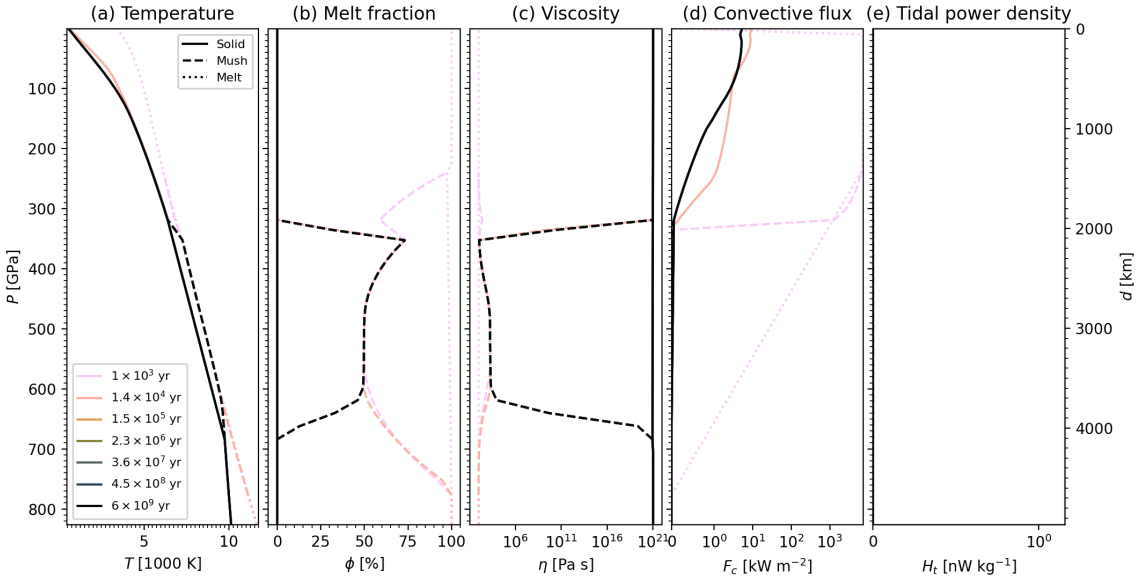

(a) 6 $M_\oplus$ planet

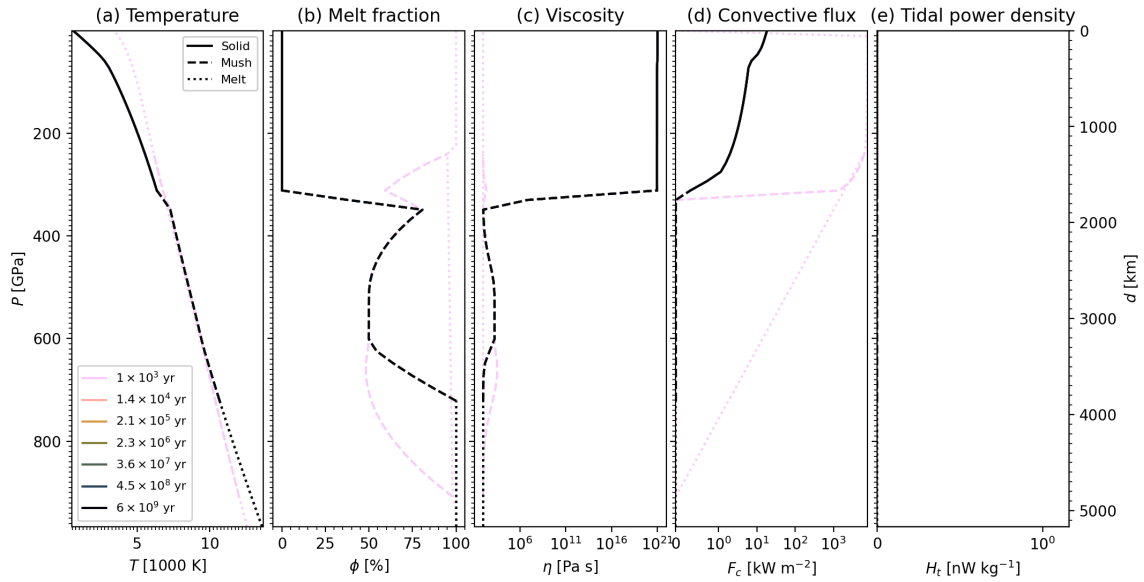

(b) 7 $M_\oplus$ planet

Figure B.3: Pressure-dependent profiles of interior mantle properties for 6 and 7 $M_\oplus$ planets. Panel descriptions follow those in Figure 3.6.

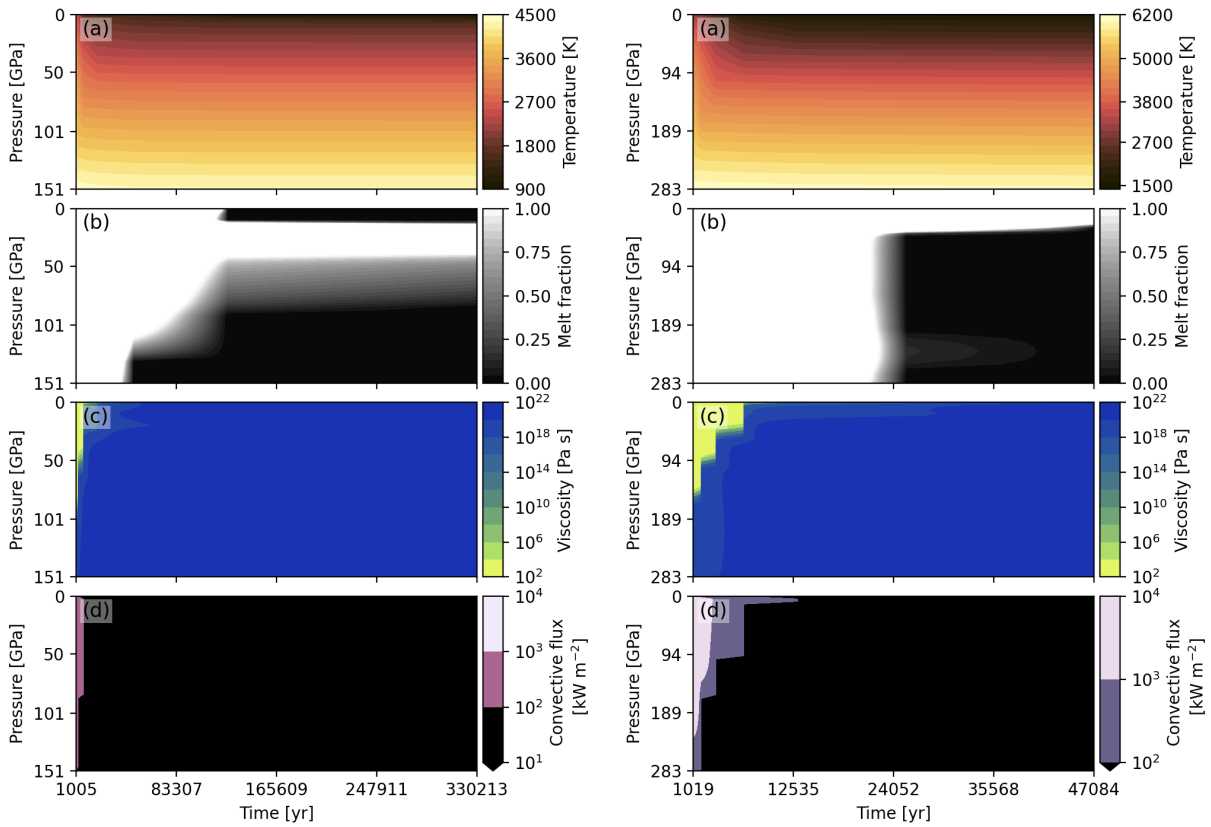

(a) 1 $M_\oplus$ planet **(b)** 2 $M_\oplus$ planet

Figure B.4: Time evolution of the interior structure in pressure space for 1 and 2 $M_\oplus$ planets. Panel descriptions follow those in Figure 3.7.

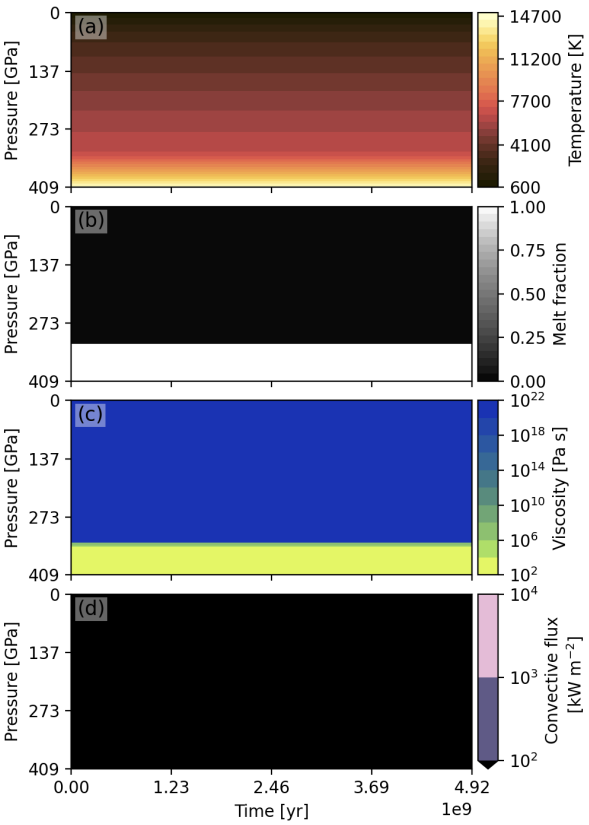

(a) 3 $M_\oplus$ planet

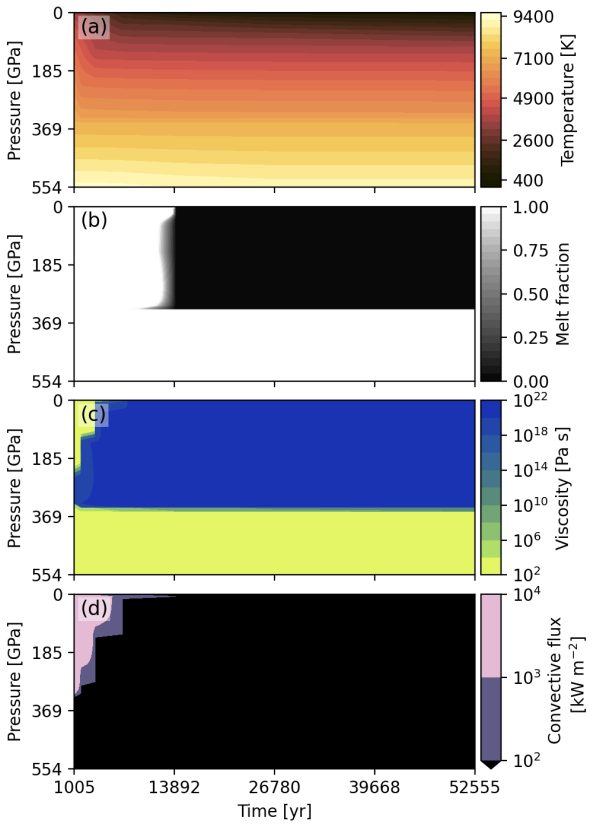

(b) 4 $M_\oplus$ planet

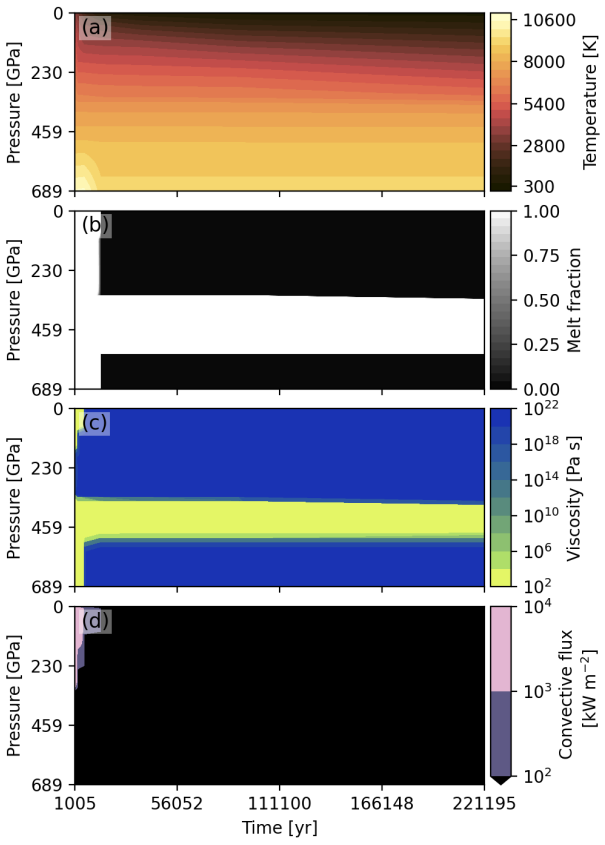

(c) 5 $M_\oplus$ planet

Figure B.5: Time evolution of the interior structure in pressure space for 3, 4, and 5 $M_\oplus$ planets. Panel descriptions follow those in Figure 3.7.

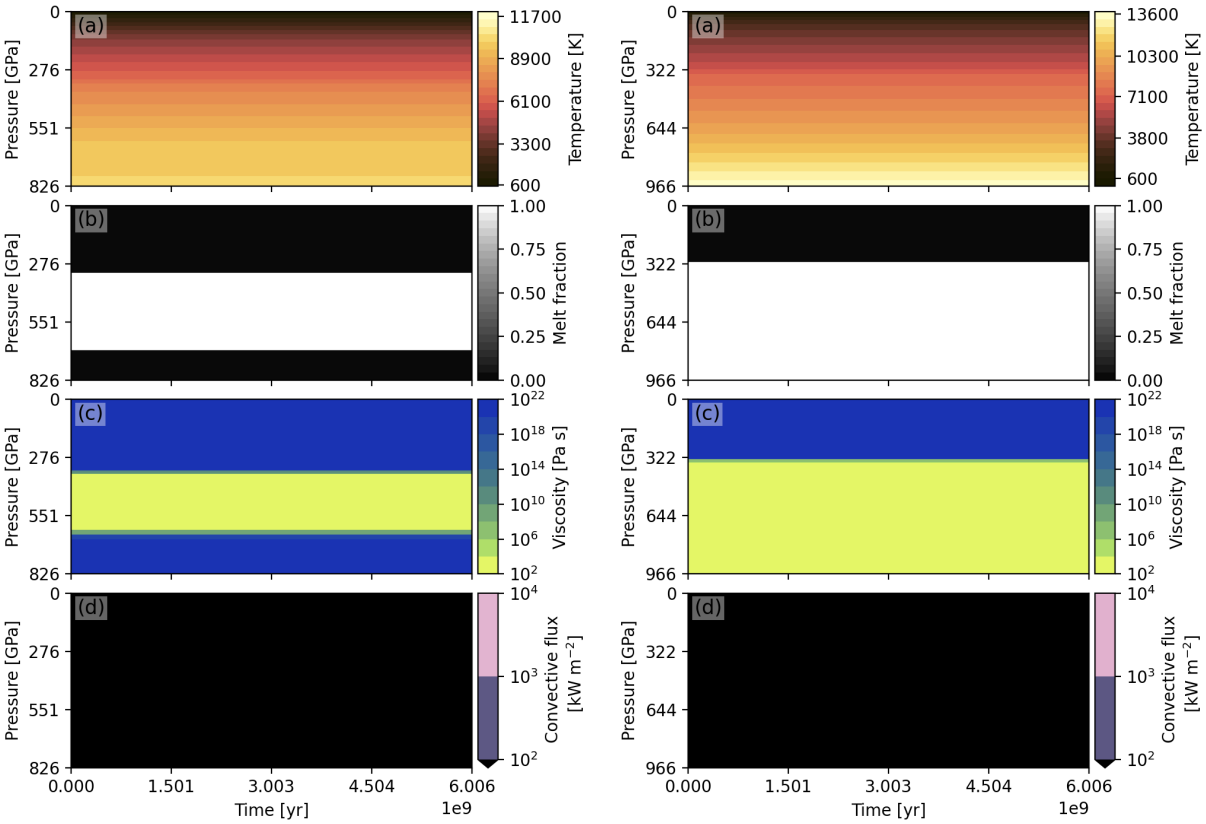

(a) 6 $M_\oplus$ planet

(b) 7 $M_\oplus$ planet

Figure B.6: Time evolution of the interior structure in pressure space for 6 and 7 $M_\oplus$ planets. Panel descriptions follow those in Figure 3.7.

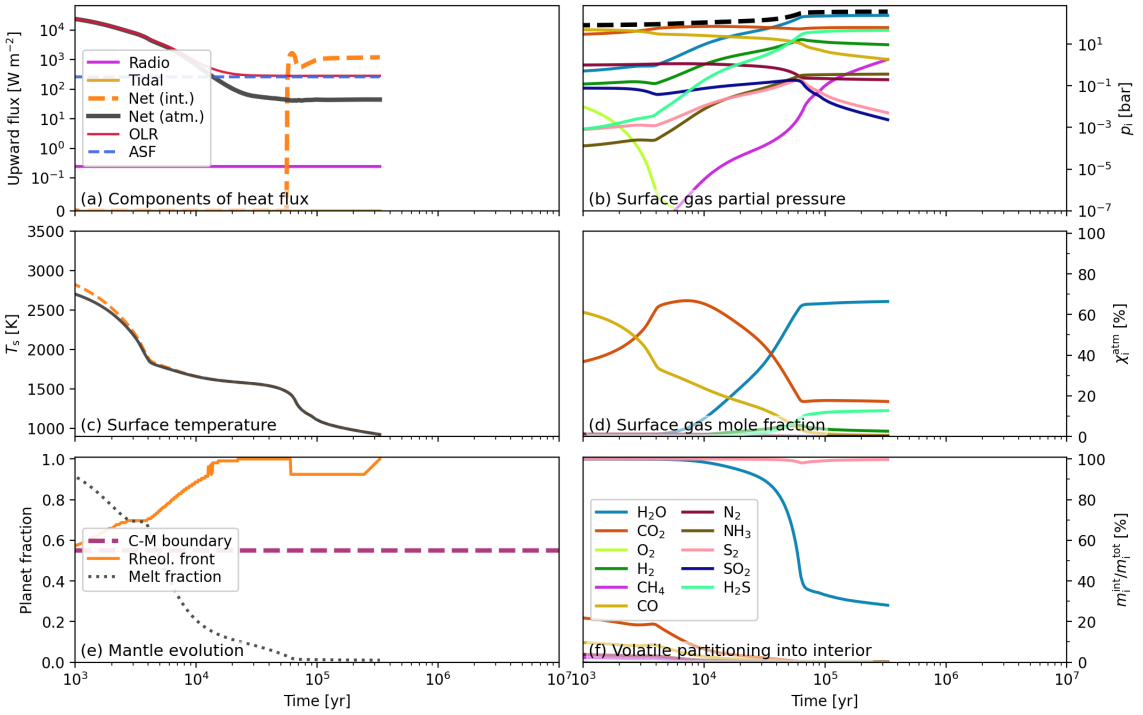

(a) 1 $M_\oplus$ planet

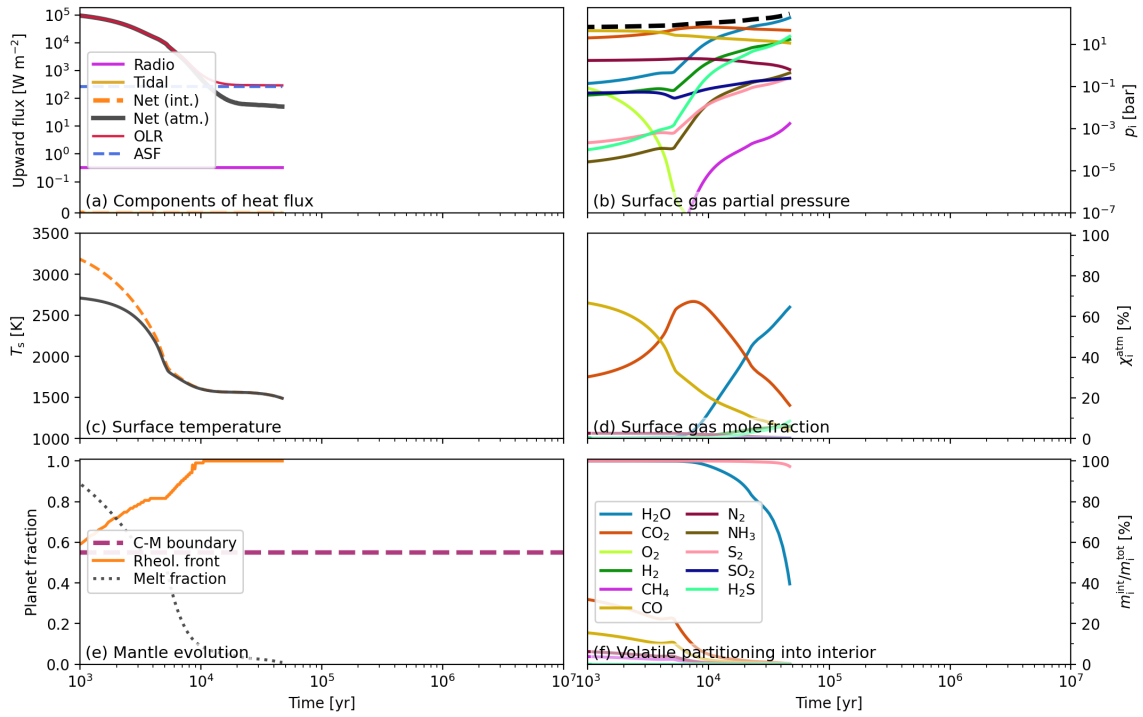

(b) 2 $M_\oplus$ planet

Figure B.7: Time evolution of the thermal and volatile state for 1 and 2 $M_\oplus$ planets, each starting with a linear initial temperature profile. Panel descriptions follow those in Figure 3.8.

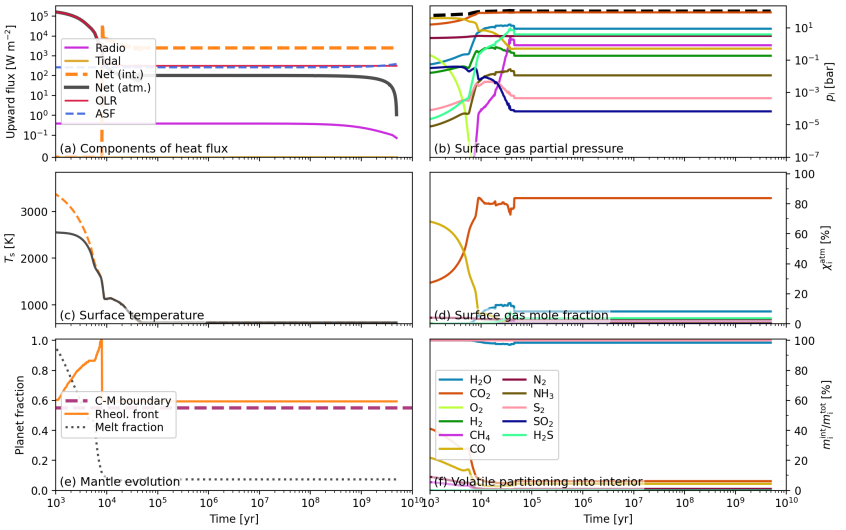

(a) 3 $M_\oplus$ planet

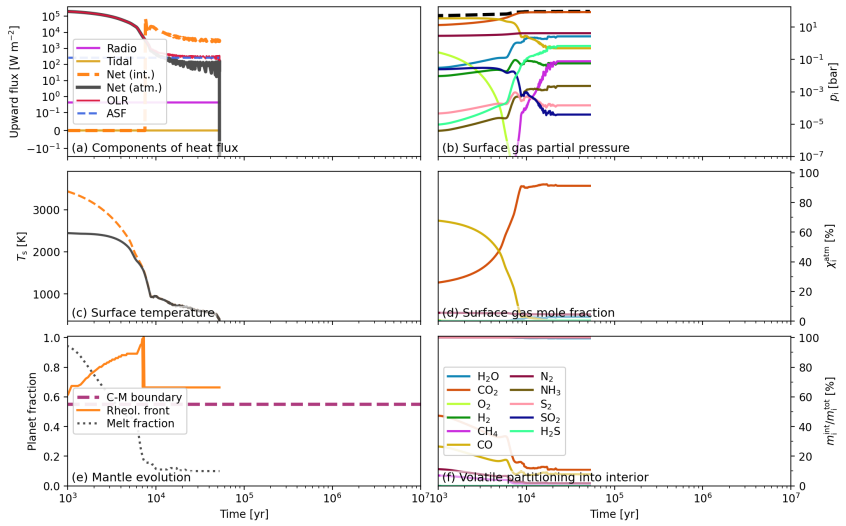

(b) 4 $M_\oplus$ planet

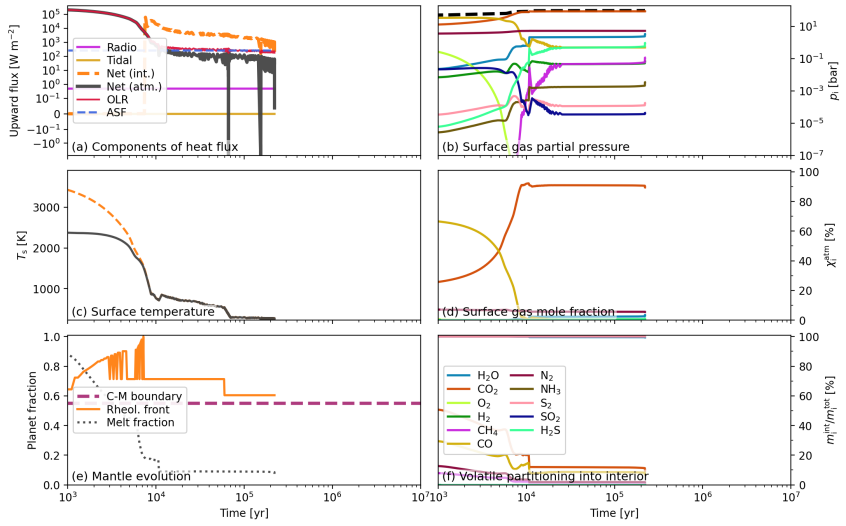

(c) 5 $M_\oplus$ planet

Figure B.8: Time evolution of the thermal and volatile state for 3, 4, and 5 $M_\oplus$ planets, each starting with a linear initial temperature profile. Panel descriptions follow those in Figure 3.8.

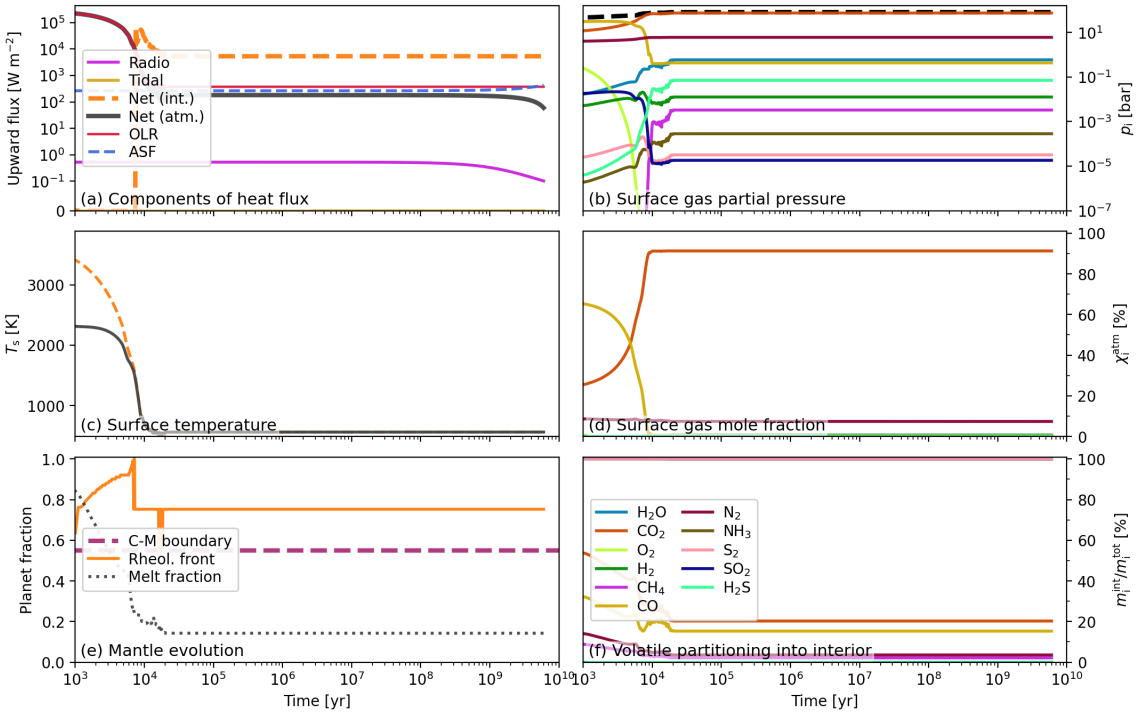

(a) 6 $M_\oplus$ planet

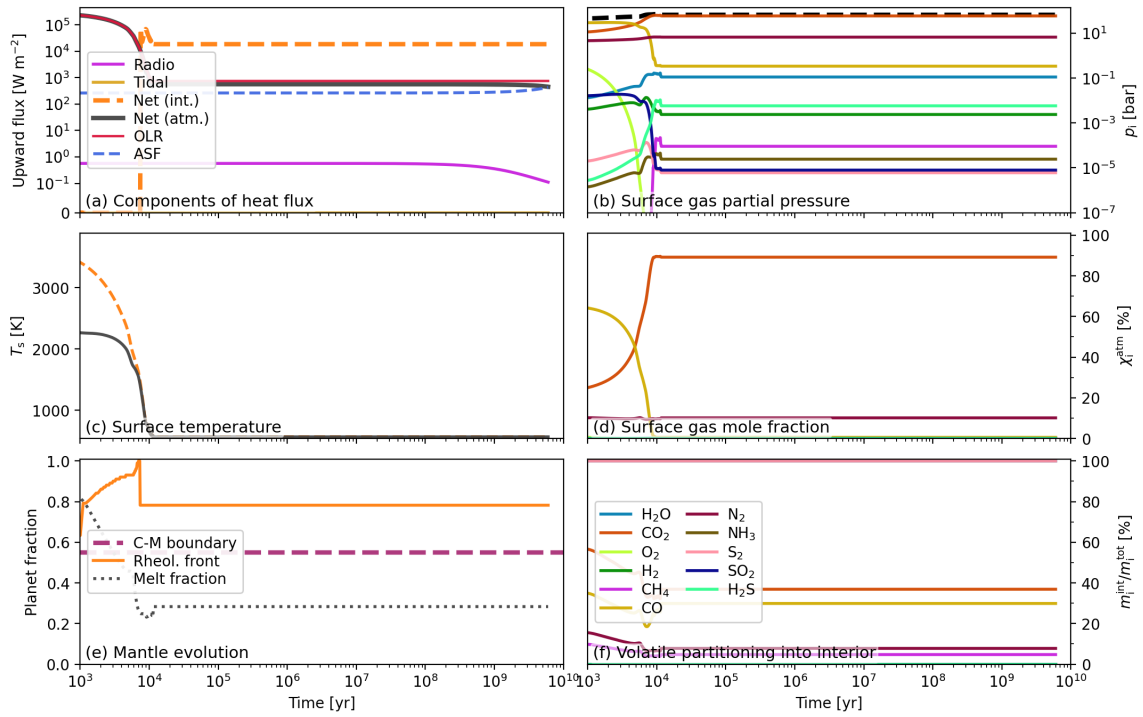

(b) 7 $M_\oplus$ planet

Figure B.9: Time evolution of the thermal and volatile state for 6 and 7 $M_\oplus$ planets, each starting with a linear initial temperature profile. Panel descriptions follow those in Figure 3.8.